2010

High Precision Atomic Mass Spectrometry with Applications to Neutrino Physics, Fundamental Cosntants and Physical Chemistry

Brianna Mount

THE FLORIDA STATE UNIVERSITY

COLLEGE OF ARTS AND SCIENCES

HIGH PRECISION ATOMIC MASS SPECTROMETRY WITH APPLICATIONS TO NEUTRINO PHYSICS, FUNDAMENTAL COSNTANTS AND PHYSICAL CHEMISTRY

By

BRIANNA MOUNT

A Dissertation submitted to the
Department of Physics
in partial fulfillment of the
requirements for the degree of
Doctor of Philosophy

Degree Awarded:
Fall Semester, 2010

The members of the committee approve the dissertation of Brianna Mount defended on October 29, 2010.

_____
Edmund Myers
Professor Directing Dissertation

_____
Nicholas Bonesteel
Professor Co-Directing Dissertation

_____
Alan Marshall
University Representative

_____
Laura Reina
Committee Member

_____
Ingo Wiedenhoever
Committee Member

Approved:

_____
Mark Riley, Chair, Department of Physics

_____
Joseph Travis, Dean, College of Arts and Sciences

The Graduate School has verified and approved the above-named committee members.

ACKNOWLEDGEMENTS

I feel very fortunate to have been a part of the history of the MIT/FSU Penning Trap. The many graduate students and post-docs throughout the twenty year history of the trap at MIT had truly made an amazing apparatus. The phrase is now becoming cliché, but my research was accomplished by "standing on the shoulders of giants."

I arrived on the scene in the spring of 2007, three years after Ed and Matt had moved the apparatus to Florida State University. By that time, the Penning Trap had been rebuilt amazingly quickly, and had already been used to measure several precise masses. This is in great part due to the abilities and diligence of Ed. I am very thankful to have had an advisor with such a seemingly encyclopedic knowledge of many branches of physics (and beyond), and a willingness to take time to share his expertise.

In addition to teaching me almost everything I know about experimental physics, Ed also gave me opportunities to be exposed to many different cultural experiences mainly through the various conferences that I attended. I would also like to thank Ed's wife, Lisa, for showing me that there is more to Tallahassee than the FSU-PPT lab. I will always remember our canoeing trip with wild manatees! Not to mention the fateful Finland trip and the reindeer sleigh ride! You both have had an amazing influence on my life.

I am very grateful to have had such a long overlap with Matt. He taught me the details of the day-to-day running of the trap and suffered with patience through my endless questions. I would also like to thank Andrew Zarella for helping greatly with the ever-present job of filling the cryogens. Raman Rana is the next graduate student to inherit the trap. I have enjoyed getting to know him this summer, and I know the trap is in good hands.

I would not be where I am without the guidance of my parents. Mom, you have made me the independent person I am today. Dad, you gave me my perseverance. Thank you both.

Most of all, I wish to thank my husband, Dan. I am so grateful you were willing to make enormous sacrifices in our first few married years. I can't wait to start a new chapter with you!

I would also like to acknowledge funding from the NSF and NIST.

TABLE OF CONTENTS

List of Tables vi
List of Figures x
Abstract xi

1. INTRODUCTION 1

1.1 History of Atomic Mass Measurements 1
1.2 Modern High Precision Penning Traps 3
1.3 Brief History of the MIT/FSU Trap 4
1.3.1 MIT Mass Table 5
1.3.2 2003-2007 FSU Mass Table 5
1.3.3 My Career at FSU 6
1.4 Structure of this Dissertation 7

2. EXPERIMENTAL APPARATUS AND TECHNIQUES 9

2.1 Penning Trap Introduction 9
2.2 Atomic Mass Measurement Process 11
2.2.1 Making Ions 13
2.2.2 Making *Two* Ions 14
2.2.3 Vapor Loader 15
2.2.4 Measuring the Cyclotron Frequency: Pi Pulses and PNPs 16
2.2.5 Swapping Ions 18
2.2.6 Ratio Measurement 20
2.2.7 Mass Difference and Resultant Mass 21
2.3 Systematic Effects 22
2.3.1 Trap Imperfection: Electrostatics 22
2.3.2 Trap Imperfection: Magnetic Field 23
2.3.3 Trap Imperfection: Equilibrium Position 23
2.3.4 Image Charge 24
2.3.5 Ion-Ion Interactions 24
2.3.6 F_z Shifts: Ion-Detector Interaction 25
2.3.7 F_z Shifts: Differential Voltage Drift 26
2.4 Trap Characterization 27
2.4.1 Magnetic Field "Event" of January 2009 and Characterization 27
2.4.2 Obtaining Cyclotron Radii 28
2.4.3 Measuring Amplitude Dependent Shifts: f_z vs. ρ_m and ρ_c 29

3. CYCLOTRON FREQUENCY MEASUREMENTS FOR NUCLEAR APPLICATIONS 31

3.1 *Q*-value Measurements for Neutrinoless Double Beta Decay and Double Electron Capture 31
3.1.1 Motivations 31
3.1.1.1 Neutrinoless Double Beta Decay 31
3.1.1.2 Neutrinoless Double Electron Capture 35
3.1.2 ^{130}Xe/^{130}Te Data and Analysis 36
3.1.3 ^{76}Ge/^{76}Se Data and Analysis 40

3.1.4 Discussion 45
3.2 "World's Smallest Beta Decay Q-value 46
3.2.1 Motivation 46
3.2.2 ^{115}In/^{115}Sn Data and Analysis 47
3.2.3 Discussion 49

4. CYCLOTRON FREQUENCY MEASUREMENTS FOR ATOMIC PHYSICS AND PHYSICAL CHEMISTRY 51
4.1 Stable Alkali Masses 51
4.1.1 Motivations 51
4.1.2 Experimental Details 54
4.1.3 Discussion 60
4.2 ^{18}O (and ^{19}F) Mass 62
4.2.1 Motivations 62
4.2.2 Experimental Details 63
4.2.3 Discussion 65
4.3 ^{17}O Mass 65
4.3.1 Motivations 65
4.3.2 Experimental Details 66
4.3.3 Discussion 67

5. MEASUREMENTS OF MOLECULAR ION ELECTRONIC DIPOLE MOMENTS BY MEASURING POLARIZABILITY SHIFTS TO THE CYCLOTRON FREQUENCY 68
5.1 Motivations for Electronic Dipole Measurements of Molecular Ions 68
5.2 Polarizability Shifts to the Cyclotron Frequency 69
5.3 Calculating Polarizability Due to Molecular Structure 69
5.3.1 HCO^+ Molecular Structure and Polarizability 70
5.3.2 NH^+ Molecular Structure and Polarizability 72
5.4 Polarizability "Jumps" 73
5.4.1 HCO^+ Jump Rate 74
5.4.2 NH^+ Jump Rate 75
5.5 HCO^+ Data Collection and Analysis 76
5.6 NH^+ Data Collection and Analysis 81
5.7 Conclusion and Summary of Dipole Moment Measurements 83

6. SUMMARY AND FUTURE WORK 85
6.1 Current FSU Table 85
6.2 Future Work with Current Detection Circuit 86
6.2.1 ^{174}Yb Mass Measurement for the Fine Structure Constant 86
6.2.2 NH^+ Molecular Spectroscopy 86
6.2.2 Direct Test of $E = mc^2$ with ^{35,36}Cl 86
6.2.2 Mass of ^{136}Ba for Neutrinoless Double Beta Decay 87
6.3 Future Work with New Higher Frequency Detection Circuit 87
6.3.1 The Mass of the ^{6,7}Li Monomers 87
6.3.2 ^{3}He/^{3}H Q-value for Neutrino Mass Measurements 87

6. LIST OF REFERENCES 89

LIST OF TABLES

1.1 Precision atomic masses measured at MIT (prior to 2002) 5

1.2 Precision atomic masses measured at FSU between 2003 and 2007 6

1.3 Chronological order of data taken during my time at FSU 7

3.1 Neutrinoless double beta decay candidates 34

3.2 Average cyclotron frequency (*i.e.* inverse mass) ratios and systematic corrections for the ^{130}Xe/^{130}Te data 38

3.3 Mass difference equations corresponding to the ratios given in Table 3.2 39

3.4 Atomic masses of ^{130}Xe and ^{130}Te obtained from the different ratios, and their weighted averages, compared with previous values 39

3.5 ρ_c^{cal} values associated with each m/q 42

3.6 Average cyclotron frequency (*i.e.* inverse mass) ratios and systematic shifts for the ^{74,76}Ge/^{74,76}Se data 43

3.7 Mass difference equations corresponding to the ratios given in Table 3.6 44

3.8 Atomic masses (in u) of ^{74,76}Ge and ^{74,76}Se 45

3.9 The three $Q_{\beta\beta}$ decay values measured by the FSU-PPT compared to other recent mass spectrometer measurements 45

3.10 Average cyclotron frequency (*i.e.* inverse mass) ratios and systematic corrections for the ^{115}In/^{115}Sn data 48

3.11 Mass difference equations corresponding to the ratios given in Table 3.10 48

3.12 Atomic masses (in u) of ^{115}In and ^{115}Sn compared with values in the AME 2003 49

3.13 Comparison of the determinations of the ^{115}In($9/2^+$)→^{115}Sn($3/2^+$) β-decay Q-value 49

4.1 Determinations of the fine structure constant 52

4.2 Comparison of FSU and MIT reference ions 55

4.3 Average cyclotron frequency (*i.e.* inverse mass) ratios and systematic corrections for the alkali data 58

4.4 Mass differences and derived atomic mass of the relevant alkali, corresponding to the ratios given in Table 4.3 59

4.5 Final atomic masses of ^{6}Li, ^{23}Na, ^{39,41}K, ^{85,87}Rb and ^{133}Cs obtained from the different ratios and their weighted averages, compared with previous values 60

4.6 Error budgets for mass ratios obtained during the ^{18}O and ^{19}F experiments....64

4.7 Mass difference equations corresponding to the ratios given in Table 4.6 64

4.8 Masses for ^{18}O and ^{19}F from various sources....65

4.9 Average cyclotron frequency ratios (*i.e.* inverse mass) and systematic corrections for ^{17}O data 66

4.10 Mass difference equations corresponding to the ratios given in Table 4.9 67

4.11 Atomic masses for ^{17}O obtained from the different ratios, and their weighted average, compared with the result of the AME 2003 and the Cologne group's molecular spectroscopy result 67

5.1 Polarizabilities, α, and resultant cyclotron frequency shifts, $\Delta\omega_c/\omega_c$ for the lowest rotational levels of HCO^+ assuming μ = 3.888(4)D and B_0 = 44594.42873(28) MHz 71

5.2 Polarizabilities from the theoretical calculation of Reference [135] and resultant cyclotron frequency shifts for NH^+ 73

5.3 Quantities needed in the calculation of the lifetime against absorption of the ground state of HCO^+, assuming T = 4.2K, μ = 3.888(4)D and B_0 = 44594.42873(28)MHz and standard CODATA values for the other constants....74

5.4 Expressions for the amplitudes of the peaks in the histogram of the ratio of the cyclotron frequencies of HCO^+ vs. $^{28}SiH^+$ assuming a Boltzmann distribution at temperature T.....80

5.5 Results from fitting the histograms of the ratio of the cyclotron frequencies of HCO^+ versus $^{28}SiH^+$....80

5.6 Population of all states J≥1 relative to J=0....81

5.7 The FSU HCO^+ dipole measurement compared to calculated dipole moments....83

5.8 The FSU NH^+ dipole measurement compared to calculated dipole moment.....83

6.1 Summary of Mass Measurements in this Dissertation 85

LIST OF FIGURES

1.1 Timeline of the fractional uncertainty in the mass of fluorine 3

2.1 Cross-section of the FSU-PPT electrodes 10

2.2 The three harmonic modes in a Penning trap 11

2.3 Penning trap apparatus 12

2.4 Rough schematic of the vapor loader 15

2.5 Sketch of a homemade element 16

2.6 Fast Fourier Transform (FFT) of an ion's axial ring-down signal as it appears on the screen of ICR-Master (a Lab-View program developed specifically for this Penning trap at MIT) 17

2.7 Swapping Procedure 19

2.8 Typical cyclotron frequency ratio data 21

2.9 Magnetic field variation since the start of measurements at FSU 28

3.1 Possible neutrino mass hierarchies 32

3.2 Double beta decay total electron energy spectrum 33

3.3 Level scheme for the double-electron capture of ^{74}Se to the second (2^+) excited state of ^{74}Ge 36

3.4 Cyclotron frequency ratios relative to $^{84}Kr^{2+}$, uncorrected for systematic errors, obtained from each run 40

3.5 Measured ρ_c^{cal} values for m/q=37,38,42 41

3.6 Values of $V_{gr}{}^0$ from f_z vs ρ_m vs V_{gr} measurements versus m/q 42

3.7 $^{84}Kr^{2+}/^{84}Kr^{3+}$ ratio measurements corrected for systematic effects 44

3.8 Level scheme for the beta decay of the ground state of ^{115}In showing relevant half-lives and branching ratios 46

3.9 Cyclotron frequency ratios, uncorrected for systematic effects, obtained for each run 47

3.10 The three most precise β-decay Q-values of $^{115}In(9/2^+)\rightarrow{}^{115}Sn(3/2^+)$ from two Penning trap measurements (JYFLTRAP and FSU-PPT) and a measurement of the half-life combined with nuclear matrix elements (NMEs) 50

4.1 Determinations of the fine structure constant....52

4.2 Comparison of masses from MIT, AME 2003 and FSU....61

4.3 Comparison of potassium masses....61

4.4 Comparison of Penning Trap mass measurements of ^6Li 62

5.1 Energy level diagram of HCO^+ for rotational levels $J=0,1,2$, in its electronic and vibrational ground state 71

5.2 Zeeman energies of NH^+, $X^2\Pi_{1/2}$ (υ=0), B = 0-10 T 72

5.3 All cyclotron data for HCO^+, showing polarizability jumps....75

5.4 The only set of NH^+ vs $^{15}N^+$ data showing a jump in the polarizability of NH^+ 76

5.5 Chemical structure of Delrin, or poloxymethylene 76

5.6 Sample HCO^+ run....77

5.7 Piece-wise versus Polynomial interpolation....78

5.8 All cyclotron frequency measurement shifts, indicating the states of the HCO^+ ion....78

5.9 All ratio measurements for $NH^+/^{15}N^+$ with an enlargement showing the two opposite parity states 82

ABSTRACT

The Florida State University single-ion cryogenic Penning trap mass spectrometer has been used to precisely measure the masses of the doublets ^{76}Ge/^{76}Se and ^{74}Ge/^{74}Se to provide precision *Q*-values to aid in searches for neutrinoless double beta decay as well as neutrinoless double electron capture. The observation of these processes would provide evidence for the Majorana nature of the electron neutrino and information on neutrino mass. The smallest known β-decay *Q*-value has also been determined by the measurement of the masses of ^{115}In and ^{115}Sn. The masses of stable alkali isotopes for application as precision mass references as well as for the photon-recoil method of determining the fine structure constant have also been measured. For physical chemistry, the masses of the oxygen isotopes, ^{17}O and ^{18}O have been measured to test the Dunham-Watson formalism for the ro-vibrational energy levels of isotopic variants of a diatomic molecule. By measuring the small shifts in cyclotron frequency due to polarizability, the dipole moments of NH^+ and the astrophysically important molecule HCO^+ have been measured for the first time. The mass of ^{19}F has also been measured for use as a mass standard.

Several improvements and developments to the FSU Precision Penning Trap (FSU-PPT) have enabled these measurements. A vapor loader now allows vapors to be introduced into the trap, greatly increasing the range of species that can be measured. The previously developed technique for measuring a cyclotron frequency ratio, in which two ions are simultaneously trapped, but swapped between large and small cyclotron orbits has been further developed to allow the ion in the large cyclotron orbit to be constantly monitored and therefore recentered more efficiently. This technique has also been extended to enable two-ion cyclotron frequency ratio measurements of non-mass doublets, as well as of multiply charged ions.

1. INTRODUCTION

1.1 History of Atomic Mass Measurements

In the early 19th century, John Dalton conveyed the first clear ideas of atomic theory and measured the first atomic weights [1,2]. These first atomic mass measurements used the mass of hydrogen as the standard, m(H) = 1, since it was the smallest known element [3]. Throughout the following decades, researchers built upon and improved Dalton's atomic mass table [2,4,5]. The precision of these early mass measurements was sufficient to aid in the development of modern chemistry: in particular, they provided a piece of the puzzle which led to Mendeleev's 1869 discovery of the periodic table of elements [6].

By the turn of the century, almost 80 atomic weights had been measured [5]. Since oxygen combined readily with more compounds than hydrogen (in fact, almost all masses then measured were relative to the mass of oxygen), the more convenient definition of m(O) = 16 was gradually agreed upon [2,3]. During this time period, the quantities measured by experimentalists were actually atomic *weights*[1], which contain the mass of the different isotopes combined proportionally with their isotopic abundances. Chemically, isotopes of an element are the same, hence indistinguishable to early researches. In the words of Frederick Soddy, winner of the 1921 Nobel Prize in Chemistry for his work on isotopes, "their atoms have identical outsides but different insides [7]."

Over one hundred years passed between Dalton's first mass table and the next major breakthrough in atomic mass measurement in the early 20th century. J.J. Thomson, aided by F.W. Aston, found that if he passed ionized neon through electric and magnetic fields and detected the neon beam at the end of its path with a photographic plate, that two parabolic curves were detected. He had discovered the two isotopes of neon. Since each isotope had a different mass, they were deflected differently through the fields [8]. After World War I, Aston continued his work and built his first mass spectrograph in 1918 [9]. Adding to Thomson's work, this spectrograph used a focusing technique to improve resolution. Two more iterations of his mass spectrograph refined its resolution even further, eventually leading to his measurement of 212 isotopes and the 1922 Nobel Prize [10,11].

In the early 1930's, a paper in a German electrical engineering journal describing the concept for a linear accelerator inspired Ernest Lawrence to create a device which used the

[1] This terminology is used for historical reasons and is admittedly confusing.

circular motion of charged particles about a magnetic field, combined with an oscillating electric field to accelerate ions (we now call this a cyclotron) [12,13]. The principle of cyclotron motion and in particular, the inverse dependence of the frequency on the mass, led to the development of ion cyclotron resonance (ICR) mass spectrometry in the early 1950's [14].

Building on all previous work, the next revolution in precision atomic mass measurements came with the development of the Penning trap by Hans Dehmelt in the 1960's and the isolation of a single electron in 1973 [15,16]. This trap consists of a magnetic field used to confine ions radially, and a quadropole electric field to confine the ions axially (see Chapter 2). These experiments at the University of Washington spawned many Penning trap groups worldwide (see next section). The most precise mass measurement to date is the mass of ^{16}O with a precision of 11 ppt [17].

While the rest of this dissertation will concentrate on the relatively small field of high precision atomic mass measurements, it should be noted that mass spectroscopy for chemical analysis has become an enormously powerful technique and has developed and branched into many areas of the sciences over the past century, and is a much larger field. Mass spectrometers have become common-place in laboratories for chemical analysis. Very good techniques (such as FT-ICR [18,19,20]) have been developed for chemical analysis of complex samples, able to measure 50,000 peaks in a single spectrum [21].

Figure 1.1 is a timeline of the fractional uncertainty of fluorine[2]. Fluorine was chosen since it is mononuclidic and therefore its atomic weight is its atomic mass[3] and because it has been measured with the Florida State University Precision Penning Trap (FSU-PPT).

[2] The masses in Figure 1.1 have been corrected for the differences over time in the definition of the atomic mass unit. With the determination of oxygen's isotopes in 1929 [22], physicists chose the definition m(^{16}O)=16, while chemists chose to remain using the mass of naturally occurring oxygen m(O) = 16. This disagreement continued until 1961, at which time it was agreed that the mass standard should be m(^{12}C) = 12 u [2,3]. This standard is still used today.

[3] Before the mass spectrometer, the quantities measured were atomic weights.

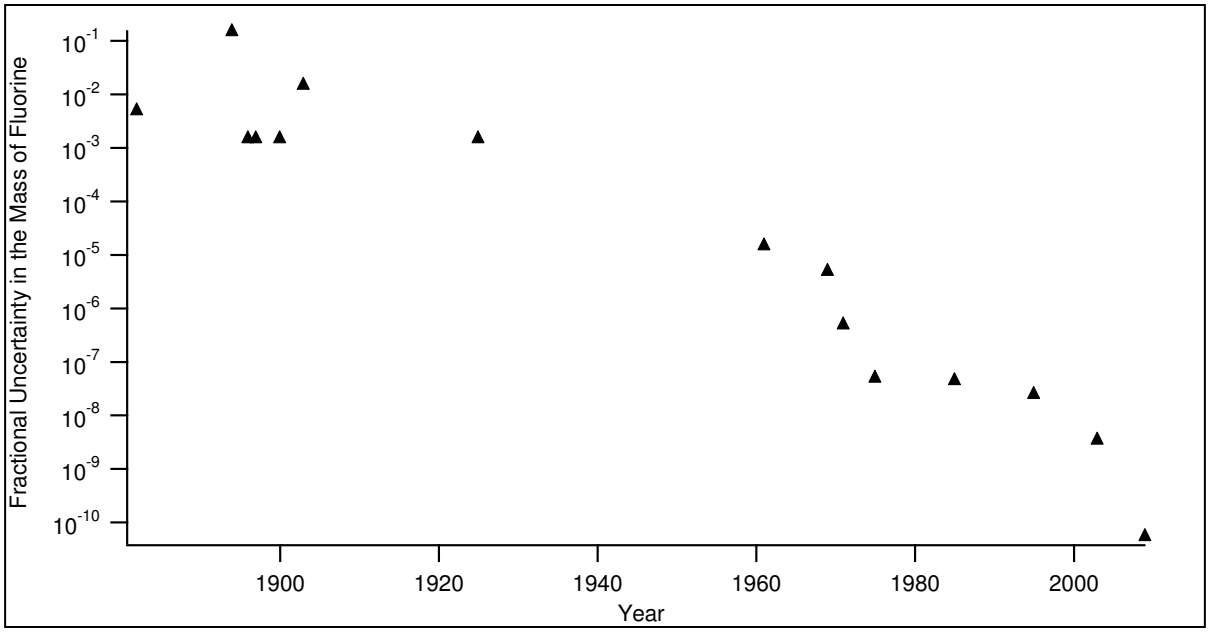

Figure 1.1 Timeline of the fractional uncertainty in the mass of fluorine [4,23].

1.2 Modern High Precision Penning Traps

It is possible to divide most modern high precision Penning traps into two classes determined by the techniques used to detect the ions [24-26]. The first class of experiments is non-destructive, relying on image currents to detect the ions. The most accurate work has been done with this category of traps. In addition to the MIT/FSU trap whose achievements will be discussed in Section 1.3, this category of traps includes work done at the University of Washington, Harvard and Mainz.

In pioneering work at the University of Washington, Hans Dehmelt and his associates measured the free electron g-factor in 1987 [27]. More precise measurements, with careful control of the quantized cyclotron motion, have recently been accomplished in 2008 by the Harvard group [28]. These measurements are important for the determination of the fine structure constant and to test QED (see Section 4.1). These two groups also each have the most stringent tests of CPT invariance, with lepton and baryon systems, respectively. The University of Washington compared the electron and positron magnetic moments [27] and the Harvard group compared the antiproton and proton mass-to-charge ratios [29]. At the University of Mainz, measurements of the g-factor of electrons bound in hydrogen-like ions have been

measured [30]. These can be used to determine the atomic mass of the electron and can also be used to test QED calculations.

The development of the modern Penning trap with image current detection for precision atomic mass measurements with "heavy" ions was first undertaken by Van Dyck at the University of Washington, leading to the most precise atomic mass to date [17], but also by David Pritchard and his associates at the Massachusetts Institute of Technology (MIT) [31-39]. It is this last system that is now housed at FSU and will be described in detail later in this dissertation. Recently, the University of Washington traps have been moved to the University of Heidelberg, under the direction of Klaus Blaum, where various high precision atomic mass and g-factor measurement experiments are under way.

The second class of precision Penning traps are those that use the time-of-flight detection technique. They generally approximate the free space cyclotron frequency through the measurement of just one frequency, which is the sum of the magnetron and trap-modified cyclotron frequencies of the ion in the trap (see Section 2.1). Excitation of the cyclotron motion by an rf drive at this frequency is detected using a destructive method, which expels ions from the Penning trap, and measures how fast they reach a detector. Faster ions correspond to a resonance with the drive frequency. This method is generally less precise than the method described in this dissertation, but is able to measure short-lived species[4]. Many of these types of Penning traps exist in nuclear physics laboratories.[5] Notable Penning trap mass spectrometers using time-of-flight detection (with recent publications referenced) include ISOLTRAP [41-43], JYFLTRAP [44-46], TITAN [47-50], SMILETRAP [51-53], LEBIT [54-56], CPT [57], and SHIPTRAP [58,59].

1.3 Brief History of the MIT/FSU Penning Trap

The Penning trap mass spectrometer now housed in the basement of the Collins Research Laboratory at Florida State University (FSU) was developed and operated at MIT from 1984 to 2003, producing the majority of the world's most precise mass measurements up to that time. This system was moved to its current location in the spring of 2003. This chapter serves as a

[4] The shortest-lived isotope ever measured in a Penning trap was ^{11}Li, with a half-life of 8.8 ms [40].
[5] For a review of time-of-flight spectrometers and their applications, see [24-26].

brief summary of the past mass measurements, along with my contribution to the world of precise measurements.

1.3.1 MIT Mass Table

The eighteen year history of the trap at MIT was filled with many developments in precision measurements, leading to the first sub-ppb mass measurements [31-39] and the first sub-10 ppt measurements of mass ratios [60]. Notable Penning trap advances at MIT included a phase-coherent method of determining the cyclotron frequency by mapping the phase of the cyclotron motion onto the axial motion (see Section 2.2.2) [61,62], a simultaneous two-ion ratio measurement technique [60], and the first detection of shifts to an ion's cyclotron frequency in a Penning trap due to electric polarizability (see Section 4.2) [63].

Table 1.1 Precision atomic masses measured at MIT (prior to 2002) [64,65].

	MIT Measurements	
Atom	**Mass (u)**	**σ_m/m (ppb)**
^{1}H	1.007 825 031 6(5)	0.50
^{2}H	2.014 101 777 9(5)	0.25
^{13}C	13.003 354 838 1(10)	0.08
^{14}N	14.003 074 004 0(12)	0.09
^{15}N	15.000 108 897 7(11)	0.07
^{16}O	15.994 914 615 5(21)	0.13
^{20}Ne	19.992 440 175 4(23)	0.12
^{23}Na	22.989 769 280 7(28)	0.12
^{28}Si	27.976 926 532 4(20)	0.07
^{40}Ar	39.962 383 122 0(33)	0.08
^{85}Rb	84.911 789 732(14)	0.16
^{87}Rb	86.909 180 520(15)	0.17
^{133}Cs	132.905 451 931(27)	0.20

1.3.2 2003-2007 FSU Mass Table

In the summer of 2003, the MIT Penning trap was relocated to Tallahassee by Edmund Myers and Matthew Redshaw. After rebuilding the apparatus, over the next four years the FSU group measured several atomic masses, along with the dipole moment of PH^+ [66].

Table 1.2 Precision atomic masses measured at FSU between 2003 and 2007 [67-70].

FSU Measurements 2003-2007		
Atom	**Mass (u)**	**σ_m/m (ppb)**
^{28}Si	27.976 926 535 0(6)	0.02
^{31}P	30.973 761 998 9(9)	0.03
^{32}S	31.972 071 173 5(16)	0.05
^{84}Kr	83.911 497 731(8)	0.10
^{86}Kr	85.910 610 628(8)	0.09
^{129}Xe	128.904 780 859(11)	0.09
^{132}Xe	131.904 155 086(10)	0.08
^{136}Xe	135.907 214 484(11)	0.08

1.3.3 My Career at FSU

I began working in the FSU Precision Penning Trap (FSU-PPT) lab in the spring of 2007, approximately four years after it had been moved. Matt was finishing up the second set of ^{84,86}Kr and ^{129,132}Xe mass measurements (see Table 1.2), and I "got my feet wet" during these measurements, learning how to make and manipulate ions and how to take and analyze data. The krypton and xenon measurements were the last to use the single ion make-kill-remake technique. All the following measurements from the FSU-PPT involve the two-ion swapping technique (see Section 2.2.3).

After Matt graduated, he decided to stay on as a post-doc. Therefore, for most of my time at FSU, Matt was involved in the measurements to varying degrees. The considerable quantity of measurements accomplished in 2008 and 2009 was due in large part to Matt's decision to stay at FSU, and the teamwork that followed.

There are two phases of the measurement: data taking and analysis. The "data taking" involves learning how to make new ions (Section 2.2.1), setting up the code to interchange the ions (aka "swapping scripts") (Section 2.2.3), then setting up and executing runs (Section 2.2.4), as well as making any auxiliary measurements necessary to determine systematic effects (Section 2.3.3). Because one is always working with signals that are close to the noise level, measurements with single ions are highly non-trivial, and considerable skill and ingenuity, as well as large amounts of patience and perseverance are necessary to obtain useful data. The analysis involves sifting through all the acquired data and deciding what parameters to use to apply systematic shifts, and in fact is far less demanding.

Although I was involved a little with the ^{18}O and ^{19}F data, the measurements were mostly done by Matt. Following this data set, I would generally take most of the data, and Matt would do the analysis, parts of which I would check. However, at the end of October 2008, I graduated to being responsible for the HCO^+ and $^{74,76}Se/Ge$ data and analysis. Since the $^{115}In/Sn$ measurement was considered time-sensitive, data was taken by me and the analysis was mostly done by Matt (and again partly checked by me) in an effort to publish expediently. The last set of data Matt was involved in before he left was the ^{23}Na data. It was taken and analyzed completely by Matt. The ^{6}Li and NH^+ data were taken after Matt had left for Michigan State and were analyzed solely by me.

1.4 Structure of this Dissertation

The motivations of the high precision atomic mass measurements discussed in this dissertation are diverse and include measurements for atomic and nuclear physics, as well as physical chemistry. I have decided to organize the measurements described in this thesis by their applications and not in chronological order.

Table 1.3 Chronological order of data taken during my time at FSU.

Approximate Date	Measurement
March 2008	^{19}F, ^{18}O
May 2008	$^{85,87}Rb$
June 2008	^{39}K
July 2008	^{41}K
August 2008	^{133}Cs
September 2008	$^{130}Xe/Te$
October 2008	^{17}O (dimer) HCO^+
November 2008 through February 2009	$^{74,76}Se/Ge$
March 2009	^{17}O (monomer)
April 2009	$^{115}In/Sn$
May 2009	^{23}Na
June 2009	^{6}Li
September 2009	NH^+

Chapter 2 is an introduction to Penning trap physics and describes several improvements to the FSU-PPT since Matt's dissertation. Chapter 3 describes the mass measurements conducted for nuclear physics applications, such as neutrinoless double beta decay. Mass measurements relevant to atomic physics and physical chemistry are described in Chapter 4. Dipole measurements are discussed in Chapter 5. Finally, Chapter 6 is a summary of the work contained in this dissertation as well as possible future measurements.

2. EXPERIMENTAL APPARATUS AND TECHNIQUES

2.1 Penning Trap Introduction

The theory of Penning traps has been discussed in detail in a review by Brown and Gabrielse [71] as well as in all the MIT theses [31-39] and Matthew Redshaw's thesis [66]. I will only introduce the most important ideas and highlight the new developments to the system in the last few years.

It is well known that a charged particle within a magnetic field undergoes circular motion, known as the cyclotron motion, at an angular frequency [72]:

$$\omega_c = \frac{qB}{m} \qquad [2.1]$$

where q is the ion's charge, m is the ion's mass and B is the magnetic field. The basic idea behind the Penning trap is to utilize the ratio of two different ions' cyclotron frequencies to obtain the mass ratio of those ions. There is an abundance of complications to this idea. While the magnetic field (8.5 T for the FSU-PPT) confines the ion radially, a quadropole electric potential of the form

$$\Phi(\vec{r}) = \frac{V}{2}\left(\frac{z^2 - \frac{1}{2}\rho^2}{d^2}\right) \qquad [2.2]$$

is used to confine the ion axially, where d is the characteristic trap size parameter given in terms of the axial and radial trap dimensions z_0 and ρ_0 by

$$d^2 = \frac{1}{2}\left(z_0^2 + \frac{\rho_0^2}{2}\right). \qquad [2.3]$$

This potential is realized with voltages applied to a ring electrode and two end-cap electrodes (upper and lower). To confine positive ions, the ring must be biased negatively with respect to the end caps. These electrodes are located on equipotential surfaces of the potential described by Equation 2.2.

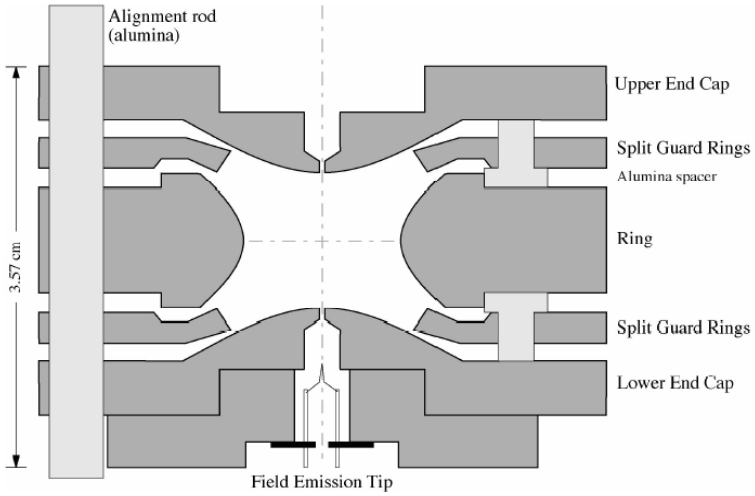

Figure 2.1 Cross-section of the FSU-PPT electrodes

The electrostatic potential introduces a harmonic oscillatory axial motion along the magnetic field lines, modifies the cyclotron frequency and introduces a second circular motion called the magnetron motion. The magnetron motion consists of a relatively slow drift about the electrostatic axis of the trap resulting from the balance between the $\vec{v}x\vec{B}$ magnetic force and the outward pull of the electrostatic field. Therefore, the resulting motion of an ion inside a Penning trap is comprised of three distinct modes each with its own frequency: axial (ω_z), magnetron (ω_m), and trap (modified) cyclotron (ω_{ct}). In a perfect Penning trap with ring voltage V_R, with an ion of mass m and charge q, these three eigenfrequencies are given by:

$$\omega_z = \sqrt{\frac{qV_R}{md^2}} \qquad [2.4]$$

$$\omega_m = \frac{\omega_c}{2}\left(1 - \sqrt{1 - \frac{2\omega_z^2}{\omega_c^2}}\right) \qquad [2.5]$$

$$\omega_{ct} = \frac{\omega_c}{2}\left(1 + \sqrt{1 - \frac{2\omega_z^2}{\omega_c^2}}\right) \qquad [2.6]$$

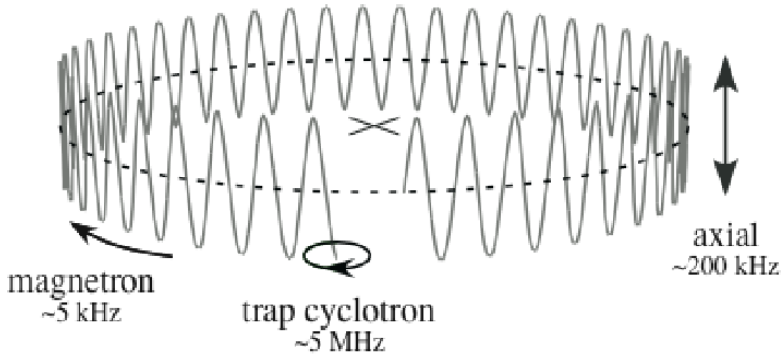

Figure 2.2 The three harmonic modes in a Penning Trap

Remarkably, for a uniform magnetic field and purely *quadratic* electrostatic potential, all three motions are harmonic, meaning their frequencies are independent of the amplitude of their motion[6]. Also remarkably, the "true" cyclotron frequency ω_c that the ion would have in a uniform magnetic field without the electrostatic potential, can be obtained from the observable frequencies, namely the trap cyclotron frequency, the magnetron frequency, and the axial frequency, by means of the Brown-Gabrielse Invariance Theorem [71]:

$$\omega_c^2 = \omega_{ct}^2 + \omega_m^2 + \omega_z^2 \qquad [2.7]$$

The power of this theorem lies in the fact that it remains exact for a real Penning trap in which there will be some misalignment of the trap electrostatic axis relative to the magnetic field and the quadratic potential near the ion's equilibrium position will not be perfectly cylindrical. Due to the hierarchy $\omega_{ct} >> \omega_z >> \omega_m$, only ω_{ct} must be measured to the same fractional precision as is desired for ω_c.

2.2 Atomic Mass Measurement Process

To obtain a mass ratio it is necessary to measure the ratio of cyclotron frequencies of two different ions in the same magnetic field. The time variation of the magnetic field in the trap necessitates measuring the two cyclotron frequencies as simultaneously as possible.

Before the development of the "swapping" technique described in Section 2.2.5, the normal operating procedure was to make one ion, measure its cyclotron frequency, "kill" that ion (see Section 2.2.1), then make an ion of the different species, measure its cyclotron frequency

[6] This is actually only true in the non-relativistic limit.

and repeat. To minimize the time between measurements of two different ions' cyclotron frequencies, a swapping procedure has been developed. This technique allows two ions to be trapped in the Penning trap simultaneously. Therefore, the swapping procedure reduces the time between cyclotron frequency measurements and enables more interchanges in a given run time. The result is a reduction of the 'noise' of a ratio measurement due to magnetic field fluctuations.

The swapping procedure was initially developed at FSU by Matthew Redshaw [66] and further developed by myself, and is completely automated (once a pair of ions is made) using a massive LabView program originally designed at MIT called ICR-Master [38]. The swapping procedure would be very difficult to implement without ICR-Master, which manipulates and measures the cyclotron frequencies of pairs of ions in the FSU-PPT. This flexible system allows data to be taken with the two ions continuously, day and night, limited by the lifetime of the ions against collisions with background gas, and the need to refill a liquid nitrogen dewar of the cryogenic insert containing the Penning trap every 15 hours (see Figure 2.3).

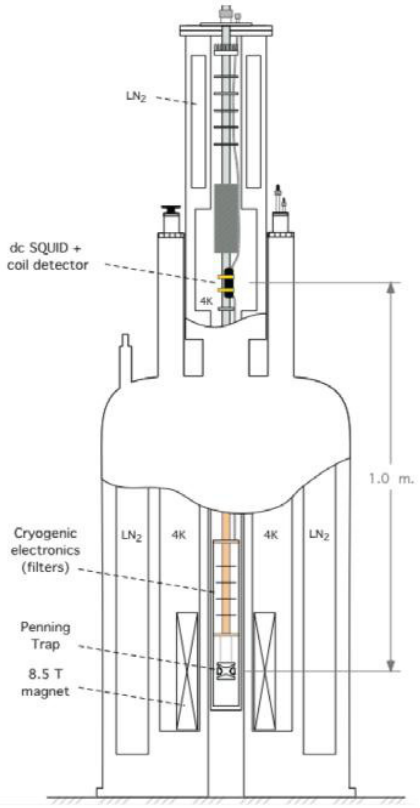

Figure 2.3 Penning trap apparatus.

2.2.1 Making Ions

The process of making ions involves letting a small amount of gas or vapor into the top of the insert, a tiny fraction of which enters the trap through a hole in the upper endcap, two meters below. A field emission point produces an electron beam, with 5-20 nA at 1 keV, which is used to ionize the neutral molecules or atoms by electron impact, see Figure 2.1. Unwanted ions (such as N_2^+) are always made out of background gas in the trap, possibly liberated by the electron beam hitting surfaces on which gases have condensed, as well as from the gas that we intentionally let in the trap. Multi-charged ions always involve large numbers of background ions. While making a single triply-charged ion, roughly 10 doubly charged ions and 100 singly charged ions are made. Since the "good" ion (the ion that we would like to trap) is near the resonance of our detection circuit and is therefore damped (see Section 2.2.4), it should have a smaller axial amplitude than the unwanted or "bad" ions. Therefore, lowering the voltage on the lower endcap will cause the bad ions to strike the endcap, hopefully leaving just the good ion in the trap (this we call a "dip").

In practice, we do a series of progressively stronger dips, making a "weaker" trap with a less negative ring or more negative lower end cap, before we deem an ion as "clean." We start with gentle dips because when an ion is made it may be axially excited by bad ions. With each dip more bad ions are killed, resulting in a less excited good ion able to withstand stronger dips. Mixed in with the dips are processes which we call "kills." These processes consist of exciting the axial motion of the bad ions by applying rf noise to the lower endcap and then doing a dip.

During ion making and the "clean-up" process, we continually monitor the FFT (see Figure 2.6) of the axial signal following pulsed excitation of the axial mode. The FWHM of the axial signal gives a clear indicator of the number of "good" ions, since the ring-down time is inversely proportional to the number of good ions. The signal amplitude also increases with the number of good ions. The presence of "bad" ions is indicated by distortion and non-reproducibility of the axial signal: with many bad ions, the good ion signal will not even be detectable. The presence of a single bad ion may lead to intermittent "bad peaks" from the good ion, depending on how close the bad ion's orbit is. Checking the stability of successive ring-downs of the axial frequency can also indicate "bad" ions (a single ion's axial frequency should be stable to about 0.03 Hz over a few minutes).

The process of producing a single ion of the desired species and charge state and eliminating contaminant ions can take a considerable amount of time: anywhere between fifteen minutes to days, depending on how difficult it is to make as well as the ion-making skill of the operator.

2.2.2 Making *Two* Ions

Section 2.2.1 described making a single ion in the trap. However, all the measurements in this dissertation were accomplished with *two* ions simultaneously trapped: one ion at the center, with the other ion in a large "parking" cyclotron orbit, generally of 1.5-2.5 mm radius (see Section 2.2.5). Simultaneously trapping two ions requires making a single ion, "cleaning" it up (removing all the unwanted ions), and then exciting it with a pulse at the trap cyclotron frequency to a large cyclotron orbit. The second ion can then be made at the center of the trap.

In our trap we observe that the "dip of death," or the dip voltage required to kill a single, axially damped ion, decreases in strength as an ion's cyclotron orbit increases. Therefore, keeping an ion in a large cyclotron orbit while cleaning the ion at the center of the trap can be tricky. The ion in the large orbit must be constantly monitored during the dip and kill process. Large cyclotron amplitudes can shift the axial frequency as much as 100-200 Hz (see Section 2.3.1), much larger than the bandwidth of our detector. In order to monitor the axial motion of an ion in a large cyclotron orbit, the ring voltage, V_r, and the guard ring voltage, V_{gr}, must be adjusted.

As discussed in Sections 2.3.1 and 2.3.2, a large cyclotron radius shifts the axial frequency:

$$\frac{\Delta\omega_z}{\omega_z} \approx \frac{3}{2}\frac{C_4}{d^2}\rho_c^2 + \frac{45}{16}\frac{C_6}{d^4}\rho_c^4 + \frac{1}{4}\frac{B_2}{B_0}\frac{\omega_c}{\omega_m}\rho_c^2 . \qquad [2.8]$$

Since the axial frequency has shifted, the ring voltage (see Equation 2.4) must be adjusted to bring the ion back on resonance with the detector circuit. Additionally, the axial motion of the ion becomes anharmonic. By adjusting the guard ring voltage to the value of C_4 which makes the derivative of the shift to the axial frequency with respect to the axial amplitude small, the motion may be made more harmonic. In principle this can be calculated, however in practice, it works best to simply use trial-and-error guided by the model, combined with past experience. The process of finding the "best" combination of V_r and V_{gr} then becomes an iterative process of

setting the voltages to one setting, and then optimizing until the ion's ring-down after an axial excitation is narrow and on resonance with the detector circuit.

2.2.3 Vapor Loader

Until the alkali measurements, the only measurements carried out at FSU were those that could be made using ions made from gases. As the demand for measurements grew, it became obvious that to move forward, the FSU-PPT needed to be able to work with metal vapors as well. A vapor loader had actually been developed at MIT and used in their alkali mass measurements [37]. It is designed to rest on a gate valve at the top of the insert to the trap (about 2 meters above the trap, see Figure 2.3) with a line-of-sight to the hole in the upper endcap. This vapor loader was completely rebuilt with various improvements. Inside the vapor loader, an "element" is attached to two copper electrical feed-throughs which extend outside the vapor loader. The ends of the rods are attached to a current source, which electrically heats the element. The currents used for heating the elements varied from 5-15 A. This set-up lets small, controllable amounts of metal vapor into the trap (see Figure 2.4).

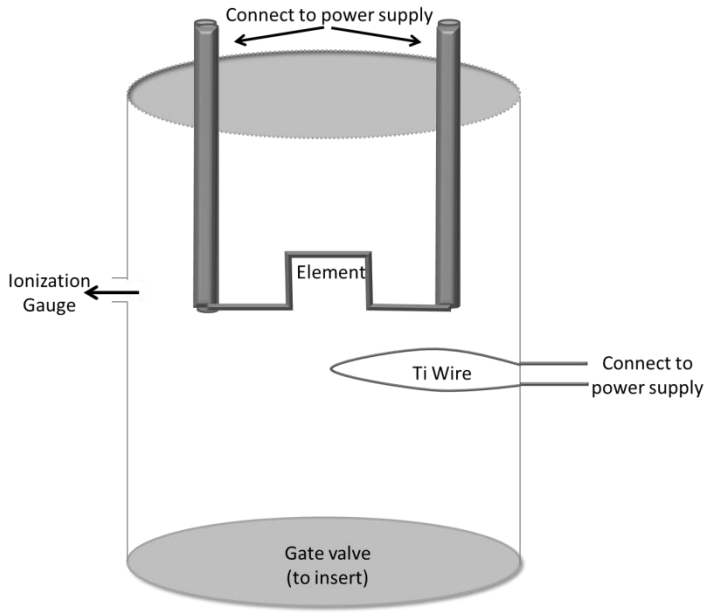

Figure 2.4 Rough schematic of the vapor loader. Since its use at MIT, the titanium wire, ion gauge and bellows (not shown here) were all added.

We used two different kinds of elements: alkali metal dispensers supplied by SAES Getters, and homemade. The elements from SAES Getters were designed to make very pure alkali films and contain alkali metal chromate and a reactive agent, which release small amount of pure alkali vapor when heated [73]. The homemade dispenser was roughly modeled on the alkali dispensers and consisted of a slit tube about 1 mm in diameter made of either stainless steel or niobium (see Figure 2.5). This tube was partially stuffed with a few mg of metal foil or oxide powder.

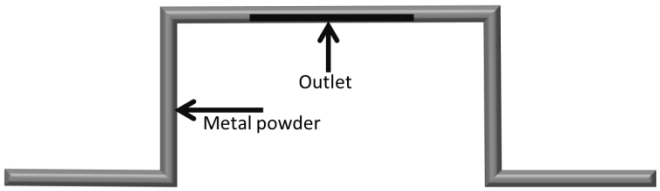

Figure 2.5 Sketch of a homemade element. One of the legs contains metal powder, which vaporizes when heating, flowing to the outlet. A tiny fraction (<0.0001%) of this vapor enters the trap.

In addition to making homemade elements, other additions were made to the vapor loader as it was known at MIT: a bellows was added to the bottom of the vapor loader, and a tilt stage (in fact a modified laser mirror mount) in order to enable the alignment of the element with the hole in the top endcap; an ionization gauge was used to monitor the vacuum in the vapor loader; and a titanium wire, which was heated for several hours before operating the vapor loader, was used as an evaporable getter to improve the vacuum.

2.2.4 Measuring the Cyclotron Frequency: Pi Pulses and PNPs

In the FSU-PPT, the axial motion of the ion is the only mode detected directly. This is accomplished by measuring the image current induced in a circuit connected between the upper and lower endcaps of the trap utilizing a high-Q (resonator "quality factor") inductor (which is called "the coil" because it is indeed a toroidal coil of niobium wire [74]) coupled to a DC SQUID [75]. In the process, the axial motion is damped by a back electromotive force from the detector circuit. Typically, the axial motion is excited using a 1 ms rf pulse centered 500 Hz below the axial frequency or using a "PNP" (see next paragraph). The resulting damped

sinusoidal "ring-down" is detected, and analyzed online to provide the amplitude, phase and frequency of the ion's axial motion [66]. The Fourier transform of the axial ring-down signal of an ion is shown in Figure 2.6.

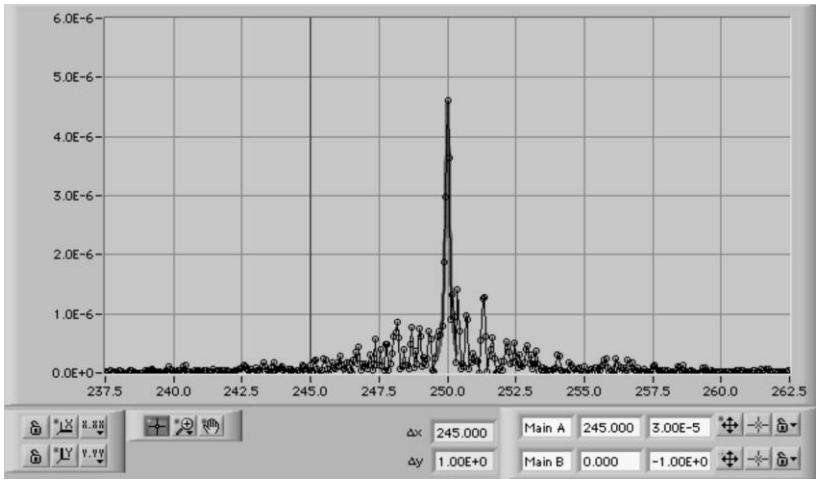

Figure 2.6 Fast Fourier Transform (FFT) of an ion's axial ring-down signal as it appears on the screen of ICR-Master (a LabView program developed specifically for this Penning trap at MIT).

The **P**ulse a**N**d **P**hase (PNP) technique [76] is used to determine the modified cyclotron frequency of an ion in the trap and this method is currently unique to the FSU-PPT. In the PNP technique, an rf pulse, applied to one half of one of the guard ring electrodes in the trap, excites the ion into a small cyclotron orbit (50-150 μm). The ion is then allowed to continue in its cyclotron motion, that is, "evolve cyclotron phase" for a predetermined amount of time called the evolution time, T_{evol}. A cyclotron-to-axial rf coupling pulse (π-pulse[7]) then transfers the classical action of this small cyclotron orbit into axial motion. This resulting axial motion is then damped and detected by the SQUID (Super-conducting quantum interference device). The axial ring-down signal is typically recorded for four to eight seconds and is analyzed online to obtain a phase, frequency and amplitude. The phase of the ring-down corresponds directly to the phase of the cyclotron motion at the time the π-pulse was applied, and hence effectively gives the final cyclotron phase.

[7] A "π-pulse" refers to the correct product of pulse amplitude and duration for complete conversion from one mode to another [76]. The correct duration of a π-pulse is measured using the avoided crossing method [66], and is referred to as the π-pulse time.

To obtain a single measurement of ω_{ct}, the PNP process is repeated ten times, each with a different evolution time, from 0.2-58 sec, producing ten measurements of the phase φ_{ct} and axial frequency ω_z of the ion. This set of ten PNPs (each with a different φ_{ct} and T_{evol}) is referred to as a PNP cycle. The modified cyclotron frequency of the ion is then determined by fitting the graph of φ_{ct} versus T_{evol} with a straight line and noting the relation:

$$\omega_{ct} = \frac{d\phi_{ct}}{dT_{evol}} \qquad [2.9]$$

The modified cyclotron frequency is hence mainly determined by the phase of the PNPs with the longest T_{evol}s[8]. However, the values of the phases returned are within the range ±180º, i.e. are modulo 360º, therefore the total number of revolutions must be predicted using the initial measurements of the cyclotron frequency from the "avoided crossing" technique, and obtaining successively more precise estimates of f_{ct} by working from shorter to longer T_{evol}s, see Reference [66].

The axial frequency is obtained by averaging the ten measurements of ω_z (one ω_z measurement from each PNP) obtained from the PNP cycle. Once the axial and modified cyclotron frequencies have been determined, the magnetron frequency is obtained using the formula [71]:

$$\omega_m \cong \frac{\omega_z^2}{2\omega_{ct}}\left[1+\frac{9}{4}\sin^2\theta_{mag}\right] \qquad [2.10]$$

where θ_{mag} is an angle characteristic to the trap and may also be measured using the avoided crossings technique. Now that all three eigenfrequencies have been measured, the free space cyclotron frequency may be calculated using the Brown-Gabrielse Invariance Theorem (Equation 2.7). Typically, the cycle of ten PNPs yields a single measurement of ω_c to about a $3\text{x}10^{-10}$ precision in the ratio and lasts about ten minutes. The PNP technique allows precise measurement of the trap cyclotron frequency. This technique sets the FSU-PPT apart from other Penning traps.

2.2.5 Swapping Ions

The swapping process begins with one ion in the center of the trap (the inner ion) and another in a large cyclotron orbit with radius of generally 2.0-2.5 mm (the outer ion). Cyclotron

[8] If the phase of a 58 sec T_{evol} PNP at f_{ct} = 5 MHz is determined to 30 degrees, then f_{ct} is determined to 3 x 10^{-10}.

frequency measurements of the inner ion are carried out and then the ions are swapped. The first step of the swapping process consists of reducing ("cooling") the orbital radius of the outer ion to a radius of approximately 1 mm. A pulse at the trap cyclotron frequency is then applied to the inner ion, pushing it into the large orbit. The former outer ion is subsequently cooled to the center of the trap and its cyclotron frequency is measured using the PNP technique, etc. This procedure of swapping the ions can take anywhere from five to fifteen minutes depending on the outer ion's radius.

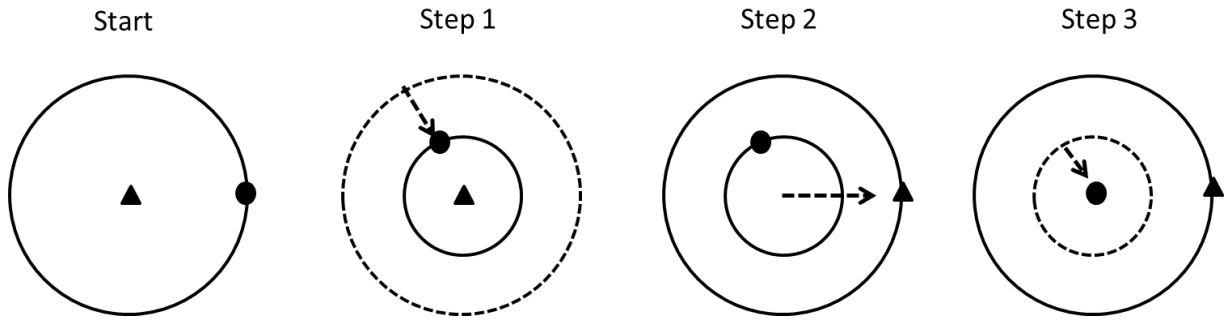

Figure 2.7 Swapping Procedure. Start: One ion is at the trap center, the other is in a large (2.0-2.5 mm) orbit. Step 1: The ion formerly in the large orbit is now cooled to about 1 mm. Step 2: The ion formerly at the trap center is "kicked" out to the large cyclotron orbit. Step 3: The ion at the 1 mm orbit is now cooled completely.

The swapping time is completely dominated by the time involved in cooling the ion. Unfortunately, since we do not know the phase of the ion in its large cyclotron orbit, we cannot simply use a single pulse at the modified cyclotron frequency to drive the ion to the center of the trap. Instead*, partial*[9] π-pulses at the cyclotron-to-axial coupling frequency are used. Each partial π-pulse converts a bit of cyclotron amplitude into axial amplitude. A large cyclotron amplitude shifts the axial frequency (see Section 2.3.1), so the ring and guard ring voltages must be shifted to bring the axial amplitude resulting from each π-pulse onto resonance with our detector circuit to then be damped (see Section 2.2.4). Since the cyclotron radius is shrinking, the ring and guard ring voltages must be changed constantly (see Equation 2.8).

[9] A "partial π-pulse" is a pulse applied at the cyclotron-to-axial coupling frequency, but with a shorter duration than a complete π-pulse. Instead of transferring all the cyclotron motion to axial motion, only part of the cyclotron motion is converted into axial motion. Such a pulse is needed for large cyclotron radii, because of the anharmonicity that a large resultant axial amplitude would cause.

The flexibility of ICR-Master allows "swapping scripts" to be set up for each *m/q*. Loops in the scripts may be set up to do a certain number of π-pulses at each guard ring and ring voltage setting. For example, commands may be written which "tell" ICR-Master to apply the coupling drive for *w* ms, *x* number of times, with guard ring voltage setting *y*, and ring voltage setting *z*. Therefore, in the ICR-Master script, there are 4 lists: partial π-pulse times, number of repeats, guard ring voltage, and ring voltage. These lists usually contain around 10-15 entries each. With each loop, the π-pulse times get closer to the full π-pulse times, and the ring and guard ring voltage settings get closer to the "normal" settings (the settings for an ion at the center of the trap).

Setting up such a script is time-consuming, and generally takes about a day, depending on the parking radius[10]. However, once a reliable algorithm has been found, data taking becomes almost completely automated. Since quite a bit of the data is taken at night, when no one is watching the script, it is essential that the script reliably cools the ion. To guard against possible problems, the script is set up to monitor the axial frequency of the ion after each partial π-pulse. If the axial frequency is outside of a 5-10 Hz imaginary box around the detector resonance, the ring voltage is adjusted to bring the ion back on resonance with the detector.

This technique of varying the ring and guard ring voltages while monitoring the axial frequency was developed during my time at FSU. This procedure has been extended for the use of multi-charged ions as well as for non-mass doublets. For the non-mass doublets, separate swapping script parameters (ring and guard ring voltages) are used for each ion, however the same number of partial π-pulses are applied to each ion, to ensure any heating effects [66] are even.

2.2.6 Ratio Measurement

A ratio measurement consists of several "runs," like the one in Figure 2.8. Normally, runs consist of three PNP cycles (see Section 2.2.4), followed by a swap of the ions (see Section 2.2.5), three PNP cycles of the other ion, then another swap, etc., repeated as many times as possible for up to 15 hours. An example run is shown in Figure 2.8.

[10] For future students: I think the easiest way to find the cooling algorithm for a new *m/q*-value is to start with a small radius (0.75-1 mm or so) and cool the ion from this point. Then, find the parameters that will cool the ion from a slightly larger radius to the first radius. Keep going to slightly larger radii, until you have obtained the script for the radius that you wish to take data with. This seems to produce a more reliable script than trying to find an algorithm starting with a large (2 mm or so) radius.

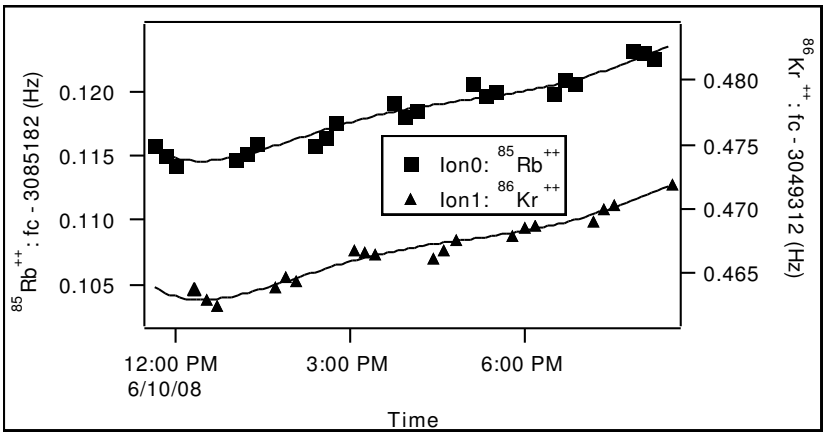

Figure 2.8 Typical cyclotron frequency ratio data. The cyclotron frequency of one ion at the center of the trap being measured, while another is "parked" in a large cyclotron orbit.

Both ions' cyclotron frequency data is fit simultaneously with a set of polynomials (with different constant terms) ranging from 0^{th} order (straight line with no slope) to an 8^{th} order polynomial. The so-called F-Test [77] is then used to determine the optimal fit for both curves. From the difference in the constant terms in this simultaneous fit, the ratio of the two ions' frequencies may be obtained. The cyclotron frequency data for one ion is first rescaled using a previous estimate of the ratio, to make the difference in the constant terms small.

2.2.7 Mass Difference and Resultant Mass

The mass differences and the ratio of the atomic masses may then be obtained from the cyclotron frequency ratio of the ions as shown in the following example. The ratio obtained from a run is equal to the inverse of the mass ratio of the ions. The masses of the two ions being compared can each be broken into the mass of its constituent atom(s) less the electron(s) mass plus the mass energy required to make the ion from its constituent atoms:

$$R = \frac{m\left(^{18}O_2^+\right)}{m\left(^{12}C_2D_6^+\right)} = \frac{2m\left(^{18}O\right) - m(e) + \Delta E\left(^{18}O_2^+\right)}{2m(C) + 6m(D) - m(e) + \Delta E\left(^{12}C_2D_6^+\right)} \qquad [2.11]$$

The energy required to make an ion from its components may be written in terms of the heats of formation at 0K ($\Delta_f H^0$) and the ionization energies, *IE,* as:

$$\begin{aligned}\Delta E &= \Delta_f H^0\left(^{12}C_2D_6^+\right) - 2\Delta_f H^0(C) - 6\Delta_f H^0(D) \\ &= \Delta_f H^0\left(^{12}C_2D_6\right) + IE\left(^{12}C_2D_6\right) - 2\Delta_f H^0(C) - 6\Delta_f H^0(D)\end{aligned} \qquad [2.12]$$

The mass of the electron and usually the heats of formation are known to more than the necessary precision, so the precision for the final mass depends mainly on the uncertainty of the measured cyclotron frequency ratios and of the reference masses.

2.3 Systematic Effects

While the swapping technique reduces random error associated with the magnetic field variation, there are many sources of systematic error which must be considered. In general, small shifts to the eigenfrequencies ω_{ct}, ω_z and ω_m are calculated, and their effect on ω_c is then determined using:

$$\frac{\Delta\omega_c}{\omega_c} \approx \frac{\Delta\omega_{ct}}{\omega_{ct}}\left(\frac{\omega_{ct}}{\omega_c}\right)^2 + \frac{\Delta\omega_z}{\omega_z}\left(\frac{\omega_z}{\omega_c}\right)^2 + \frac{\Delta\omega_m}{\omega_m}\left(\frac{\omega_m}{\omega_c}\right)^2 \qquad [2.13]$$

Once the shifts to the free-space cyclotron frequency in the imperfect trap have been determined for both ions, the resulting shift to the ratio is determined. The fractional shift to the ratio resulting from shifts of the free space cyclotron frequency for two ions, $\Delta\omega_0$ and $\Delta\omega_1$ is

$$\frac{\Delta R}{R} \approx \frac{\Delta\omega_0}{\omega_0} - \frac{\Delta\omega_1}{\omega_1} \qquad [2.14]$$

It is actually an imbalance in the fractional shifts of the cyclotron frequencies between the two ions which creates systematic shifts. Hence, by measuring mass doublets we achieve suppression of systematic shifts that are "common mode." Note that while Equation 2.14 gives the predicted shift to the cyclotron frequency ratio, to correct the observed cyclotron frequency ratios to obtain the desired inverse mass ratios, this shift must be subtracted.

2.3.1 Trap Imperfections: Electrostatics

The electrostatic potential in the Penning trap is not a pure quadrupole due to machining and assembly imperfections, the truncation of electrodes, and most importantly, due to "charge patches" on the electrode surfaces. In as much as the ion's motion averages over the azimuthal coordinate, the potential at the trap's center can be modeled as being cylindrically symmetric and may be approximated by the first few even terms in an expansion of Legendre polynomials P_n (reflection symmetry has also been assumed, see Reference [39] for discussion of odd terms):

$$\Phi(r,\theta) = \frac{V_R}{2}\sum_{n=0}^{\infty} C_n\left(\frac{r}{d}\right)^n P_n(\cos\theta) \qquad [2.15]$$

where V_R is the voltage of the end caps with respect to the ring electrode. From this expression for the electrostatic potential, the amplitude dependent (anharmonic) shifts to each normal mode frequency of an ion in the center of the trap may be calculated in terms of the axial, trap cyclotron and magnetron amplitudes (a_z, ρ_c and ρ_m, respectively). The values of C_n quantify the strength of the field imperfections with the C_2 term being the unperturbed term. In practice, only the C_4 and C_6 terms are generally relevant and the shift to the already small magnetron frequency is negligible. C_4 can be adjusted (or set to zero) by applying a variable voltage to the guard rings (see Figure 2.1). The leading order electromagnetic shifts to ω_{ct} and ω_z (and hence to ω_c, see Equation 2.13) given by this potential are therefore [38]:

$$\frac{\Delta\omega_z}{\omega_z} = \frac{3}{4}\frac{C_4}{d^2}\left(z^2 - 2\rho_c^2 - 2\rho_m^2\right) + \frac{15}{16}\frac{C_6}{d^4}\left(z^4 - 6z^2\rho_c^2 + 3\rho_c^4 - 6z^2\rho_m^2 + 12\rho_c^2\rho_m^2 + 3\rho_m^4\right) \quad [2.16]$$

and

$$\frac{\Delta\omega_{ct}}{\omega_{ct}} = -\frac{3}{2}\frac{\omega_m}{\omega_c}\frac{C_4}{d^2}\left(2z^2 - \rho_c^2 - 2\rho_m^2\right) - \frac{15}{8}\frac{\omega_m}{\omega_c}\frac{C_6}{d^4}\left(3z^4 - 6z^2\rho_c^2 + \rho_c^4 - 12z^2\rho_m^2 + 6\rho_c^2\rho_m^2 + 3\rho_m^4\right) \quad [2.17]$$

2.3.2 Trap Imperfections: Magnetic Field

Analogous to these electrostatic shifts, the dominant shifts due to the magnetic field non-uniformity are [38]:

$$\frac{\Delta\omega_z}{\omega_z} = \frac{1}{4}\frac{B_2}{B_0}\left(\rho_m^2 + \frac{\omega_c}{\omega_m}\rho_c^2\right) \quad [2.18]$$

$$\frac{\Delta\omega_{ct}}{\omega_{ct}} = \frac{1}{2}\frac{B_2}{B_0}\left(z^2 - \rho_c^2 - \rho_m^2\right) \quad [2.19]$$

where B_0 and B_2 are expansion coefficients of the magnetic scalar potential ψ, where $B = -\nabla\psi$ (Note: A more complete description is given in Reference [38]). The auxiliary measurements needed to determine the various expansion coefficients are described in Section 2.4.

2.3.3 Trap Imperfection: Equilibrium Position

In addition to the amplitude-dependent shifts in the free-space cyclotron frequency due to the trapping field imperfections, there may also exist a non-amplitude dependent shift in the ratio due to linear gradient in the magnetic field in the trap. Suppose there is a linear term in the axial

coordinate of the magnetic field such that $B(z) = B_0 + B_1 z$. If the ion of interest's axial equilibrium position in the trap were different than the reference ion's, this linear term in the magnetic field would introduce a shift in the free-space cyclotron frequency of:

$$\frac{\Delta\omega_c}{\omega_c} = \frac{B_1}{B_0}\Delta z \qquad [2.20]$$

where Δz is the difference in axial position and is given by [66]:

$$\Delta z = -\frac{C_1 d^2}{2z_0}\frac{V_{LEC}}{V_R} \qquad [2.21]$$

where C_1 is a constant that relates the axial electric field seen by the ion due to the voltage difference across the endcaps to that of a parallel plate capacitor with the electrode spacing $2z_0$ and V_{LEC} is the effective voltage difference between the upper and lower endcaps, including any effects due to charge patches and contact potentials.

It is important to note the dependence of Δz on the ring voltage, which in turn carries a mass dependence. Therefore, this effect introduces a shift in a ratio of a non-perfect mass doublet, proportional to the difference in $1/m$.

2.3.4 Image Charge

An additional shift to the eigenfrequencies of an ion in a Penning trap is produced by the redistribution of the charge on the conducting trap electrode surfaces by the field produced by the ion itself. This surface charge redistribution is usually treated in terms of fictitious image charges [78]. This image charge creates an additional electric field as seen by the ion at the center of the trap. However, the shift in the mass ratio due to this additional field is small when comparing ions of the same charge state as is common practice for the FSU-PPT. It can be shown that image charge shifts produce a fractional shift in an ion's cyclotron frequency proportional to its mass. A detailed discussion and analysis of these shifts is given in Reference [66].

2.3.5 Ion-Ion Interactions

Another contribution to the overall potential experienced by an ion near the center of the trap must be of course the Coulomb potential due to the ion in the large orbit. To first order, this interaction may be modeled by averaging over the orbit of the outer ion to produce a ring of

charge q_k and radius ρ_{ck}, where q_k and ρ_{ck} are the charge and cyclotron radius of the parked outer ion.

In analogy to the trap electrostatic imperfections, the perturbation to the electrostatic potential seen by the inner ion can also be written in terms of a Legendre polynomial expression. Following the discussion given in Jackson (pg 103) [78], the expansion coefficients are given by:

$$C_l(\rho_{ck}) = \frac{2\Omega_z}{\omega_z} P_l(0) \left(\frac{d}{\rho_{ck}}\right)^{l-2} \qquad [2.22]$$

where

$$\Omega_Z = \frac{\Omega_E^2}{\omega_z} \qquad \text{and} \qquad \Omega_E^2 = \frac{q_i q_k}{4\pi\varepsilon_0 m_i \rho_{ck}^3} \qquad [2.23,24]$$

where q_i and m_i are the charge and mass of the inner ion [79]. The shifts to the cyclotron and axial frequencies due to the ring of charge may then be obtained:

$$\frac{\Delta\omega_{ct}}{\omega_{ct}} \approx \left(\frac{\omega_z}{\omega_{ct}}\right)^2 \left(\frac{\Omega_z}{\omega_z}\right) \left[\frac{1}{2} + \frac{9}{16}\left(\frac{\rho_{ci}}{\rho_{ck}}\right)^2 + \frac{75}{128}\left(\frac{\rho_{ci}}{\rho_{ck}}\right)^4 + \ldots\right] \qquad [2.25]$$

and

$$\frac{\Delta\omega_z}{\omega_z} \approx \left(\frac{\Omega_z}{\omega_z}\right) \left[-\frac{1}{2} + \frac{9}{16}\left(\frac{a_{zi}^{\max}}{\rho_{ck}}\right)^2 - \frac{75}{128}\left(\frac{a_{zi}^{\max}}{\rho_{ck}}\right)^4 + \ldots\right] \qquad [2.26]$$

If the frequencies of the motions of the two ions are close (the difference of the axial frequencies of the ions is not much greater than Ω_z, then dynamical effects must also be considered. For example, one ion excites motion in the second which resonantly back acts on the first and so on, thereby shifting the eigenfrequencies.

2.3.6 F_z Shifts: Ion-Detector Interaction (Coil Pushing)

Yet another source of error is the so-called coil-pushing shift to the axial frequency. This coil (inductor), mentioned briefly in Section 2.2.4 is part of a resonant tuned LC circuit which causes the ion's axial motion to be damped and enables it to be detected. The interaction of the tuned circuit and the ion's axial motion causes the ion's axial frequency to be perturbed: it is "pushed" away from the resonant frequency of the coil. The shift to the ion's axial frequency, ω_z, can be obtained from ac circuit theory and has a dispersion form, namely [66]:

$$\Delta\omega_z^{CP} = \left(\frac{\gamma_0\gamma_z}{4}\right)\frac{(\omega_z - \omega_0)}{(\omega_z - \omega_0)^2 + \left(\frac{\gamma_0}{2}\right)^2} \quad [2.27]$$

where (all in angular units) ω_z is the unperturbed axial frequency, ω_0 is the resonant frequency of the coil, and γ_0 is the full-width at half-maximum of the coil resonance. The inverse of the ring-down time of the ion, γ_z, is given by:

$$\gamma_z = \frac{1}{\tau} = \frac{Q\omega_0 L}{m}\left(\frac{qC_1}{2z_0}\right)^2 \quad [2.28]$$

in terms of the known values of the coil Q, inductance L, the constant C_1, the axial trap dimension z_0, the mass of the ion m, and charge of the ion q.

2.3.7 F_z Shifts: Differential Voltage Drift

This systematic effect is subtle and generally only effects measurements of non-doublet masses. As explained in Section 2.2.4, a single measurement of ω_{ct} consists of ten PNP measurements, also known as a PNP cycle. With each PNP, a ring-down and therefore an axial frequency is recorded. The question then is: which axial frequency measurement should we combine with the trap cyclotron frequency measurement to obtain the free space cyclotron frequency?

Currently, we are using the average of the ten ω_z measurements from each PNP cycle. However, due to the varying length of the evolution times of our PNPs, this average may not correspond to the measurement time of the trap cyclotron frequency [66], which is determined by the time, in the cycle of 10 PNPs, of the two long T_{evol} PNPs. If there is a drift in the axial frequency during the PNP measurements, there will be a systematic shift in the resultant free space cyclotron frequency. However, if both ions' axial frequencies are drifting at the same rate and direction, the systematic shift will cancel in the ratio (see Equation 2.14).

The axial frequency is dependent on the charge and mass of the ion, the characteristic trap size, and the ring voltage as shown in Equation 2.4. The voltages for the trap are controlled by a very stable voltage source we call the V-box (as well as add-on computer voltages)[11]. The V-box contains two "channels," or potentiometer settings to be used in the case of non-doublet

[11] The add-on computer voltages are small compared with the voltage from the V-box. They are essential in allowing changing voltages (for example ring and guard ring voltages during a swapping script) without having to manually adjust the potentiometers of our voltage source.

masses, where the add-on computer voltage does not have the range to accommodate both ions' voltages. In the case of non-doublet masses, there is the possibility for the two ions' ring voltages (and therefore axial frequency) to drift in different directions, causing a systematic shift to the free space cyclotron frequency.

2.4 Trap Characterization

The trap imperfection Δ_{trap} (Sections 2.3.1, 2.3.2, 2.3.3, 2.3.4), ion-ion interaction $\Delta_{i\text{-}i}$ (Section 2.3.5), coil-pushing and differential voltage drift, Δ_{fz} (Sections 2.3.6, 2.3.7) shifts are currently the largest sources of systematic shifts in the FSU-PPT system. With the models outlined above, the data may be corrected for these effects, however uncertainty in these corrections remains. By obtaining the various parameters using auxiliary measurements and with careful analysis, it is usually possible to reduce the final systematic error in a mass ratio to below 10^{-10}, and in some cases to 10^{-11}.

The most important parameters for quantifying the systematic shifts and uncertainties of the measurements in this dissertation are the cyclotron radius ρ_c, the electrostatic imperfection terms C_4 and C_6 (see Sections 2.4.4, 2.4.5), and the magnetic field imperfection terms B_1 and B_2 (see Section 2.4.1). The magnetic field characterization will be discussed first, followed by the methods in which we determine ρ_c and then C_4 and C_6.

2.4.1 Magnetic Field "Event" of January 2009 and Characterization

Using the known charge and the mass of an ion, the magnetic field may be calculated from the cyclotron frequency to follow the long term drift of the magnetic field of our superconducting magnet. The recorded magnetic field variation since the relocation of the trap is shown in Figure 2.9.

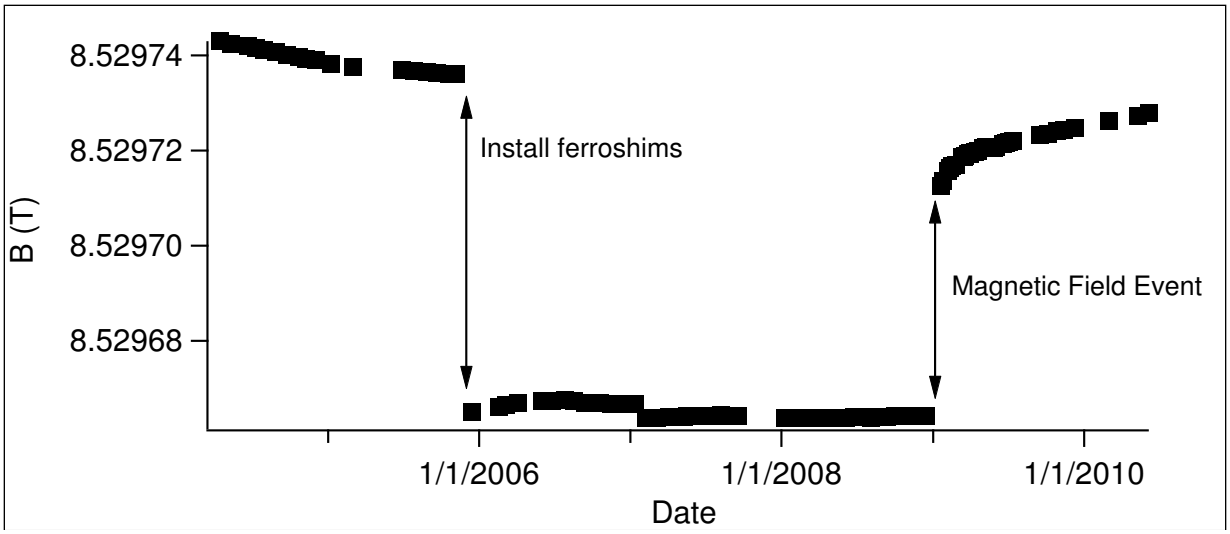

Figure 2.9 Magnetic field variation since the start of measurements at FSU.

The installation of the ferroshims in 2005, in order to reduce B_2, caused an expected decrease in the constant magnetic field, B_0, and was discussed in [66]. In January 2009, a sudden, spontaneous increase in the magnetic field occurred. This jump occurred between the measurements of the ^{76}Ge and ^{74}Se Q-values (see Section 3.1). In addition to B_0, a measurement of B_1 was also made at this time by varying the lower endcap voltage and looking for a shift to the cyclotron frequency due to Equations 2.20 and 2.21. It was found that B_1 had increased from -1.8(5) x 10^{-8} to 2.8(1.0) x 10^{-8} mm^{-1}. A measurement of B_2 was also made (see next Section) and it was found that it had jumped from -5(3) x 10^{-9} mm^{-2} to 8(5) x 10^{-8} mm^{-2}. Whereas before the magnetic field event, the systematic shifts due to B_1 and B_2 could be neglected, after they could not.

2.4.2 Obtaining Cyclotron Radii

Since the ion-ion interactions depend upon the cyclotron radii, it is vital that the absolute radii are determined reliably. Since there is no meter stick within the Penning trap, we rely on a linear relation between the product of the voltage amplitude of the cyclotron drive (at the frequency synthesizer) and the duration of the drive pulse and the cyclotron radius produced. Hence we assume a calibration between the drive and the absolute radius:

$$\rho_c = \rho_c^{cal}(CDT)(CDA) \qquad [2.29]$$

where ρ_c^{cal} is the calibration constant, *CDT* is the cyclotron drive time, and *CDA* is the cyclotron drive amplitude. *CDT* and *CDA* are well-controlled, so the crucial parameter to determine is ρ_c^{cal}. (Note a similar equation can be written for the magnetron radius.)

ρ_c^{cal} depends on cyclotron frequency. Using a reference ρ_c^{cal} at one frequency, we obtain values at different frequencies in three ways. This $\rho_c^{cal}(ref)$ was measured using light ions, and the known shift to the cyclotron frequency due to special relativity:

$$\frac{\Delta\omega_c}{\omega_c} = -\frac{\omega_c^2}{2c^2}\rho_c^2 \qquad [2.30]$$

The following expressions enable the transfer of $\rho_c^{cal}(ref)$ to a ρ_c^{cal} of a different mass. The first method compares the axial amplitudes resulting from PNPs between the mass being considered and the reference mass using

$$\rho_c^{cal}(m) = \sqrt{\frac{f_{ct}^{\ ref}}{f_{ct}(m)}}\left(\frac{q^{ref}}{q(m)}\right)\left(\frac{a_z(m)}{a_z^{\ ref}}\right)\rho_c^{cal}(ref) \qquad [2.31]$$

where the ratio of the axial amplitudes are measured from the runs.

The second method compares the π-pulse times obtained with the avoided crossings method. This value may be calculated using the relation

$$\rho_c^{cal}(m) = \rho_c^{cal}(ref)\sqrt{\frac{m}{m^{ref}}}\left(\frac{t_\pi^{\ ref}}{t_\pi(m)}\right)\left(\frac{CCA^{ref}}{CCA(m)}\right) \qquad [2.32]$$

where t_π is the π-pulse time and *CCA* is the cyclotron coupling amplitude used in the avoided crossing.

The third method of evaluating ρ_c^{cal} is to use the f_z vs ρ_c vs V_{gr} method discussed in the next section. For an example of these measurements, see Section 3.1.2.

2.4.3 Measuring Amplitude Dependent Frequency Shifts: f_z vs ρ_m and ρ_c

Probing the amplitude dependent shifts of the ion requires varying a motional amplitude and recording the observed frequency shifts. Although in general there are three motional amplitudes that each affect three frequencies, in practice we can obtain the parameters we require to determine the systematic shifts from just two sets of measurements of shifts to the axial frequency.

***f_z* vs *ρ_m* vs *V_{gr}*.** According to Equation 2.17, the largest systematic shift to the axial frequency for an ion with a large magnetron radius and a small cyclotron radius and axial amplitude is

$$\frac{\Delta\omega_z}{\omega_z} = -\frac{3}{2}\frac{C_4}{d^2}\rho_m^2 + \frac{45}{16}\frac{C_6}{d^4}\rho_m^4 \qquad [2.33]$$

where $\rho_m = \rho_m^{cal}(MDT)(MDA)$ and $C_4 = \frac{D_4\left(V_{gr} - V_{gr}^0\right)}{V_R}$. [2.34,35]

D_4 is a constant of our trap [38], *MDT* is the time the magnetron drive is applied (ms), *MDA* is the amplitude at which the magnetron drive is applied (V_{pp}), V_{gr} is the guard ring voltage, $V_{gr}^{\ 0}$ is the guard ring voltage which makes C_4 zero. Therefore, by varying the magnetron radius and guard ring voltage, and measuring the resultant f_z shift, $V_{gr}^{\ 0}$ and C_6 may be measured [66].

***f_z* vs *ρ_c* vs *V_{gr}*.** According to Equation 2.17, the largest systematic shift to the axial frequency for an ion with a large cyclotron radius and a small magnetron radius and axial amplitude is

$$\frac{\Delta\omega_z}{\omega_z} = \left(-\frac{3}{2}\frac{C_4}{d^2} + \frac{1}{4}\frac{B_2}{B_0}\frac{\omega_c}{\omega_m}\right)\rho_c^2 + \left(\frac{45}{16}\frac{C_6}{d^4}\right)\rho_c^4. \qquad [2.36]$$

If $V_{gr}^{\ 0}$ has been determined from the f_z vs ρ_m vs V_{gr} measurement, then B_2 may be determined from this measurement. Likewise, if C_6 has been determined from the f_z vs ρ_m vs V_{gr} measurement, then the ratio of the $\rho_c^{\ 4}$ terms from this measurement, and a measurement conducted at the reference mass will yield a value for $\rho_c^{\ cal}$ at this mass.

3. CYCLOTRON FREQUENCY MEASUREMENTS FOR NUCLEAR APPLICATIONS

3.1 Q-value Measurements for Neutrinoless Double Beta Decay and Double Electron Capture

3.1.1 Motivations

3.1.1.1 Neutrinoless Double Beta Decay

Double beta decay is the process in which a nucleus with Z protons and mass number A emits two electrons and transforms into a nucleus with $Z+2$ protons while maintaining mass number A via the conversion of two neutrons into two protons. In "ordinary" double beta decay ($2\nu\beta\beta$), two electron antineutrinos are emitted in addition to the two electrons. This process was observed in the laboratory for the first time in 1987 [80]. It gives no information as to whether neutrinos are Majorana particles (particles that are their own antiparticles).

Another form of double beta decay has been postulated, however: *neutrinoless* double beta decay ($0\nu\beta\beta$). This process does not emit any neutrinos: it therefore violates lepton number conservation and requires that neutrinos are Majorana particles [81]. Further, the rate at which this process occurs would help in the determination of an absolute neutrino mass scale.

Atmospheric, solar and nuclear reactor neutrino oscillation experiments have shown that neutrinos indeed have mass, but only give information on the differences in the squares of these masses. There exist two of these $\Delta m^2 = |m_i^2 - m_j^2|$ values, usually labeled in the literature as Δm^2_{atm} [82] and Δm^2_{sol} [83]. These two values can be arranged to construct two different possible mass hierarchies: normal and inverted [84] (see Figure 3.1).

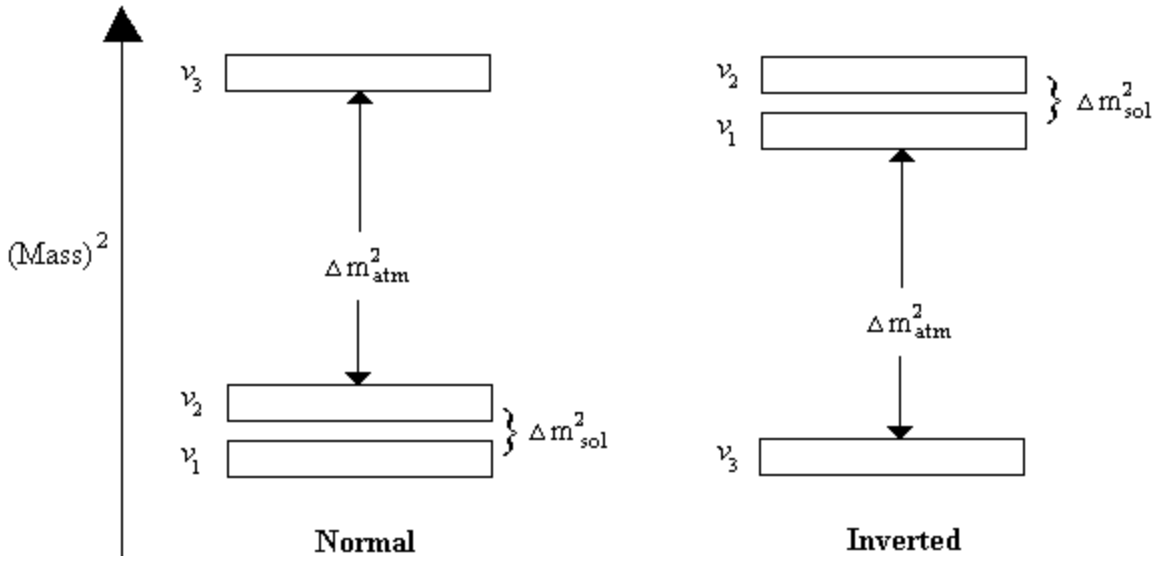

Figure 3.1 Possible neutrino mass hierarchies [84]

While the very observation of 0νββ would indicate neutrinos are Majorana particles, additionally, a measurement of the half-life, $T_{1/2}$, of the decay would provide information about the absolute mass scale of the neutrinos since

$$\left(T_{1/2}^{0\upsilon}\right)^{-1} \propto \left\langle m_{\beta\beta} \right\rangle^2 \qquad [3.1]$$

where $<m_{\beta\beta}>$ is the effective Majorana mass of the electron neutrino [85] and is related to the neutrino mass eigenstates m_i by

$$\left\langle m_{\beta\beta} \right\rangle \equiv \left| \sum_i m_i U_{ei}^2 \right|. \qquad [3.2]$$

where the neutrino-mixing matrix, $U_{\alpha i}$, relates the three mass eigenstates, $|\upsilon_i>$, and three flavor eigenstates, $|\upsilon_\alpha>$, of the neutrinos [86]:

$$\left|\upsilon_i\right\rangle = \sum_i U_{\alpha i} \left|\upsilon_\alpha\right\rangle \qquad [3.3]$$

where α runs over the flavor eigenstates: *e, μ* and *τ*. The index *i* indicates the mass eigenstates: *1, 2* and *3*. This neutrino-mixing matrix transforms states with well-defined mass into states with well-defined flavor [86].

The signature of 0νββ is a peak in the spectrum of the sum of the kinetic energies of the two emitted electrons at the decay's *Q*-value. Here, the *Q*-value is the mass-energy of the products subtracted from the mass-energy of the parent nucleus. This can be determined by

precise measurement of the mass difference between the parent and the daughter atoms.

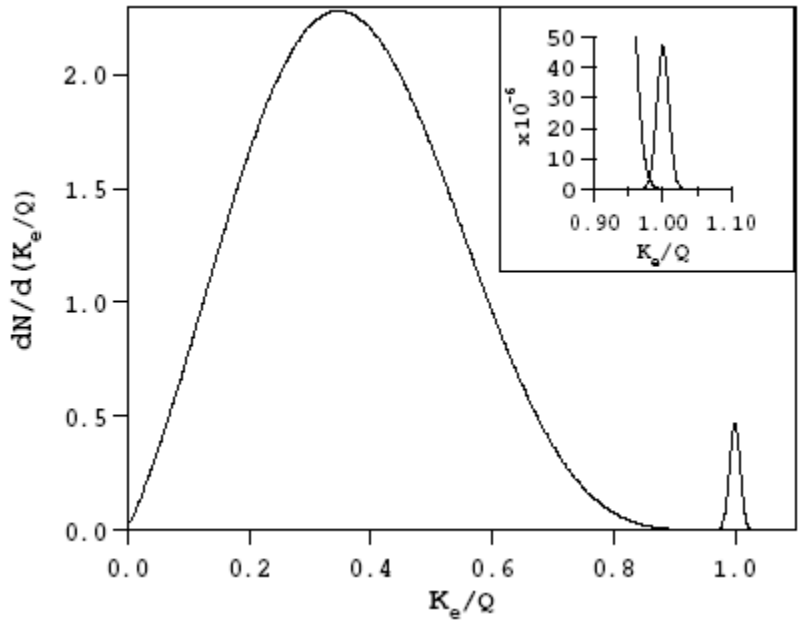

Figure 3.2 Double beta decay total electron energy spectrum [84].

The larger, broader peak in the spectrum in Figure 3.2 is due to 2νββ. The total energy spectrum of these electrons is peaked at about half that of the 0νββ electrons because they must share the released energy with the emitted neutrinos, whereas in 0νββ, the electrons contain all the emitted energy of the reaction. Since the 0νββ peak is always much smaller than the 2νββ peak and overlaps its tail, it is essential to obtain a precise *Q*-value for which to search in order to differentiate any suspected 0νββ peak from fluctuations in the 2νββ electron spectrum, as well as from background peaks from various sources [85].

There are several candidate nuclei in the search for 0νββ, most of which have been or are currently involved in the many searches for 0νββ worldwide [84,85]. These candidates possess essential qualities: they must be unstable against double beta decay (they are more massive than their (Z+2, A) daughter atom), yet must be stable against single beta decay to the (Z+1, A) nuclide to avoid being overwhelmed by background. It is also important that the *Q*-value for the 0νββ decay be high to maximize the transition rate. A list of the most prominent candidates as

well as their 0νββ *Q*-values are given in Table 3.1.

Table 3.1 Neutrinoless double beta decay candidates. Note that the *Q*-values for the ^{76}Ge, ^{130}Te, and ^{136}Xe decays are the current, most precise FSU-PPT values [68,87,88] and the *Q*-values of the ^{100}Mo and ^{150}Nd decays were measured by the JYFLTRAP [45,89]. All other masses were obtained from the 2003 AME [90]. Any conversion factors were taken from CODATA [91].

Parent	Daughter	*Q*(keV)	Error (keV)
^{48}Ca	^{48}Ti	4273.42	4.56
^{76}Ge	^{76}Se	2039.061	0.007
^{82}Se	^{82}Kr	2995.50	3.82
^{96}Zr	^{96}Mo	3347.70	4.75
^{100}Mo	^{100}Ru	3034.40	0.17
^{110}Pd	^{110}Cd	2003.55	3.82
^{116}Cd	^{116}Sn	2808.45	5.59
^{124}Sn	^{124}Te	2287.75	2.89
^{130}Te	^{130}Xe	2527.518	0.013
^{136}Xe	^{136}Ba	2457.83	0.37
^{150}Nd	^{150}Sm	3371.38	0.20
^{160}Gd	^{160}Dy	1729.41	5.03

The experiments that have thus far obtained the highest sensitivity for detecting 0νββ decay are those utilizing ^{76}Ge [92,93]. A subset of one of the large collaborations presenting ^{76}Ge data has even claimed to have observed 0νββ after reanalyzing the initially reported data [94]. This controversial claim based on data with poor statistics and unidentified background lines has been disputed [95]. Obviously for the 0νββ mechanism to be accepted as valid, there needs to be another observation by a different group and perhaps even with a different atomic species. There are many collaborations around the world developing apparatuses in this search, employing a variety of the candidates listed above.

One such collaboration is the CUORE experiment [96]. In March 2008, Frank Avignone, senior U.S. member of this experiment (currently at the University of South Carolina), contacted the FSU group concerning the *Q*-value for the ^{130}Te 0νββ decay. There is a need for a more precise value than the currently accepted *Q*-value of 2530.3 ± 2.7 keV [97]. In fact, the next-generation CUORICINO experiment currently being developed has an anticipated FWHM energy resolution of 5 keV and absolute energy calibration uncertainty better than 0.4 keV [96,98]. To obtain a higher precision *Q*-value we used the FSU-PPT to measure the masses of

both ^{130}Te (parent) and ^{130}Xe (daughter).

3.1.1.2 Neutrinoless Double Electron Capture

In addition to *neutrinoless* double beta decay, information concerning the nature of neutrinos could be obtained from the related *neutrinoless* processes of double positron emission, positron emission and electron capture, or double electron capture [99]. In general, these processes are strongly disfavored due to reduced decay energy and hence available phase space [100,101]. However, there are conditions under which neutrinoless double electron capture, 0νεε, can compete with the more popular 0νββ (see below).

Neutrinoless double electron capture is the process in which two atomic electrons are captured by two protons and become two neutrons (without emitting two electron neutrinos). Stated in another way, a nucleus with *Z* protons and mass number *A* is transformed into a nucleus with *Z-2* protons and remains with mass number *A*:

$$(Z, A) \rightarrow (Z-2, A)^{*HH'} \rightarrow (Z-2, A) + decay \quad radiation \qquad [3.4]$$

where the symbols H and H' identify the holes in the daughter atom, the levels from which the electrons were captured [102]. The daughter atom is unstable and can decay emitting γ-rays, X-rays, Auger electrons, etc. In particular, the double electron capture can be to an excited state.

As stated above, generally the rate of 0νεε is too low for detection of this process to be considered as a viable experimental option. However, rate enhancements of ~10^5-10^6 are possible if there is a fortuitous near degeneracy of the energies of the parent and excited daughter atom of much less than 1 keV [101,103]. Possible situations such as this have been discussed recently in ^{112}Sn [102] and ^{74}Se [100]. Their related mass differences needed to be measured precisely to determine if the rates of 0νεε are greatly enhanced for these atoms, as the rates are affected by several orders of magnitude when there is just a few keV in the uncertainty in the *Q*-value [103]. When this problem was initially brought to the attention of our group, the 0νεε *Q*-value of ^{112}Sn had already been measured by the University of Jyväskylä Penning trap, JYFLTRAP, to a sufficient precision [104] to rule out a useful degeneracy in that atom.

Double electron capture in the ^{74}Se-^{74}Ge system is shown in Figure 3.3. Two possible decays are expected from the excited daughter atom: either a two gamma cascade of energies 608.355(9) and 595.850(6) keV or one gamma quantum of energy 1204.205(7) keV [101,105].

Detection of this cascade originating from a sample of ^{74}Se would be the signature of the 0νεε and confirm that neutrinos are Majorana particles [100].

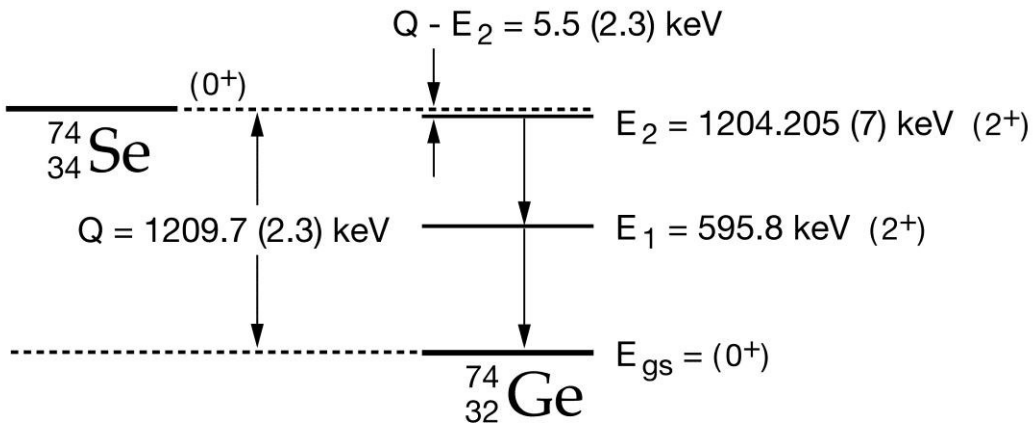

Figure 3.3 Level scheme for the double-electron capture decay of ^{74}Se to the second excited (2^+) state of ^{74}Ge. The ^{74}Se-^{74}Ge *Q*-value is from [90], and the energies of the first two excited levels of ^{74}Ge are from [106].

Before the FSU-PPT measurement, the best 0νεε *Q*-value for ^{74}Se was 1209.7(2.3) keV [90]. The initial and final states are closest in energy (leading to the largest enhancement rate) for the capture of two electrons from the L shell. For the case of (L_2L_3) capture, which would be necessary for decay to the 2^+ state conserving spin and parity without other radiation emitted [46], the necessary binding energy is 2.465(3) keV [107], making the difference between the *Q*-value and resulting energy of the daughter atom 3.0(2.3) keV, which does not necessarily rule out the hoped for degeneracy (see Figure 3.3). Therefore, we set out to measure the 0νεε *Q*-value of ^{74}Se.

3.1.2 ^{130}Xe/^{130}Te Data and Analysis

Since the analysis for this data set was accomplished by Matt, I will only summarize it in favor of devoting more details to the selenium and germanium data in the next section (which I analysed). The obvious method of measuring a *Q*-value would be to directly measure the ratio, and hence the mass difference, of the parent and daughter atoms of the decay. However, the single-ion make-kill-remake technique is problematic when using a difficult to make ion such as $^{130}Te^{3+}$, and would yield low statistics (one such run was attempted, however, see Table 3.2).

Using the two-ion swapping technique would generate better statistics and ensure the trap conditions (and systematic effects) would be nearly identical for the two ions. However, the closeness of the masses of ^{130}Te and ^{130}Xe make this proposed method difficult. Since the masses are only separated by a fractional difference of ~2 x 10^{-5}, the ions cannot be manipulated independently. Indeed, this scheme involving directly measuring the ratio $^{130}Xe^{3+}/^{130}Te^{3+}$ was attempted, but it was observed that while exciting the ion with the radial drive at the center of the trap, the ion in the parking orbit was also observed to be resonantly excited. Because this leads to additional, complicated systematic mode frequency shifts that we did not investigate, this $^{130}Xe^{3+}/^{130}Te^{3+}$ ratio measurement (along with the single-ion measurement) were used only as a further test of the *Q*-value.

It was decided instead to measure the ratio of the parent and daughter atoms' masses relative to the mass of a reference ion. The mass of ^{129}Xe had previously been precisely measured by the FSU-PPT trap using the single ion make-kill-and-remake technique [70] and was chosen as the reference mass. Since the mass of ^{129}Xe is known to 0.1 ppb, this route had the added benefit of allowing the precise measurement of the masses of ^{130}Xe and ^{130}Te. Additionally, the ratio $^{130}Xe^{3+}/^{132}Xe^{3+}$ was measured to test for systematics.

The ratios measured to obtain the *Q*-value were $^{130}Xe^{3+}/^{129}Xe^{3+}$ and $^{130}Te^{3+}/^{129}Xe^{3+}$. The xenon ions were made by letting gas into the top of the trap, and then ionizing the gas using electron-impact ionization in the usual way (see Section 2.2.1). The tellurium ions were made using the vapor loader (see Section 2.2.3) by heating a few mg of enriched tellurium powder. Once the ions were made, runs were conducted where the inner ion's cyclotron orbit was approximately 60 μm and the parking orbit of the outer ion was approximately 2 mm.

As a verification that trap conditions did not vary between the measurement of the ratio of $^{130}Xe^{3+}/^{129}Xe^{3+}$ and $^{130}Te^{3+}/^{129}Xe^{3+}$, three runs measuring the ratio of $^{129}Xe^{3+}/^{132}Xe^{3+}$ were completed (the mass of ^{132}Xe also being well-known [70]) before and after the *Q*-value ratio measurements to ensure that any systematic shifts between the mass-129 and mass-130 cyclotron frequencies, which may affect the measurements, do not change between the measurements of ^{130}Te and ^{130}Xe, and so have negligible effect on the ^{130}Te-^{130}Xe mass difference . The weighted mean of the three runs before and after the *Q*-value measurement agreed within their weighted errors.

Table 3.2 Average cyclotron frequency (*i.e.* inverse mass) ratios and systematic corrections for the $^{130}Xe/^{130}Te$ data. *N* is the number of runs included in the average. Δ_{trap}, $\Delta_{i\text{-}i}$, and Δ_{fz} are the estimated systematic corrections in parts-per-trillion (ppt), with estimated uncertainty in parentheses, due to trap field imperfections, ion-ion interaction, and shifts in f_z due to ion-detector interaction and differential voltage drift, respectively. σ_{syst} is the total systematic error and σ_{stat} is the statistical error (in ppt) for each average ratio. <*R*> is the average ratio after applying systematic corrections, with statistical and systematic uncertainties combined in quadrature, in parentheses. The three entries for $^{130}Te^{3+}/^{130}Xe^{3+}$ correspond to results obtained with a single ion in the trap, with two ions in the trap, and from the ratio of the $^{130}Te^{3+}/^{129}Xe^{3+}$ and $^{130}Xe^{3+}/^{129}Xe^{3+}$ ratios, respectively.

Ion pair	*N*	Δ_{trap}	$\Delta_{i\text{-}i}$	Δ_{fz}	σ_{syst}	σ_{stat}	<*R*>
$^{130}Xe^{3+}/^{129}Xe^{3+}$	5	1(18)	1(11)	-18(31)	38	73	0.992 311 669 329(82)
$^{130}Te^{3+}/^{129}Xe^{3+}$	3	-5(17)	1(11)	-11(30)	36	75	0.992 290 942 332(83)
$^{132}Xe^{3+}/^{130}Xe^{3+}$	5	-5(34)	2(22)	-35(34)	53	83	0.984 832 390 737(98)
$^{132}Xe^{3+}/^{129}Xe^{3+}$	6	-8(45)	2(33)	-22(38)	68	65	0.977 260 673 493(94)
$^{130}Te^{3+}/^{130}Xe^{3+}$ (1 ion)	1	-7(26)	0(0)	34(15)	30	252	0.999 979 112 310(254)
$^{130}Te^{3+}/^{130}Xe^{3+}$ (2 ion)	1	2(6)	0(60)	0(16)	62	182	0.999 979 112 415(192)
[$^{130}Te^{3+}/^{130}Xe^{3+}$] ($^{129}Xe^{3+}$)		-6(11)	0(2)	7(13)	17	97	0.999 979 112 412(98)

Table 3.2 summarizes all the ratios obtained from these runs with their systematic and statistical errors. Notice the three methods of determining the $^{130}Te^{3+}/^{130}Xe^{3+}$ ratio agree. Additionally, the ratio obtained from the $^{132}Xe^{3+}/^{129}Xe^{3+}$ measurement in Table 3.2 agrees with the ratio obtained previously using the FSU-PPT in Reference [70] of 0.977 260 673 508(95).

While the statistical uncertainty dominates the error, the largest systematic shifts (and uncertainties) were due to the shifts to the axial frequency due to the $C_4 a_z^2$ shift (see Section 2.3.1) and the f_z drift shift (see Section 2.3.7). In addition to the ratios measured under optimum conditions, several tests of systematic effects were performed by measuring the ratio of $^{129}Xe^{3+}/^{132}Xe^{3+}$ while varying the parking radius and guard ring voltage. Being a worse mass-doublet than either $^{130}Xe^{3+}/^{129}Xe^{3+}$ or $^{130}Te^{3+}/^{129}Xe^{3+}$, this ratio is a stringent test of the mass dependent systematic effects. While these measurements were used in the analysis of the systematic errors, they do not appear in Table 3.2. The mass difference equations corresponding to the ratios in Table 3.2 are given in Table 3.3.

Table 3.3 Mass difference equations corresponding to the ratios given in Table 3.2. The statistical, systematic and total errors are shown in parentheses.

Ion pair	Mass Difference	Result (u)
$^{130}Xe^{3+}/^{129}Xe^{3+}$	$^{130}Xe–^{129}Xe$	0.998 728 483(10)(5)(12)
$^{130}Te^{3+}/^{129}Xe^{3+}$	$^{130}Te–^{129}Xe$	1.001 441 885(10)(5)(12)
$^{132}Xe^{3+}/^{130}Xe^{3+}$	$^{132}Xe–^{130}Xe$	2.000 645 724(11)(7)(14)
$^{132}Xe^{3+}/^{129}Xe^{3+}$	$^{132}Xe–^{129}Xe$	2.999 374 229(9)(9)(13)
$^{130}Te^{3+}/^{130}Xe^{3+}$ (1 ion)	$^{130}Te–^{130}Xe$	0.002 713 416(33)(4)(34)
$^{130}Te^{3+}/^{130}Xe^{3+}$ (2 ion)	$^{130}Te–^{130}Xe$	0.002 713 402(24)(9)(26)
$[^{130}Te^{3+}/^{130}Xe^{3+}]$ $(^{129}Xe^{3+})$	$^{130}Te–^{130}Xe$	0.002 713 402(13)(3)(14)

We choose to use the mass difference of the last line of Table 3.3 to give the Q-value and leave the other two results as redundant checks. Expressing it in energy units, $Q_{\beta\beta}(^{130}Te)$ = 2527.518(13) keV. From the mass differences, the masses can also be obtained, and are listed in Table 3.4.

Table 3.4 Atomic masses of ^{130}Xe and ^{130}Te obtained from the different ratios, and their weighted averages, compared with previous values.

Atom	Source	Atomic Mass (u)
^{130}Xe	$^{130}Xe^{3+}/^{129}Xe^{3+}$	129.903 509 342(16)
	$^{132}Xe^{3+}/^{130}Xe^{3+}$	129.903 509 362(17)
	Average	129.903 509 351(15)
	AME [90]	129.903 508 0(8)
^{130}Te	$^{130}Te^{3+}/^{129}Xe^{3+}$	129.906 222 744(16)
	AME [90]	129.906 224 4(21)

3.1.3 ^{76,74}Ge/^{76,74}Se Data and Analysis

Data. The measurement of the *Q*-values and masses of ^{76,74}Ge/^{76,74}Se took over three months to complete. The mass-76 ratios were measured first, followed by the mass-74 ratios. For the two ion swapping technique, it is important to use ions of the same charge state. Doubly charged ions were chosen because they are within the mass range of our detector, and are easier to make than triply charged ions. The mass of ^{84}Kr is the closest precisely known mass [70] to mass-74 and mass-76, so the ion $^{84}Kr^{2+}$ was chosen as the reference.

To ensure that there were no drastic changes in the trap environment during the measurement, the ratio $^{76}Se^{2+}/^{84}Kr^{2+}$ was measured before and after the $^{76}Ge^{2+}/^{84}Kr^{2+}$ measurement. The weighted average of the $^{76}Se^{2+}/^{84}Kr^{2+}$ ratios from runs measured before and the weighted average from runs measured after the $^{76}Ge^{2+}/^{84}Kr^{2+}$ ratio measurements agreed with each other within their statistical uncertainties. Similarly, the ^{74}Se and ^{74}Ge measurements were interleaved and the like measurements also agreed within error bars as demonstrated in Figure 3.4.

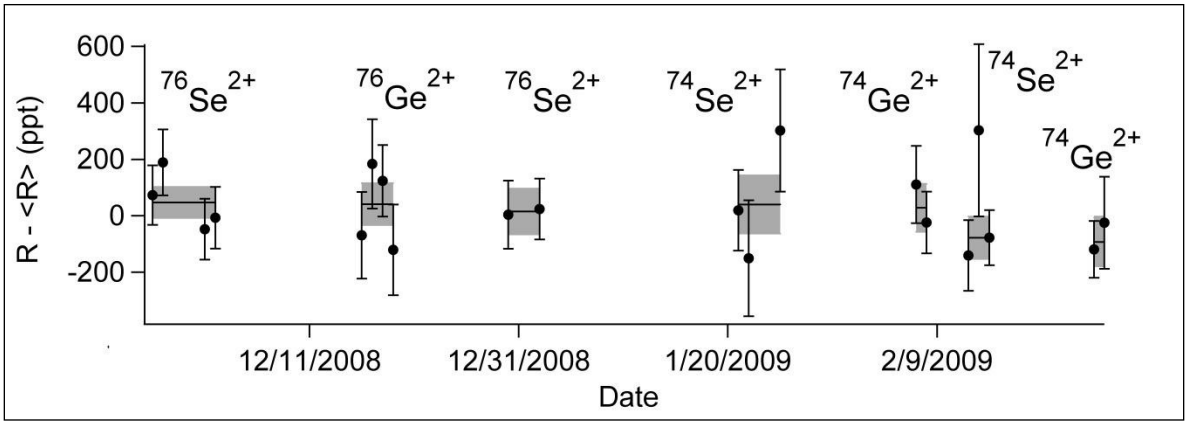

Figure 3.4 Cyclotron frequency ratios relative to $^{84}Kr^{2+}$, uncorrected for systematic errors, obtained from each run. The horizontal bands correspond to the averages of each group of data. The reference ratios <*R*> are the final, corrected average ratios, as given in Table 3.6.

Analysis. The larger difference in *m/q* between the two ions trapped simultaneously requires careful consideration. In general, the systematic shifts and errors are larger than in experiments of the past [66]. For example, while in the ^{130}Te/Xe measurements the statistical errors were the limiting factor, here the systematic uncertainties dominate the error in the masses.

However, these systematic shifts cancel in the ratio of the ratio obtained for the *Q*-value and only run-to-run variations remain in the systematic uncertainty for the *Q*-value. These ratios along with a break-down of the systematic shifts are given in Table 3.6.

For the mass 76 ratio measurements, a *CDT* of 22 ms was used for both the $^{84}Kr^{2+}$ and $^{76}Ge/Se^{2+}$ ions (see Section 2.4.2), corresponding to ρ_{ci} of approximately 107 μm and 121 μm, respectively. Once these measurements had begun, it was apparent that smaller radii could have been used, but it was decided to continue with the measurements instead of introducing any variations into the systematic effects of the *Q*-value. However, a smaller *CDT* of 15 ms was used for the mass 74 ratio measurements, corresponding to cyclotron radii of 73 μm and 85 μm for the $^{84}Kr^{2+}$ and $^{74}Ge/Se^{2+}$ ions, respectively. In the order $^{84}Kr^{2+}$ and $^{76}Ge/Se^{2+}$, $^{74}Ge/Se^{2+}$, the parking radii were approximately 2.3, 2.5 and 2.6 mm. While the mass 74 measurement had the advantage of smaller ρ_{ci}, it had the disadvantage of occurring after the "magnetic field event" described in Section 2.4.1.

As described in Section 2.4.2, the estimations in the above paragraph rely on the measurement of ρ_c^{cal} which depends on *m/q*. Also described in that Section are the three different methods of measuring ρ_c^{cal} using $\rho_c^{cal}(m=28)$ as a reference. For this set of data, all measured ρ_c^{cal} values are summarized in Figure 3.5.

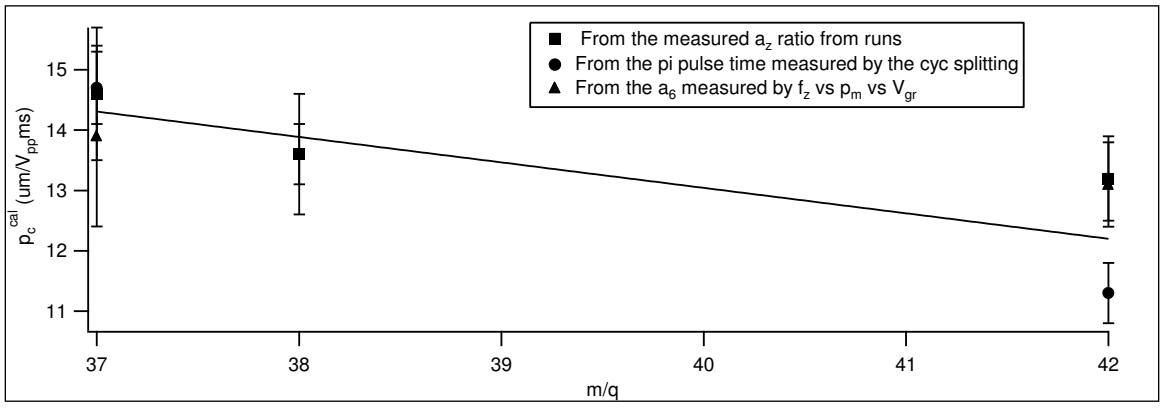

Figure 3.5 Measured ρ_c^{cal} values for *m/q* = 37, 38, 42 (see Section 2.4.2). The value of ρ_c^{cal} used for each ion was obtained from the straight line fit to the data.

The ρ_c^{cal} values used in the analysis to determine ρ_{ci}, ρ_{ck} and a_z are from the fit of the line to the data in Figure 3.5. The errors associated with these values are the fit error, error in the $\rho_c^{cal}(m=28)$ reference, and difference between the ρ_c^{cal} used from the furthest ρ_c^{cal} measurement combined in quadrature. The values used in the final analysis of this data set are given in Table 3.5.

Table 3. 5 ρ_c^{cal} values associated with each m/q.

m/q	ρ_c^{cal} (μm/V_{pp}ms)
37	14.2(8)
38	13.8(6)
42	12.2(1.1)

In addition to ρ_c^{cal}, another important mass-dependent parameter is V_{gr}^0 (see Section 2.4.3). Several f_z *vs* ρ_m *vs* V_{gr} measurements were taken, and the resulting V_{gr}^0 are plotted versus *m/q* in Figure 3.6.

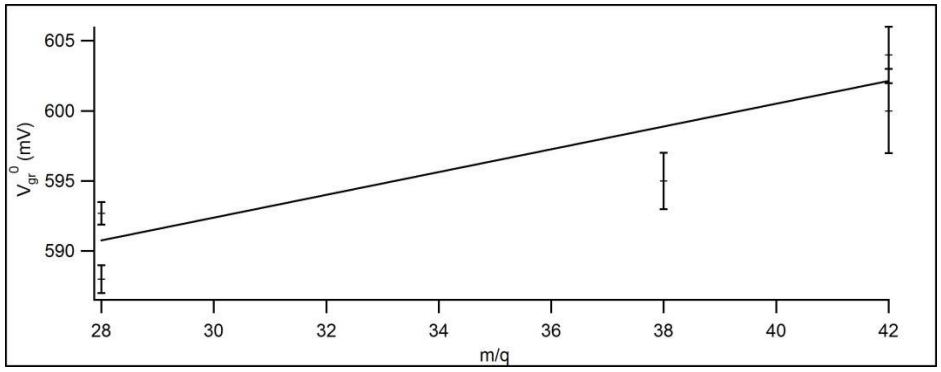

Figure 3.6 Values of V_{gr}^0 from f_z *vs* ρ_m *vs* V_{gr} measurements versus *m/q*.

From the fit to this line, it is clear that it is safe to use 600(7) mV for V_{gr}^0. Supporting evidence comes from several runs with $^{74}Ge^{2+}$, where V_{gr} was set to 580 and 620 mV. The ratios for these

runs were shifted in opposite directions by equal amounts. Using these values for ρ_c^{cal} and V_{gr}^{0}, along with the models described in Section 2.3, the systematic shifts and uncertainties in the ratio of the cyclotron frequencies may be determined and are listed in Table 3.6.

Table 3.6 Average cyclotron frequency (*i.e.* inverse mass) ratios and systematic shifts for the ^{74,76}Ge/^{74,76}Se data. *N* is the number of runs included in the average, Δ_{trap}, $\Delta_{i\text{-}i}$, and Δ_{fz} are the estimated systematic corrections in parts-per-trillion (ppt), with estimated uncertainty in parenthesis, due to trap field imperfections, ion-ion interactions, and shifts in f_z due to ion-detector interaction and differential voltage drift, respectively. σ_{sys} is the total systematic error and σ_{stat} is the statistical error (in ppt) for each average ratio. $\langle R \rangle$ is the average ratio after applying systematic corrections, with statistical and systematic uncertainties combined in quadrature. [$^{74}Ge^{2+}/^{74}Se^{2+}$] ($^{84}Kr^{2+}$), etc. for mass-76, denotes the ratio of the previous two ratios, with allowance for cancellation of common systematic errors.

Ion pair	*N*	Δ_{trap}	$\Delta_{i\text{-}i}$	Δ_{fz}	σ_{syst}	σ_{stat}	$\langle R \rangle$
$^{84}Kr^{2+}/^{74}Ge^{2+}$	4	26(126)	-7(20)	–50(58)	140	60	0.880 940 623 463(153)
$^{84}Kr^{2+}/^{74}Se^{2+}$	6	26(126)	-7(20)	–56(58)	140	61	0.880 956 094 495(153)
[$^{74}Ge^{2+}/^{74}Se^{2+}$] ($^{84}Kr^{2+}$)		0(42)	0(4)	5(5)	42	97	1.000 017 561 935(106)
$^{84}Kr^{2+}/^{76}Ge^{2+}$	4	85(187)	-13(39)	–31(42)	195	74	0.904 778 252 053(209)
$^{84}Kr^{2+}/^{76}Se^{2+}$	6	83(186)	-13(39)	–33(47)	196	45	0.904 752 164 530(201)
[$^{76}Ge^{2+}/^{76}Se^{2+}$] ($^{84}Kr^{2+}$)		2(40)	0(6)	1(20)	45	96	0.999 971 166 953(106)

The largest systematic shifts for the mass-76 measurement were the C_4z^2 and C_6z^4 trap imperfections shifts. Due to the increased magnetic field inhomogeneity for the mass-74 measurements (see Section 2.4.1), $B_2\rho_c^2$ was the largest shift, followed by the C_4z^2 shift. To confirm our model of the systematic effects of our trap, we measured the ratio of $^{84}Kr^{2+}/^{84}Kr^{3+}$. This is a stringent test of the charge-dependent and *m/q*-dependent ($\Delta m/q = 14$) systematic effects. As can be seen from Figure 3.7, the corrected ratios all correspond within error bars with the ratio calculated from the masses.

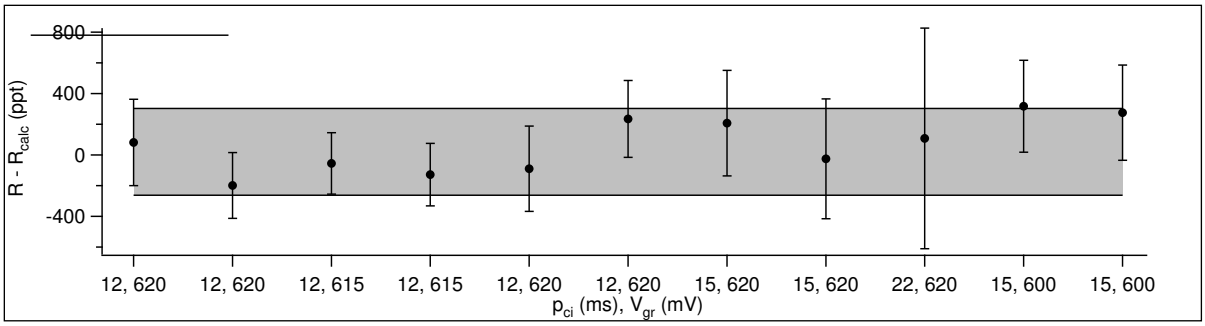

Figure 3.7 $^{84}Kr^{2+}/^{84}Kr^{3+}$ ratio measurements corrected for systematic effects. The error bars include the systematic and statistical errors combined in quadrature. The horizontal band corresponds to the weighted average and error bar including common systematic errors. Each point corresponds to one run taken with the ρ_{ci} and V_{gr} indicated on the x-axis. The y-axis is the ratio calculated from the best-known value of the mass of ^{84}Kr [70], the mass of the electron [91], and the ionization energies of the doubly and triply charged states of Kr [108], subtracted from the measured corrected ratio.

The mass differences obtained from the ratios in Table 3.6 combined with the mass of the electron [91], the mass of ^{84}Kr [70], and the ionization energies of the ions [108,109] are given in Table 3.7.

Table 3.7 Mass difference equations corresponding to the ratios given in Table 3.6. The statistical, systematic and total errors are shown in parenthesis.

Ion pair	Mass Difference	Result (u)
$^{74}Ge^{2+}/^{84}Kr^{2+}$	$^{84}Kr–^{74}Ge$	9.990 319 966 3(51)(117)(128)
$^{74}Se^{2+}/^{84}Kr^{2+}$	$^{84}Kr–^{74}Se$	9.989 021 793 4(51)(118)(128)
$[^{74}Se^{2+}/^{74}Ge^{2+}]$ $(^{84}Kr^{2+})$	$^{74}Ge–^{74}Se$	-0.001 298 172 9(74)(13)(75)
$^{76}Ge^{2+}/^{84}Kr^{2+}$	$^{84}Kr–^{76}Ge$	7.990 095 001 7(62)(164)(175)
$^{76}Se^{2+}/^{84}Kr^{2+}$	$^{84}Kr–^{76}Se$	7.992 284 023 8(38)(164)(169)
$[^{76}Se^{2+}/^{76}Ge^{2+}]$ $(^{84}Kr^{2+})$	$^{76}Ge–^{76}Se$	0.002 189 022 1(73)(34)(80)

From the mass differences the mass of $^{74,76}Se$ and $^{74,76}Ge$ may be obtained (see Table 3.8), as well as the *Q*-values. The *Q*-value for double β-decay of ^{76}Ge was found to be 2039.061(7) keV, and the *Q*-value for the double-electron capture of ^{74}Se was found to be 1209.240(7) keV.

Table 3.8 Atomic masses (in u) of ^{74,76}Ge and ^{74,76}Se.

Isotope	FSU-PPT Measurement
^{74}Ge	73.921 177 765(15)
^{74}Se	73.922 475 938(15)
^{76}Ge	75.921 402 729(19)
^{76}Se	75.919 213 707(19)

3.1.5 Discussion

The 0νββ *Q*-value of ^{130}Te was measured to be 2527.518(13) keV. This *Q*-value is two orders of magnitude more precise than the current AME 2003 value and is more than of sufficient precision for the CUORICINO experiment and the future CUORE experiment. Our result has recently been confirmed (within 1.5σ), but with a standard deviation a factor of 25 larger than our result, by the Canadian Penning Trap, (see Table 3.9) [110]. Our measurement of the $Q_{\beta\beta}$(^{76}Ge-^{76}Se) agrees and is a factor of seven more precise than the next-most precise Penning trap measurement [111]. The many measurements of this particular *Q*-value is a testament to its importance in the search for 0νββ [88,104,111]. The overall abundance of precision *Q*-value measurements in general underscores the prominence of the many ongoing 0νββ searches [46,68,87,88,104,110-113].

Table 3.9 The three $Q_{\beta\beta}$ decay values measured by the FSU-PPT compared to other recent mass spectrometer measurements. Note that for the ^{136}Xe-^{136}Ba *Q*-value, only the ^{136}Xe mass was measured by FSU and ISOLTRAP, and the ^{136}Ba mass was taken from the AME 2003. However, the Manitoba II spectrometer measured the mass difference directly.

$Q_{\beta\beta}$ (keV)	ISOLTRAP[113]	FSU[68,87,88]	CPT[110]	SMILETRAP[111]	JYFLTRAP[89]	Manitoba II[112]
^{76}Ge-^{76}Se		2039.061(7)		2039.006(50)	2039.04(16)	
^{130}Te-^{130}Xe		2527.518(13)	2527.01(32)			
^{136}Xe-^{136}Ba	2462.7(4.3)	2457.83(37)				2458.73(56)

The 0νεε *Q*-value of ^{74}Se was found to be 1209.240(7) keV. Allowing for the L_2L_3 electron binding energies [107], the energy difference between the second excited state of ^{74}Ge [106] and the 0νεε *Q*-value of ^{74}Se was found to be 2.570(10) keV. JYFLTRAP has measured

this value to be 2.50(5) keV. Both the FSU-PPT and the JYFLTRAP values are greater than the hoped-for value of a few eV, and no helpful resonant enhancement is expected.

3.2 "World's Smallest Beta Decay *Q*-value"

3.2.1 Motivation

As of the publication of the AME 2003, the energy difference listed between the ground state of ^{115}In and the first excited state of ^{115}Sn was 1.7(4.0) keV, see Figure 3.8. Since this uncertainty did not preclude the possibility that the energy difference was negative, it was not known whether a β-decay from ^{115}In($9/2^+$) →^{115}Sn($3/2^+$) was possible (whether the ground state of ^{115}In was higher or lower in energy than the first excited state of ^{115}Sn). Cattadori *et al.* were the first to discover the beta decay of ^{115}In($9/2^+$)→^{115}Sn($3/2^+$)[12]. They observed a line in their γ spectrum, located at 497.48(21) keV with a relative intensity of 1.18(31) x 10^{-4}% compared to the ^{115}In($9/2^+$) →^{115}Sn($1/2^+$) intensity (see Figure 3.8)[13], which they inferred must have followed the ^{115}In($9/2^+$)→^{115}Sn($3/2^+$) β-decay [114].

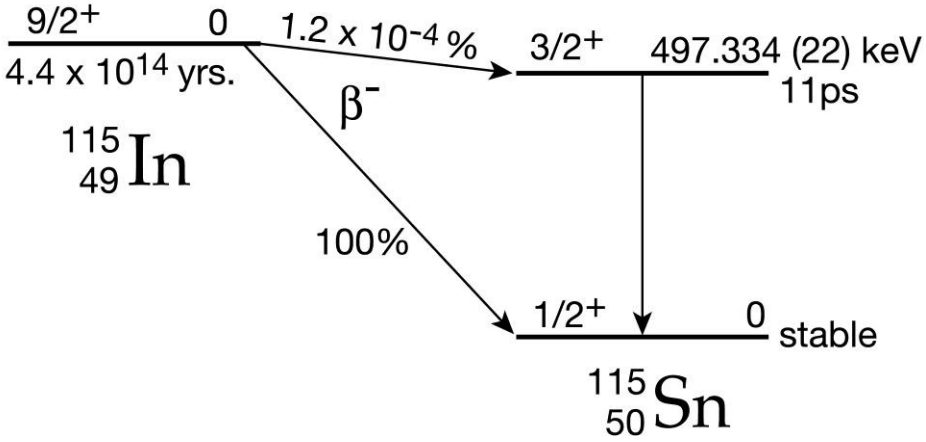

Figure 3.8 Level scheme for the beta-decay of the ground state of ^{115}In showing relevant half-lives and branching ratios.

[12] The purpose of the Cattadori *et al.* experiment was to investigate the γ spectrum of ^{115}In, which was being considered for possible use as a detector of solar neutrinos through the ^{115}In(ν_e,e^-)^{115}Sn* neutrino capture reaction.
[13] ^{115}In is unstable with a half-life of 4.41(25) x 10^{14} yrs [116] and almost always β-decays to the grounds state of ^{115}Sn (see Figure 3.8).

From their half-life measurement, they were able to deduce a range of possible *Q*-values from 0.12 to 2.85 keV, implying the possibility that $^{115}In(9/2^{+}) \rightarrow {}^{115}Sn(3/2^{+})$ is the smallest known β-decay *Q*-value[14]. This *Q*-value may be obtained more precisely from measuring the mass difference of ^{115}In and ^{115}Sn combined with an already precise gamma-ray measurement of the first excited level of ^{115}Sn, 497.334(22) keV [115].

3.2.2 $^{115}In/^{115}Sn$ Data and Analysis

The $^{115}In/^{115}Sn$ *Q*-value is the latest *Q*-value to be measured by the FSU-PPT. By the time this *Q*-value was measured, the techniques developed with other FSU-PPT *Q*-value measurements had almost become routine. The entire $^{115}In/^{115}Sn$ measurement took less than two weeks to accomplish. The ^{115}In and ^{115}Sn ions were made via the vapor loader (see Section 2.2.3) with natural indium (95.7% ^{115}In) and an enriched sample of tin (32.4% ^{115}Sn) loaded into a 1mm diameter niobium tube. The *Q*-value measurement consisted of four runs of the ratio $^{115}In^{3+}/^{129}Xe^{3+}$, followed by five runs of $^{115}In^{3+}/^{129}Xe^{3+}$, followed by four additional runs of $^{115}In^{3+}/^{129}Xe^{3+}$ (see Figure 3.9).

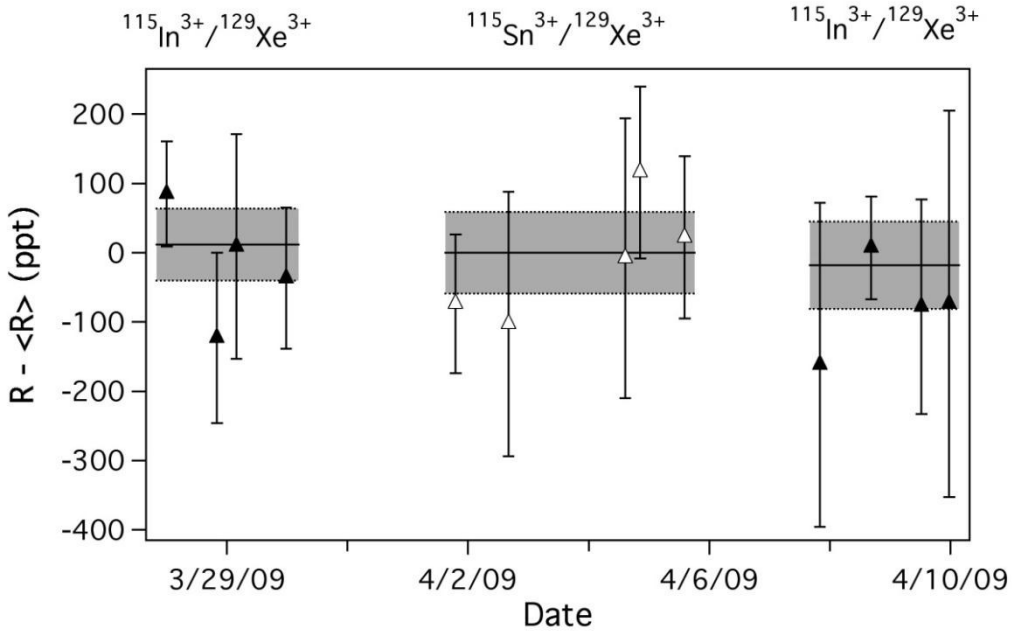

Figure 3.9 Cyclotron frequency ratios, uncorrected for systematic errors, obtained from each run. The horizontal lines and error bands correspond to the averages of each of the three sets of data.

[14] The smallest β-decay *Q*-value known at that time was that of ^{187}Re: 2.470(4) keV [117].

Like the Se and Ge measurements, the ratios measured here are not good mass doublets ($\Delta m/q \approx 4.7$) and so the systematic uncertainty is the largest contributor of error. For the ratio of the ratio for the Q-value, most systematic effects drop out, leaving the statistical error to dominate the uncertainty.

Table 3.10 Average cyclotron frequency (*i.e.* inverse mass) ratios and systematic corrections for the ^{115}In/^{115}Sn data. N is the number of runs included in the average. Δ_{trap}, $\Delta_{i\text{-}i}$, and Δ_{fz} are the estimated systematic corrections in parts-per-trillion (ppt), with estimated uncertainty in parentheses, due to trap field imperfections, ion-ion interaction, and shifts in f_z due to ion-detector interaction and differential voltage drift, respectively. σ_{syst} is the total systematic error and σ_{stat} is the statistical error (in ppt) for each average ratio. $\langle R \rangle$ is the average ratio after applying systematic corrections, with statistical and systematic uncertainties combined in quadrature, in parentheses. The entry for $^{115}In^{3+}/^{115}Sn^{3+}$ correspond to the ratio of the above two ratios, allowing for cancellation of common systematic errors.

Ion pair	N	Δ_{trap}	$\Delta_{i\text{-}i}$	Δ_{fz}	σ_{syst}	σ_{stat}	$\langle R \rangle$
$^{115}In^{3+}/^{129}Xe^{3+}$	8	-10(63)	10(18)	–11(32)	73	45	0.891 384 316 786(86)
$^{115}Sn^{3+}/^{129}Xe^{3+}$	5	-11(63)	11(19)	–28(39)	76	66	0.891 380 173 543(101)
$[^{115}Sn^{3+}/^{115}In^{3+}]$ $(^{129}Xe^{3+})$		-1(4)	1(1)	–17(7)	8	90	0.999 995 351 900(90)

Like the mass-74 ratios, the ^{115}In/^{115}Sn set of measurements occurred after the "magnetic field event," and therefore one of the biggest systematic shifts was the $B_2\rho_c^2$ shift. The $C_4a_z^2$shift was also a major contributor, as was the f_z drift shift (see Section 2.3). The mass difference equations obtained from the ratios in Table 3.10 are given in Table 3.11.

Table 3.11 Mass difference equations corresponding to the ratios given in Table 3.10. The statistical, systematic and total errors are shown in parentheses.

Ion pair	Mass Difference	Result (u)
$^{129}Xe^{3+}/^{115}In^{3+}$	^{129}Xe–^{115}In	14.000 902 084 5 (58)(94)(111)
$^{129}Xe^{3+}/^{115}Sn^{3+}$	^{129}Xe–^{115}Sn	14.001 436 161 3 (85)(98)(130)
$[^{115}In^{3+}/^{115}Sn^{3+}]$ $(^{129}Xe^{3+})$	^{115}In–^{115}Sn	0.000 534 076 8 (103)(9)(104)

From these mass differences, the atomic masses of ^{115}In and ^{115}Sn were obtained (see Table 3.12). The last row of Table 3.11 is the *Q*-value of the β-decay from the ground state of ^{115}In to the ground state of ^{115}Sn. Expressed in terms of energy, the *Q*-value for the ^{115}In($9/2^+$) $\rightarrow$^{115}Sn($1/2^+$) β-decay is 497.489(10) keV. Subtracting the energy difference between the first excited state and the ground state of ^{115}Sn, gives the Q- value for the ^{115}In($9/2^+$) $\rightarrow$^{115}Sn($3/2^+$) β-decay as 155(24) keV.

Table 3.12 Atomic masses (in u) of ^{115}In and ^{115}Sn compared with values in the AME2003 [11].

Isotope	AME2003	This Work
^{115}In	114.903 878(5)	114.903 878 774(16)
^{115}Sn	114.903 342(3)	114.903 344 697(17)

3.2.3 Discussion

This measurements confirms that the ^{115}In($9/2^+$)$\rightarrow$^{115}Sn($3/2^+$) β-decay has the smallest known β-decay *Q*-value, 155(24) eV. JYFLTRAP has also measured this *Q*-value with the result of 350(170) eV [118]. Additionally, γ-ray spectroscopy measurements carried out at the HADES underground laboratory determined the half-life of the decay, which was then used along with theoretical nuclear matrix element (NME) calculations to determine another *Q*-value of 57^{+19}_{-12} eV [118].

Table 3.13 Comparison of the determinations of the ^{115}In($9/2^+$)$\rightarrow$^{115}Sn($3/2^+$) β-decay *Q*-value. Where applicable, 497.334(22) keV has been assumed for the energy difference between the first excited state and ground state of ^{115}Sn.

Determination	*Q*-value (eV)
AME 2003 [90]	1700(4000)
Cattadori *et al.*[114]	120-2850
JYFLTRAP [118]	350(170)
Half-life + NME [118]	57^{+19}_{-12}
FSU-PPT [119]	155(24)

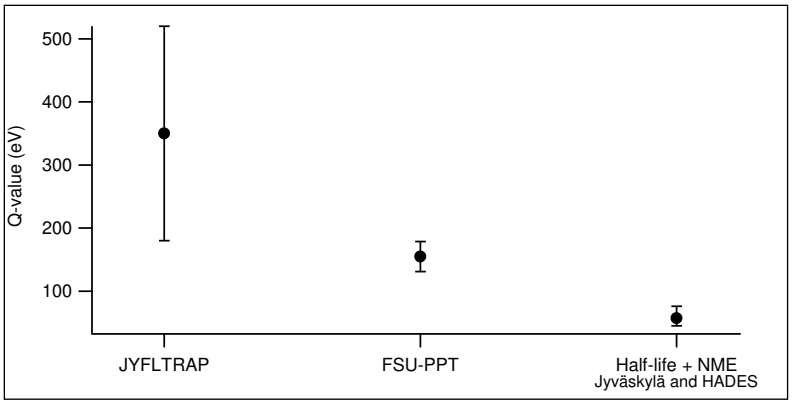

Figure 3.10 The three most precise β-decay *Q*-values of ^{115}In(9/2$^+$)→^{115}Sn(3/2$^+$) from two Penning trap measurements (JYFLTRAP [118] and FSU-PPT[119]) and a measurement of the half-life combined with nuclear matrix elements (NMEs) [118].

While the two Penning trap measurements almost agree within 1σ, the theoretical calculations using the half-life are several σ away from either value. The apparent error in the theoretical *Q*-value is described in [120] as possibly being due to the common neglect of atomic effects in the theory, which cannot be neglected for this uncommon case of ultra-low *Q*-values. Our precise *Q*-value, combined with measured decay rates provides a test case for the theory of very low *Q*-value beta-decay.

4. CYCLOTRON FREQUENCY MEASUREMENTS FOR ATOMIC PHYSICS AND PHYSICAL CHEMISTRY APPLICATIONS

4.1 Stable Alkali Masses

4.1.1 Motivation

The fine structure constant, α, sets the scale of the electromagnetic interaction, and so connects a wide range of fundamental and applied science. In particular, the level of agreement of the value for α obtained from different areas of physics can be used to test the consistency of current physics theories. The fine structure constant is defined through the relation [91]:

$$\alpha = \frac{1}{4\pi\varepsilon_0}\frac{e^2}{\hbar c} \qquad [4.1]$$

where ε_0 is the electric constant, e is the charge of the electron, $\hbar$ is $h/2\pi$ where h is Planck's constant and c is the speed of light. Note that the electric constant and the speed of light are both constants fixed by definition and therefore contain no error.

The most accurate method to date of determining the fine structure constant is through the comparison of theory and measurement of the g-factor of the electron. Following the seminal developments in single particle Penning trap physics, a measurement of the electron's g-factor with a precision of 20 ppb was achieved at the University of Washington [27]. The precision has since been improved to the 0.37ppb level by the Harvard group [28]. The g-factor of the electron may be calculated as a sum of a power series in α using Quantum Electrodynamics (QED) and taking into account small terms associated with short-distance physics [121,122]:

$$\frac{g}{2} = 1 + C_2\left(\frac{\alpha}{\pi}\right) + C_4\left(\frac{\alpha}{\pi}\right)^2 + C_6\left(\frac{\alpha}{\pi}\right)^3 + C_8\left(\frac{\alpha}{\pi}\right)^4 + \ldots + a_{\mu l} + a_{hadronic} + a_{weak} \qquad [4.2]$$

Hence, using this equation, electron g-factor measurements yield values for the fine structure constant. However, if an independent, precise value for α is available, a measurement of the magnetic moment of the electron can then be used to test the above equation and therefore test QED. As a prototype field theory, QED is already one of the most precisely tested theories and is of central importance to modern physics.

Currently, the second most precise method for the determination of the fine structure constant is obtained from photon recoil experiments with alkali atoms. These experiments measure the recoil velocity of an atom after it has absorbed an optical photon and yield values of h/m_{alkali}. The fine structure constant is then obtained using the equation:

$$\alpha^2 = \left(\frac{2R_\infty}{c}\right)\left(\frac{m_{alkali}}{m_e}\right)\left(\frac{h}{m_{alkali}}\right) \qquad [4.3]$$

where R_∞ is the Rydberg constant [123], m_e is the mass of the electron [124], and m_{alkali} is the mass of the alkali atom. Compared to the g-factor method, this approach only depends on QED calculations in the corrections to the energy levels of hydrogen used to obtain R_∞ [123]. At this time, the photon recoil velocities of ^{133}Cs and ^{87}Rb have been measured using atom interferometry [125,126]. In addition to the g-factor and photon recoil measurements, a third competitive determination of the fine structure constant may be derived from the fine structure of helium and helium-like ions [127].

Table 4.1 Determinations of the fine structure constant.

Measurement	α^{-1}	Fractional Error
Electron g-factor, Harvard [28]	137.035 999 084(51)	0.37ppb
^{87}Rb photon recoil [126]	137.035 999 45(62)	4.5ppb
^{133}Cs photon recoil [125]	137.036 000 0(11)	8.0ppb
Electron g-factor, University of Washington [27]	137.035 990 0(27)	20ppb
Helium fine structure [127]	137.036 001 1(42)	31ppb

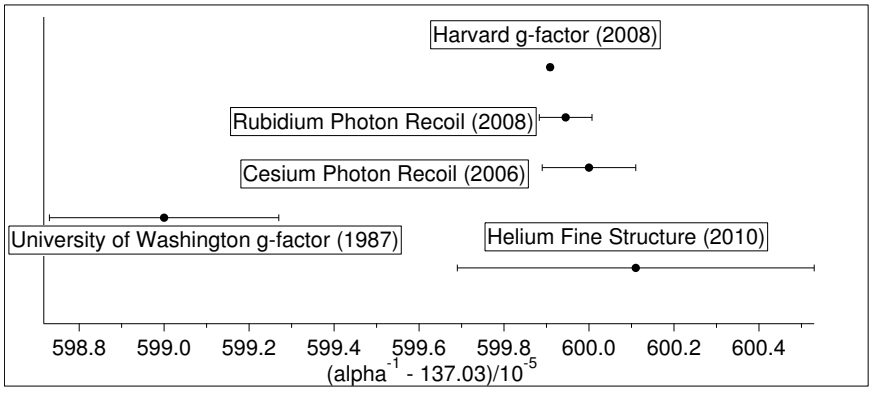

Figure 4.1 Determinations of the fine structure constant.

Another generation of photon recoil measurements is in development [128] with the aim of yielding precision competitive to that of the electron g-factor experiment. Eventually, these experiments may approach the limit of precision of the particular mass of the alkali. Although no competitively precise results for h/m_{alkali} based on the other stable alkalis have yet been reported, we note that all these species have been subjects of numerous investigations with ultra-cold atoms, and have now been Bose-Einstein condensed (or, for ^{6}Li, Fermi-condensed). Since the lighter alkalis have the advantage of higher photon-recoil velocities, h/m_{alkali} measurements may be expected in the future.

Additional motivations for our measurements of the atomic masses of the alkalis are provided by nuclear physics. All of the alkalis, because of their low ionization energies [129], are both easy to produce and resistant to charge exchange with background gas. This makes them convenient reference ions for the many mass spectrometers, already commissioned or under development, that use gas stopping of short-lived radioactive species produced in nuclear reactions (see Section 1.2). In the case of lithium, there is particular motivation due to discrepancies between masses in the literature: a precision Penning trap mass measurement of ^{6}Li [130] is in disagreement with masses obtained via two different Penning traps with time-of-flight detection [49,52]. Another mass measurement, utilizing distinct techniques, would be useful in verifying the mass. The mass of ^{6}Li is also important to calculations of the mass-shift contribution to the isotope shift as determined using laser spectroscopy [131]. These are needed to correct measured isotope shifts used to determine changes in nuclear charge-radii of the stable and also exotic "halo-nucleus" isotopes. Additionally, a more precise mass of ^{6}Li (along with the mass of the neutron and ^{7}Li) can determine the ^{6}Li(n,γ)^{7}Li Q-value, serving as a check of thermal neutron capture experiments [132,133].

Although the masses of the rubidium, cesium and sodium isotopes have already been measured to ≤ 0.2 ppb at MIT, it is important to check these values due to various problems with their measurements as described in ref. [65]. Although the same Penning trap was used for the measurements described in this paper and the MIT measurements, there were many differences in techniques, reference ions and systematic effects (see explanation below). A comparison of a FSU-PPT measurement of these alkalis with the MIT masses also serves as a test for our previous measurements of the reference ions ^{84,86}Kr and ^{129,132}Xe.

4.1.2 Experimental Details

As previously discussed in Section 1.3.3, the analysis of most of this data (with the exception of Li) was accomplished by Matt Redshaw, however I was mostly responsible for the data taking (except for Na). Therefore, I will describe the experimental details and summarize the analysis. This set of data is simply enormous. In total[15], there were 104 runs, each lasting 6-15 hours. The order of the measurements was ^{85,87}Rb, ^{39,41}K, ^{133}Cs, ^{23}Na and ^{6}Li.

^{85,87}Rb, ^{39,41}K, and ^{133}Cs were measured in the summer of 2008, and the masses of ^{23}Na and ^{6}Li were measured in the summer of 2009. Between these sets of measurements, many other mass measurements were obtained and the trap conditions had changed. The biggest event that occurred in the interim was the decrease in the magnetic field (see Section 2.3.2) in January 2009.

The alkali mass measurements were the first in which the vapor loader was used (see Section 2.2.3) at FSU. During this set of data, the alignment of the vapor loader was tested. The vapor loader sits on a converted optics mount. By turning the screws to adjust the mount, thereby adjusting the vapor loader's line-of-sight with the small hole in the upper endcap, and attempting to make an ion, the "best" alignment was found. With the exception of ^{6}Li, for which a home-made niobium dispenser containing isotopically enriched (>90%) ^{6}Li was used, the alkali vapors were produced by electrically heating commercial alkali dispensers from SAES [134], with natural isotopic abundances (^{23}Na 100%, ^{39}K 93.3%, ^{41}K 6.7%, ^{85}Rb 72%, ^{87}Rb 28%, ^{133}Cs 100%).

All the reference ions were made from gasses. Although this is not necessary, usually making from a gas is easier than making from the vapor loader. Additionally, the current vapor loader is set up to allow only one element at a time to be used (see Section 2.3.2). As mentioned above, there are several differences in the measurements described in this dissertation and the MIT alkali mass paper [65]. The first major difference between this measurement and the MIT measurement was the use of different sets of reference masses, see Table 4.2.

[15] Including runs which were not used in the determination of the final masses, but were used as checks of systematics.

Table 4.2 Comparison of FSU and MIT reference ions.

Alkali Ion	MIT Reference	FSU Reference
$^{6}Li_2^+$	N/A	$^{12}C^+$
$^{23}Na^+$	$^{12}C^+$, $^{12}C_2^+$	$^{20}Ne^+$, $^{12}C_2^+$
$^{39}K^+$	N/A	$^{40}Ar^+$
$^{41}K^+$	N/A	$^{40}Ar^+$, $^{40}ArH^+$
$^{85}Rb^{3+}$	N/A	$^{86}Kr^{3+}$
$^{85}Rb^{2+}$	$^{12}C_3H_6^+$, $^{12}C_3H_7^+$	$^{86}Kr^{2+}$, $^{84}Kr^{2+}$
$^{87}Rb^{2+}$	$^{12}C_3H_7^+$, $^{12}C_3H_8^+$	$^{86}Kr^{2+}$
$^{133}Cs^{2+}$	$^{12}C_5H_6^+$	N/A
$^{133}Cs^{3+}$	$^{12}CO_2^+$	$^{132}Xe^{3+}$, $^{132}Xe^{3+}$

The MIT measurements compared the cyclotron frequencies of multiply charged alkali ions and singly charged reference ions. Given the various asymmetries in this procedure, and because following similar procedures when measuring isotopes of krypton and xenon we encountered various systematic errors not discussed in [65], we compared ions only of the same charge state. The other difference with respect to the reference ions was that we chose not to use hydrocarbons due to possible "polarizability shifts" (see Chapter 5) to the cyclotron frequency for these ions [135]. Instead, we used our own previously measured masses of $^{84,86}Kr$ and $^{129,132}Xe$ as reference masses.

The second major difference is that the MIT data was taken with a single ion in the trap at a time, while our data was taken with two simultaneously trapped ions using our swapping technique (see Section 2.2.5). The laborious technique used by MIT to measure the alkali masses involved making and isolating a single ion of the desired species in the trap, measuring its cyclotron frequency, then "killing" it by adjusting the trap voltage such that the ion strikes an endcap. This process of making, isolating, measuring cyclotron frequency and "killing" was then repeated with the reference ion. The entire process would be repeated several times, making this technique demanding in the sense that an operator is needed for the duration of the entire measurement (~12 hours) to keep making the ions.

^{85,87}Rb and ^{133}Cs: The measurements involving ^{85,87}Rb and ^{133}Cs used multi-charged ions, which have two main advantages: it increases the signal size for a given axial amplitude and also the cyclotron frequency, both of which improve statistical precision. Additionally, smaller mode amplitudes may be used, reducing systematic shifts Δ_{ii} and Δ_{trap}, which depend on a_z and ρ_c. Further, the contribution of shifts to f_c due to shifts to f_z goes as $(f_z/f_c)^2$ and is hence reduced for increased f_c.

Because these measurements were at higher m/q, and required a higher trap voltage than is provided by our V-box, we increased its output by placing some lithium batteries (in a carefully temperature controlled housing) in series. However, when the batteries were being installed, they were accidentally shorted, and this caused a drift in the voltages of the trap during the measurements of rubidium. Therefore, the largest systematic shift for ^{85,87}Rb was a shift due to a differential voltage drift (see Section 2.3.7). To test that the correction used for the differential voltage shift was correct, the voltage channels associated with each channel were switched, and data was taken. The data with the ion voltage channels switched did indeed result in a shift equal, but in the opposite direction as when the ion voltage channels were not switched.

The second largest sources of systematic error were the C_4z^2 and C_6z^4 shifts to the axial frequency. For ^{133}Cs, the largest systematic shifts were due to C_4z^2 and the differential voltage drift. For the $^{133}Cs^{3+}/^{132}Xe^{3+}$ ratio, these shifts were small, and totaled to less than a part in 10^{-11}. The shifts for the ratio $^{133}Cs^{3+}/^{129}Xe^{3+}$ were larger due to the greater mass difference ($\Delta m/q$ = 1.33 vs. $\Delta m/q$ = 0.33).

^{39,41}K: For ^{39,41}K we used the reference ^{40}Ar. We also investigated systematic shifts to the ratio for the more severe non-mass-doublet ratios $^{12}C^{16}O_2^+/^{40}Ar^+$ and $^{40}Ar^+/^{18}O_2^+$. Within these data sets, we varied several experimental parameters and found good agreement for Δ_{trap} shifts, but found that the predicted Δ_{ii} shifts were too small by a factor of 3(1). Nevertheless, for both ratios we obtained agreement with the ratio determined using the masses in ref. [65] to within the combined statistical and systematic uncertainties. For the ratios $^{40}Ar^+/^{39}K^+$ and $^{41}K^+/^{40}Ar^+$ we increased the uncertainty in Δ_{ii} to 3 x Δ_{ii}. Even then, the uncertainty in Δ_{ii} contributed little to the total systematic error because of the larger Δ_{trap} shifts and uncertainties. These shifts are due to axial amplitude imbalance between the two ions and a non-optimal setting of the guard ring, so that C_4 was not close to zero.

We also performed one data run each for the ratios $^{40}ArH^+/^{40}Ar^+$ and $^{41}K^+/^{40}ArH^+$. On two occasions a $^{40}ArH^+$ was made serendipitously from a single $^{40}Ar^+$ ion that was already confined in the trap, presumably via collisions with background hydrogen gas via the interaction $Ar^+ + H_2 \rightarrow ArH^+ + H$. We observed that a $^{40}Ar^+$ disappeared from the trap and a $^{40}ArH^+$ had appeared.

^{23}Na: For $m/q = 23$ there is no convenient mass-doublet to use as a reference. Instead, as in ref. [65], we measured the ratio $^{12}C_2^+/^{23}Na^+$. This larger difference in m/q of the reference ion and the alkali ion results in larger systematic shifts due to trap imperfections and ion-ion interactions. We carefully investigated these systematic shifts by taking a series of data runs where we systematically varied the parking radius of the outer ion and the cyclotron amplitude (and hence axial amplitude) of the inner ion used in the PNP measurement. The data were well described by the models of ref. [67,79]. However for determining the final ratio, we used only data taken under optimal conditions, with the smallest inner cyclotron radius ρ_{ci} (~100 μm) and the largest practical parking radius ρ_{ck} (~1.6 – 1.7 mm). We also measured the ratio $^{23}Na^+/^{20}Ne^+$ and took data where we systematically varied ρ_{ci} and ρ_{ck}. For this ion pair, shifts to the cyclotron frequency ratio were as large as ~2 x 10^{-9}. However, the data were well described by the Δ_{ii} and Δ_{trap} model. The mass of ^{23}Na obtained from the ratio $^{23}Na^+/^{20}Ne^+$ differed from that of $^{12}C_2^+/^{23}Na^+$ by 3.1(6.2) x 10^{-10}, where the uncertainty is dominated by systematic uncertainty. Hence, we used only the $^{12}C_2^+/^{23}Na^+$ data to obtain the final value for mass of ^{23}Na.

^{6}Li: The measurements on ^{6}Li required extending our techniques, which we have previously implemented in the mass range $m/q = 17 – 45$, to significantly lower m/q. The main challenge in working with light, singly-charged ions is that, for a given axial amplitude, the energy in the harmonic axial mode decreases with mass. Larger axial amplitudes are required to detect the ion, which gives rise to larger systematic shifts. In addition, for fixed f_z (which in our case is fixed by the resonant frequency detector of our detector) lower m/q ions require a lower trapping potential, increasing sensitivity to stability of the ring voltage. Furthermore, the magnetron frequency is also lower. This results in a magnetron-axial coupling frequency: $\omega_{mc} = \omega_z + \omega_m$, that is close to ω_z, making it difficult to properly eliminate any magnetron motion.

Rather than work with the lithium monomer at smaller m/q, we worked with the dimer, and measured the mass-doublet ratio $^{6}Li_2^+/^{12}C^+$. Producing and isolating a single $^{6}Li_2^+$ was

challenging due to the ~1% dimer population in the lithium vapor, and the ~10% dimer ion ionization fragment. Nevertheless, we were able to isolate single $^{6}Li_2^+$ ions. However, we failed to make a single $^{7}Li_2^+$ ion due to an overwhelming signal from $^{14}N^+$ ions made from background gas.

Since $^{6}Li_2^+/^{12}C^+$ is a mass doublet, the systematic effects were smaller than most of the other alkali ratio measurements. However, the statistical error was large. There was larger scatter than normal within a run (of an average of 4.5 x 10^{-10}) as well as scatter between successive runs.

Table 4.3 Average cyclotron frequency (*i.e.* inverse mass) ratios and systematic corrections for the alkali data. The upper half of the table lists ratios used for the final masses. The lower portion of the table are ratios measured as tests for systematic errors. *N* is the number of runs included in the average. Δ_{trap}, $\Delta_{i\text{-}i}$, and Δ_{fz} are the estimated systematic corrections in parts-per-trillion (ppt), with estimated uncertainty in parentheses, due to trap field imperfections, ion-ion interaction, and shifts in f_z due to ion-detector interaction and differential voltage drift, respectively. σ_{syst} is the total systematic error and σ_{stat} is the statistical error (in ppt) for each average ratio. <*R*> is the average ratio after applying systematic corrections, with statistical and systematic uncertainties combined in quadrature, in parentheses.

Ion pair	*N*	Δ_{trap}	$\Delta_{i\text{-}i}$	Δ_{fz}	Δ_{pol}	σ_{syst}	σ_{stat}	<*R*>
$^{6}Li_2^+/^{12}C^+$	7	3(55)	-2(20)	-1(33)	-	67	249	0.997 485 741 614(258)
$^{23}Na^+/^{20}Ne^+$	9	-784(427)	-345(415)	12(5)	-	595	38	0.869 620 239 184(596)
$^{12}C_2^+/^{23}Na^+$	9	-118(56)	-32(53)	-1(1)	-	77	74	0.957 906 091 266(107)
$^{40}Ar^+/^{39}K^+$	7	-170(95)	14(31)	-9(17)	-	101	33	0.975 009 239 187(106)
$^{41}K^+/^{40}Ar^+$	7	145(75)	-14(32)	-11(5)	-	82	52	0.975 600 318 068(97)
$^{40}ArH^+/^{41}K^+$	1	1(11)	0(1)	6(5)	92(2)	12	147	0.999 795 387 703(148)
$^{86}Kr^{3+}/^{85}Rb^{3+}$	1	-40(18)	7(1)	-37(19)	-	26	78	0.988 373 496 338(82)
$^{86}Kr^{2+}/^{85}Rb^{2+}$	2	46(37)	-15(11)	106(27)	-	47	50	0.988 373 570 567(69)
$^{85}Rb^{2+}/^{84}Kr^{2+}$	4	1(52)	-14(15)	37(27)	-	60	47	0.988 219 481 271(76)
$^{87}Rb^{2+}/^{86}Kr^{2+}$	3	-36(39)	18(8)	74(28)	-	49	49	0.988 510 045 784(69)
$^{133}Cs^{3+}/^{132}Xe^{3+}$	3	-8(31)	2(3)	12(15)	-	35	70	0.992 466 003 022(78)
$^{133}Cs^{3+}/^{129}Xe^{3+}$	3	30(27)	-9(7)	31(27)	-	39	70	0.969 897 994 594(80)
$^{23}Na^+/^{20}Ne^+$	9	-784(427)	-345(415)	12(5)	-	595	38	0.869 620 239 184(596)
$^{40}Ar^+/^{18}O_2^+$	3	-283(247)	36(93)	24(6)	-	264	46	0.900 803 755 223(268)
$^{40}ArH^+/^{40}Ar^+$	1	155(82)	-27(28)	-16(9)	-92(2)	87	129	0.975 400 698 085(156)
$^{12}C^{16}O_2^+/^{40}Ar^+$	8	-25(201)	80(55)	137(29)	-	210	56	0.908 444 829 304(217)
$^{86}Kr^{2+}/^{84}Kr^{2+}$	5	51(48)	-34(15)	20(24)	-	56	42	0.976 730 017 167(70)
$^{132}Xe^{3+}/^{129}Xe^{3+}$	6	19(21)	-17(10)	11(20)	-	31	55	0.977 260 673 537(63)

Atomic masses of ^{6}Li, ^{23}Na, $^{39,41}K$, $^{85,87}Rb$ and ^{133}Cs: To obtain the masses of neutral, ground state atoms, we first convert the cyclotron frequency ratios into mass differences between neutral atoms. To do this we account for the mass of the missing electrons, and the ionization and chemical binding energies, which we obtained from References [136-142]. The mass differences corresponding to the ratios in Table 4.3 are given in Table 4.4.

Table 4.4 Mass differences and derived atomic mass of the relevant alkali, corresponding to the ratios given in Table 4.3. For the mass differences, the statistical, systematic and total uncertainties are shown in parentheses, respectively. For the mass the total uncertainty, including that of the reference atom, is given.

Ion pair	Mass Difference	Result (u)	Atom	Mass (u)
$^{6}Li_2^{+}/^{12}C^{+}$	$2(^{6}Li) - ^{12}C$	0.030 245 774 8(30)(7)(31)	^{6}Li	6.015 122 887 4(31)
$^{23}Na^{+}/^{20}Ne^{+}$	$^{23}Na - ^{20}Ne$	2.997 329 114 7(9)(137)(137)	^{23}Ne	22.989 769 290(14)
$^{12}C_2^{+}/^{23}Na^{+}$	$2(^{12}C) - ^{23}Na$	1.010 230 717 2(18)(19)(26)	^{23}Ne	22.989 769 282 8(26)
$^{40}Ar^{+}/^{39}K^{+}$	$^{40}Ar - ^{39}K$	0.998 676 636 9(13)(41)(43)	^{39}K	38.963 706 485 6(52)
$^{41}K^{+}/^{40}Ar^{+}$	$^{41}K - ^{40}Ar$	0.999 442 134 8(21)(33)(39)	^{40}K	40.961 825 257 4(48)
$^{40}ArH^{+}/^{41}K^{+}$	$^{40}Ar + ^{1}H - ^{41}K$	0.008 382 900 5(60)(5)(61)	^{40}K	40.961 825 254 1(68)
$^{86}Kr^{3+}/^{85}Rb^{3+}$	$^{86}Kr - ^{85}Rb$	0.998 820 891 7(67)(23)(71)	^{85}Rb	84.911 789 736(10)
$^{86}Kr^{2+}/^{85}Rb^{2+}$	$^{86}Kr - ^{85}Rb$	0.998 820 892 8(43)(41)(59)	^{85}Rb	84.911 789 735(10)
$^{85}Rb^{2+}/^{84}Kr^{2+}$	$^{85}Rb - ^{84}Kr$	1.000 292 012 1(39)(51)(64)	^{85}Rb	84.911 789 743(10)
$^{87}Rb^{2+}/^{86}Kr^{2+}$	$^{87}Rb - ^{86}Kr$	0.998 569 906 8(42)(42)(59)	^{87}Rb	86.909 180 535(10)
$^{133}Cs^{3+}/^{132}Xe^{3+}$	$^{133}Cs - ^{132}Xe$	1.001 296 877 2(93)(46)(103)	^{133}Cs	132.905 451 963(15)
$^{129}Xe^{3+}/^{133}Cs^{3+}$	$^{133}Cs - ^{129}Xe$	4.000 671 097 5(90)(50)(103)	^{133}Cs	132.905 451 956(14)
$^{40}Ar^{+}/^{18}O_2^{+}$	$^{40}Ar - 2(^{18}O)$	3.964 063 913 3(18)(105)(107)		
$^{40}ArH^{+}/^{40}Ar^{+}$	^{1}H	1.007 825 041 8(53)(36)(64)		
$^{12}C^{16}O_2^{+}/^{40}Ar^{+}$	$^{12}C + 2(^{16}O) - ^{40}Ar$	4.027 446 119 2(24)(93)(96)		
$^{86}Kr^{2+}/^{84}Kr^{2+}$	$^{86}Kr - ^{84}Kr$	1.999 112 904 6(36)(48)(60)		
$^{132}Xe^{3+}/^{129}Xe^{3+}$	$^{132}Xe - ^{129}Xe$	2.999 374 222 9(73)(40)(83)		

The data in Table 4.4 is intended for use in global, least-squares mass evaluations. Here, for simplicity, we obtain the alkali masses directly from each of the mass differences listed in the top half of Table 4.3, treating the other atomic masses as references. The mass of ^{12}C is defined to be 12 u exactly. We used the masses of ^{1}H, ^{14}N, ^{20}Ne and ^{40}Ar as given in the AME2003 [90], and the masses of ^{84,86}Kr and ^{129,132}Xe from ref. [23]. For ^{23}Na, ^{41}K, ^{85}Rb and ^{133}Cs, where more than one mass value was determined, we took the weighted average, linearly propagating the systematic uncertainty and the uncertainties in the reference masses. Our final atomic masses are listed in Table 4.5 and are compared to the values from the AME2003 and other recent Penning trap measurements [49,143].

Table 4.5. Final atomic masses of ^{6}Li, ^{23}Na, ^{39,41}K, ^{85,87}Rb and ^{133}Cs obtained from the different ratios, and their weighted averages, compared with previous values.

Atom	This Work	AME2003 [90]	Other Penning Traps [49, 143]
^{6}Li	6.015 122 887 4(31)	6.015 122 795(16)	6.015 122 889(26)
^{23}Na	22.989 769 282 8(26)	22.989 769 280 9(29)	
^{39}K	38.963 706 485 6(52)	38.963 706 68(20)	38.963 706 52(17)
^{41}K	40.961 825 257 4(48)	40.961 825 76(21)	
^{85}Rb	84.911 789 738(9)	84.911 789 738(12)	
^{87}Rb	86.909 180 535(10)	86.909 180 527(13)	
^{133}Cs	132.905 451 960(13)	132.905 451 933(24)	

4.1.3 Discussion

The atomic masses of ^{23}Na, ^{85,87}Rb, and ^{133}Cs confirm the AME 2003 data, which is derived largely from data taken at MIT [65]. The good agreement between the masses presented in this paper and the MIT masses support our previous mass measurements of ^{84,86}Kr and ^{129,132}Xe.

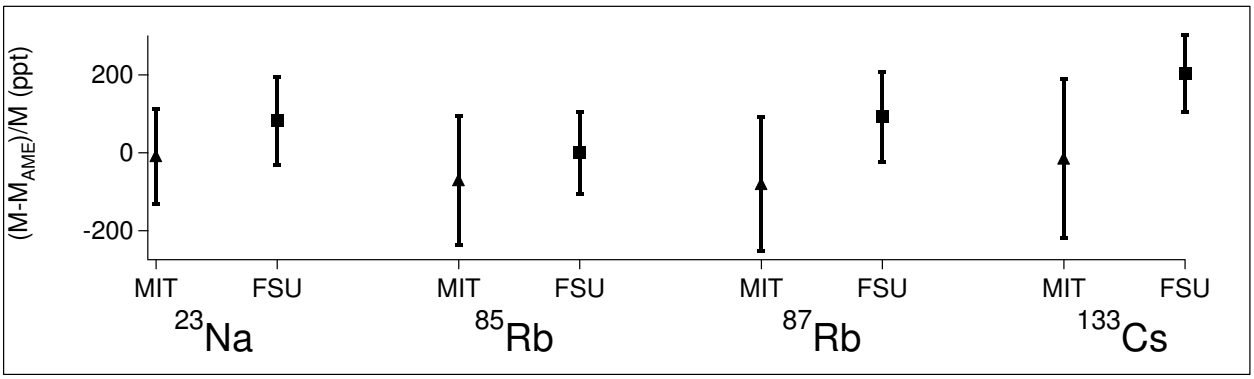

Figure 4.2 Comparison of masses from MIT, AME 2003, and FSU.

A measurement of the mass of ^{39}K by ISOLTRAP [143] was verified and improved by over a factor of 30. The first-ever Penning trap measurement of ^{41}K disagrees by over $2\sigma_{AME}$ with the AME 2003 value (calculated using neutron and proton capture experiments) and improves upon the precision by a factor of 40.

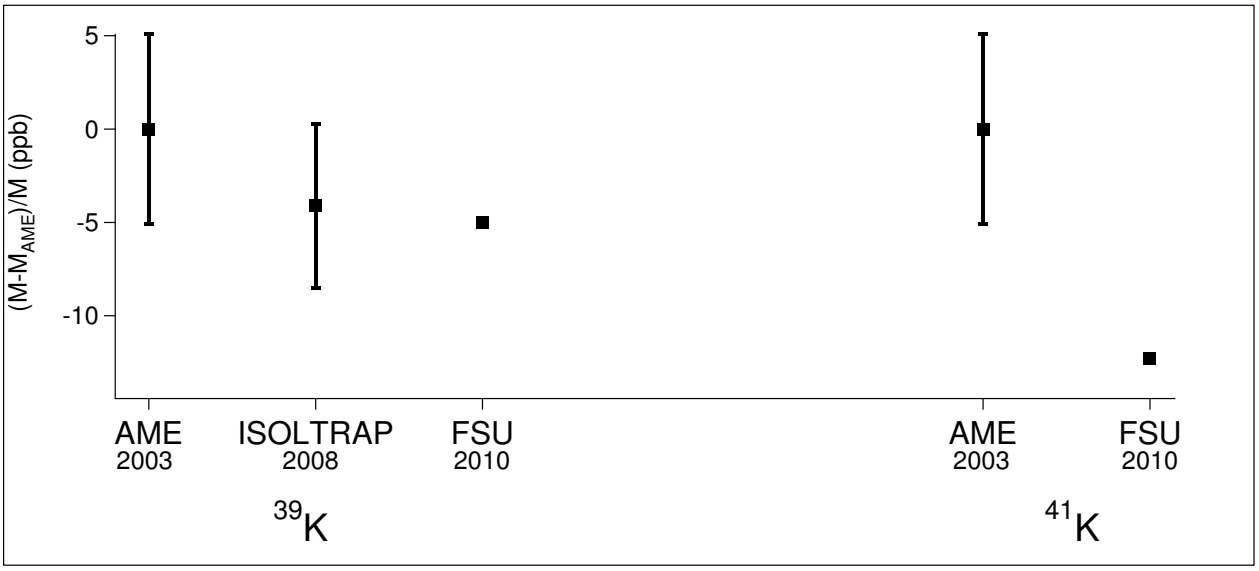

Figure 4.3 Comparison of potassium masses.

The ^{6}Li measured mass agrees with the measurements from the time-of-flight Penning traps (SMILETRAP and TITAN) [49,52] and improves the uncertainty of the previously most precise mass from the TITAN experiment by over a factor of eight. With this ^{6}Li mass, combined with the values of the masses of ^{7}Li [52] and the neutron [90] the *Q*-value of the ^{6}Li(n,γ)^{7}Li

reaction may be calculated: Q = 7251.101(5) keV. This Q-value obtained from the masses deviates significantly from the AME2003 [90] value of Q = 7249.97(8) keV measured by neutron capture experiments.

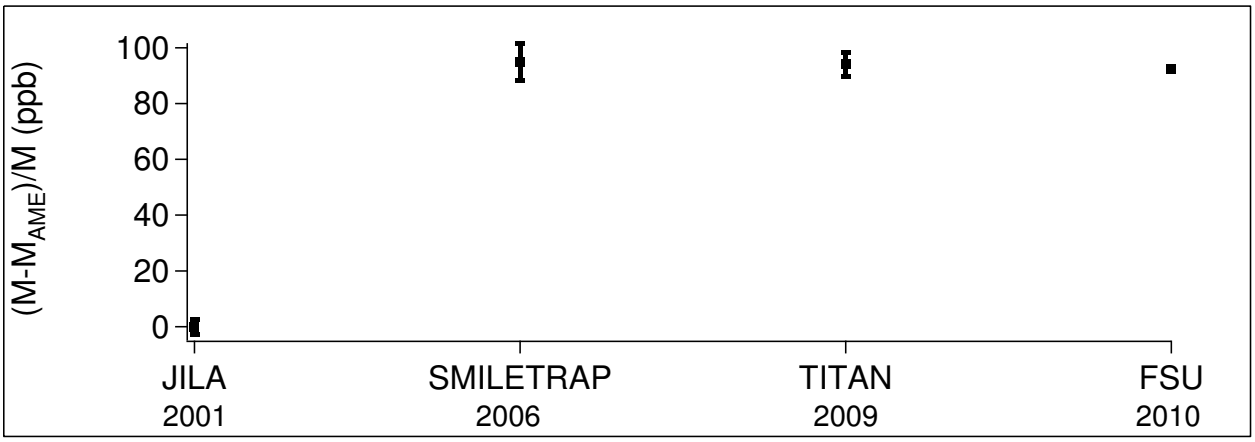

Figure 4.4 Comparison of Penning Trap mass measurements of ^{6}Li.

4.2 ^{18}O (and ^{19}F)

4.2.1 Motivation

This work was instigated following a request by Holger S.P. Müller and collaborators at the University of Cologne who have executed high precision rotational and vibrational spectroscopy, at GHz and THz frequencies, of carbon monoxide with all six stable isotopic variants (all combinations of ^{12,13}C and ^{16,17,18}O). They have analyzed the data in a manner similar to their work on SiS [144]. Their technique involves fitting their entire data set with a single Dunham expression for the rovibrational energy levels of a diatomic molecule (in this case CO) [145]:

$$E(\upsilon,J) = \sum_{ij} Y_{ij}\left(\upsilon + \frac{1}{2}\right)^{i} J^{j}(J+1)^{j} \qquad [4.4]$$

with the Dunham parameters for the different isotopomers given by the expression of Watson [146]:

$$Y_{ij} = U_{ij}\left(1 + \frac{m_e\Delta_{ij}^{C}}{M_C} + \frac{m_e\Delta_{ij}^{O}}{M_O}\right)\mu^{\frac{-(i+2j)}{2}} \qquad [4.5]$$

where J is the rotational angular momentum quantum number, υ is the vibrational quantum number, m_e is the electron mass, $\Delta^{C,O}$ are the Born-Oppenheimer break-down terms, $M_{C,O}$ is the atomic mass of the respective isotope and μ is the reduced mass $(M_C M_O)/(M_C+M_O)$.

In their preliminary analysis, the data gave a poor fit using masses for ^{16}O, ^{17}O and ^{18}O from the AME2003 tabulation [90]. They found a much better fit could be obtained by letting the least well determined mass in the AME 2003, that of ^{18}O, float. Doing this, they obtained a value of the mass of ^{18}O of 17.99915974 (5)(12)u [147] . The errors quoted in the parentheses are from the fit error and error in the mass of ^{17}O [m(^{17}O) = 16.99913170 (12)], respectively.

It was proposed that FSU measure the value of ^{18}O to the usual FSU-PPT precision of approximately 10^{-10} (an improvement of two orders of magnitude from the current accepted value), then let the Cologne group refit the data to obtain the various spectroscopic constants as well as a predicted mass of ^{17}O. While the trap was set up for this mass value, it was decided to also measure the mass of ^{19}F, so that the hydroflurocarbon series might be used as convenient mass references in the future. The mass of ^{18}O given in the AME2003 was determined from linking it to the mass of ^{16}O via nuclear decay and reaction data [90]. The mass of ^{19}F contained in the AME2003 [90] was measured using an rf spectrometer.

4.2.2 Experimental Details

As with the ^{23}Na data, the ^{18}O and ^{19}F measurements and analysis were mostly accomplished by Matt. Prior to these measurements, we had removed the insert containing the Penning trap and warmed it to room temperature. After re-cooling the insert, several measurements were performed to characterize the new trap environment. It was found that C_6 had increased by about a factor of 3 and also that the guard ring voltage required to make C_4 zero had shifted.

The mass of ^{18}O was measured using three different ratio comparisons: $^{12}CD_3^+/^{18}O^+$, $^{12}C_2D_6^+/^{18}O_2^+$, and $^{12}C_3^+/^{18}O_2^+$, and the mass of ^{19}F was measured using the ratios $^{13}CD_3^+/^{19}F^+$ and $^{28}SiH_3^+/^{12}C^{19}F^+$. In Table 4.6, the number of runs (N), the systematic corrections (Δ_{trap}, $\Delta_{i\text{-}i}$, Δ_{fz}, Δ_{pol}), errors (σ_{sys}, σ_{stat}) and the final ratios ($<R>$) for each ion pair are presented. It should be noted that while Δ_{trap}, $\Delta_{i\text{-}i}$ and Δ_{fz} are those shifts outlined in Section 2.3, there is an additional shift Δ_{pol} applied to the CF^+ data due to a dipole moment and hence polarizability shift as discussed in Chapter 5.

Table 4.6 Error budgets for mass ratios obtained during the ^{18}O and ^{19}F experiments.

Ion pair	N	Δ_{trap}	$\Delta_{i\text{-}i}$	Δ_{fz}	Δ_{pol}	σ_{sys}	σ_{stat}	$\langle R \rangle$
$^{12}CD_3^+/^{18}O^+$	7	-6(37)	-1(3)	-7(11)	–	39	30	0.997 608 564 116(50)
$^{12}C_2D_6^+/^{18}O_2^+$	7	3(51)	0(7)	7(13)	–	54	55	0.997 608 600 273(78)
$^{12}C_3^+/^{18}O_2^+$	3	0(16)	-4(51)	-9(12)	–	55	88	0.999 953 311 506(104)
$^{13}CD_3^+/^{19}F^+$	5	-1(26)	0(17)	5(10)	–	32	35	0.997 518 681 645(48)
$^{28}SiH_3^+/^{12}C^{19}F^+$	6	-1(17)	9(38)	0(10)	-80(40)	59	42	0.999 935 533 127(72)

The mass difference was obtained from the cyclotron frequency ratio of the ions (Table 4.7).

Table 4.7 Mass difference equations corresponding to the ratios given in Table 4.6. The statistical, systematic and total errors are shown in parentheses.

Ion Pair	Mass Difference	Result (u)
$^{12}CD_3^+/^{18}O^+$	$^{12}C + 3(D) - {}^{18}O$	0.043 145 722 16(54)(69)(88)
$^{12}CD_6^+/^{18}O_2^+$	$^{12}C + 3(D) - {}^{18}O$	0.043 145 721 16(98)(95)(136)
$^{12}C_3^+/^{18}O_2^+$	$3(^{12}C) - 2(^{18}O)$	0.001 680 769 5(32)(20)(38)
$^{13}CD_3^+/^{19}F^+$	$^{13}C + 3(D) - {}^{19}F$	0.047 257 006 69(66)(62)(91)
$^{28}SiH_3^+/^{12}C^{19}F^+$	$^{28}Si + 3H - {}^{12}C - {}^{19}F$	0.001 998 468 7(13)(18)(22)

The masses of ^{18}O and ^{19}F were obtained from the mass differences and the reference masses. The final masses were the weighted averages of the masses for each data set, where the systematic errors and errors in the mass references have been linearly propagated. The good agreement between the three values of the mass of ^{18}O obtained using different reference ions lends high confidence to the final mass.

Table 4.8 Masses for ^{18}O and ^{19}F from various sources

Atom	Source	Atomic Mass (u)
^{18}O	$^{12}CD_3^+/^{18}O^+$	17.999 159 612 3(10)
	$^{12}C_2D_6^+/^{18}O_2^+$	17.999 159 613 3(15)
	$^{12}C_3^+/^{18}O_2^+$	17.999 159 615 3(20)
	Final Average	17.999 159 613 0(13)
	AME2003	17.999 161 0(7)
	Savard *et al.* [148]	17.999 159 35(25)
^{19}F	$^{13}CD_3^+/^{19}F^+$	18.998 403 163 0(11)
	$^{28}SiH_3^+/^{12}C^{19}F^+$	18.998 403 162 5(23)
	Final Average	18.998 403 162 9(11)
	AME2003	18.998 403 22(7)

4.2.3 Discussion

The suspicions of the researchers at the University of Cologne are therefore confirmed in that the mass of ^{18}O is lower than the accepted AME 2003 value by 1.4(7) μu. It should also be mentioned that after measuring the mass of ^{18}O, the FSU group became aware of a measurement by the Canadian Penning Trap (CPT) [148]. The FSU-PPT and CPT measurements agree, with the FSU-PPT contributing over two orders of magnitude improvement in the mass. In addition, our results for the mass of ^{19}F agree with the AME 2003 value, but are a factor of 60 more precise.

4.3 ^{17}O

4.3.1 Motivation

Since the masses of $^{16,18}O$ have been measured precisely, they can now be used in the fit of the molecular spectra to provide a value for the mass of the now least precisely known isotope: ^{17}O. This was done, and the result was: m(^{17}O) = 16.999 131 644(30). The FSU-PPT then measured the mass of ^{17}O, thus providing a precise test of the fitting methodology for the

molecular spectra, and in particular of the Dunham and Watson expressions above which are used to relate rovibrational spectra of different isotopic variants. In particular, it provides a bound on the size of second order Born-Oppenheimer breakdown parameters.

4.3.2 Experimental Details

To determine the mass of ^{17}O, two ratios were measured: $^{17}O_2^+/^{28}SiD_3^+$ and $^{17}O^+/^{16}OH^+$. These measurements were separated by six months. While a total of ten runs were taken of the ratio of $^{17}O^+/^{16}OH^+$, only four were taken under "optimum conditions" (ρ_{ci} = 100 μm, ρ_{ck} = 1 .8 mm). The rest were taken with varied ρ_{ci} and ρ_{ck} and used as systematic tests. Eight runs were averaged to find the final frequency ratio for $^{17}O_2^+/^{28}SiD_3^+$, completed with three different $^{17}O_2^+$ ions. As tests, other runs were measured which varied the inner and parking cyclotron radii, and no significant systematic variation was observed.

Table 4.9. Average cyclotron frequency ratios (*i.e.* inverse mass ratios) and systematic corrections for the ^{17}O data. *N* is the number of runs. Δ_{trap} is the estimated systematic correction in ppt, with uncertainty in parentheses, for trap field imperfections; $\Delta_{i\text{-}i}$ for ion-ion interaction; Δ_{fz} for shifts in f_z due to ion-detector interaction and differential voltage drift; and Δ_{mol} for polarizability shifts (for OH^+) and vibrational excitation (for $^{17}O_2^+$), respectively. σ_{sys} is the total systematic uncertainty and σ_{stat} is the statistical uncertainty (in ppt) for each average ratio. <*R*> is the average ratio after applying systematic corrections, with statistical and systematic uncertainties combined in quadrature.

Ion pair	*N*	Δ_{trap}	$\Delta_{i\text{-}i}$	Δ_{fz}	Δ_{mol}	σ_{sys}	σ_{stat}	<*R*>
$OH^+/^{17}O^+$	4	0(25)	0(5)	−1(28)	−161(9)	39	82	0.999 787 798 486(91)
$^{28}SiD_3^+/^{17}O_2^+$	8	−1(16)	0(3)	−1(3)	−13(7)	18	33	0.999 383 622 618(38)

The largest systematic shift in the monomer ratio was due to the polarizability of OH^+. However, the largest systematic uncertainty resulted from C_4z^2. The largest contributor to the systematic uncertainty for the dimer ratio was also from the C_4z^2 shift to the axial frequency.

Table 4.10 Mass difference equations corresponding to the ratios given in Table 4.9. The statistical, systematic and total uncertainties are shown in parentheses.

Ion Pair	Mass Difference	Result (u)
$^{16}OH^+/^{17}O^+$	$^{16}O + H - {}^{17}O$	0.003 607 896 1 (14)(7)(16)
$^{28}SiD_3^+/^{17}O_2^+$	$^{28}Si + 3D - 2(^{17}O)$	0.020 968 355 7 (12)(7)(14)

Table 4.11 Atomic masses for ^{17}O obtained from the different ratios, and their weighted average, compared with the result of the AME2003 and the Cologne group's molecular spectroscopy result.

Source	Mass (u)
$OH^+/^{17}O^+$	16.999 131 755 5(16)
$^{28}SiD_3^+/^{17}O_2^+$	16.999 131 756 9(9)
Weighted Average	16.999 131 756 6(9)
AME 2003	16.999 131 70 (12)
Cologne	16.999 131 644 (30)

4.3.3 Discussion

From Table 4.11, it is evident that while the new FSU-PPT mass of ^{17}O agrees with the AME 2003 value, it differs from the Cologne group's value by 6.6(1.8) ppb. This difference could be due to the neglect of second-order Born-Oppenheimer terms in Equation 4.5, however it is more likely that uncertainties of some of the molecular spectroscopy data have been underestimated. This comparison, with agreement below 10 ppb, of the FSU-PPT mass of ^{17}O and the Cologne mass is the most precise test to date of the Dunham-Watson model, with first order Born-Oppenheimer breakdown parameters.

5. MEASUREMENTS OF MOLECULAR ION ELECTRONIC DIPOLE MOMENTS BY MEASURING POLARIZABILITY SHIFTS TO THE CYCLOTRON FREQUENCY

5.1 Motivations for Measurements of Molecular Ion Electric Dipole Moment

Aside from the measurement of an ion's mass, another fundamental quantity of a molecular ion may be measured in a Penning trap: its electric dipole moment[16]. This chapter describes measurements of the dipole moments of HCO^+ and NH^+. Both HCO^+ and NH^+ were chosen because they have large polarizabilities in their ground state, leading to measurable shifts in the cyclotron frequency. As opposed to neutral molecules, there are very few laboratory measurements of dipole moments of molecular *ions*, while there have been extensive theoretical calculations [135,150]. An FSU-PPT measurement would confirm the theoretical calculations with an experimental value. The many theoretical calculations of the dipole moments (which determine the strength of pure rotational transitions) may be attributed to their use in various astrophysical calculations.

HCO^+ has a rich history in astrophysics as it was in fact the first molecular ion discovered by radio astronomical observation [151]. It has now been observed in stellar atmospheres, comets, and in a variety of environments in the interstellar medium including giant molecular clouds, starbursts, active galactic nuclei, and in the dense cores of dark molecular clouds [152-155]. In addition, HCO^+ is used as a H_2 mass tracer [156]. The dipole moment of HCO^+ is used in many of these studies to determine the column densities, and is also used in modeling dissociative recombination of HCO^+ in interstellar clouds [157].

NH^+ has not yet been observed in space. However, it has been postulated that NH^+ should be present in interstellar molecular clouds and in the tails of comets [158-160]. Besides the possible astrophysical applications, NH^+ was an attractive candidate to measure due to its large expected polarizability shifts. In fact, NH^+ has the largest polarizability of the hydride cations $LiH^+ \rightarrow ArH^+$, as noted in [135].

---

[16] In this chapter, by dipole moment we mean the body frame electric dipole moment, as if the atomic nuclei could be fixed. A state of definite parity has no electric dipole moment in the laboratory frame.

5.2 Polarizability Shifts to the Cyclotron Frequency

The polarizability of an ion causes a shift (termed a polarizability shift) in its cyclotron frequency given by [135]:

$$\frac{\Delta\omega_c}{\omega_c} = \frac{-\alpha B^2}{m} \qquad [5.1]$$

where B is the magnetic field, m is the mass of the ion, and α is the polarizability. This expression can be obtained by including a term in the Lagrangian of an ion moving in the magnetic field to allow for the potential energy of a polarizable object due to the $\bar{v}x\bar{B}$ motional electric field seen by the object [39,78]:

$$V = -\frac{1}{2}\alpha E^2 = -\frac{1}{2}\alpha\left(\bar{v}x\bar{B}\right)^2 \qquad [5.2]$$

The energy shift due to the polarizability in Equation 5.2 is also known as the quadratic Stark Effect and can be obtained from second order perturbation theory. Hence, the polarizability of an ion in state $|i\rangle$ is given by a summation dependent on the dipole matrix elements, $\langle j|\mu_X|i\rangle$, and the transition energies, E_j-E_i, between its states [135,161]:

$$\alpha_{XX}(i) = 2\sum_{j\neq i}\frac{\left|\langle j|\mu_X|i\rangle\right|^2}{E_j - E_i} \qquad [5.3]$$

Note that $\alpha_{XX} = \alpha_{YY}$ is the component of the polarizability tensor corresponding to an electric field perpendicular to the quantization axis (determined by the magnetic field), as is the case for the $\bar{v}x\bar{B}$ motional electric field, and so is the appropriate component to use in Equation 5.1.

5.3 Calculating Orientation Polarizabilities of Linear Molecules

Equation 5.3 is a general equation for calculating the electric dipole polarizability of any atom or molecule. For *linear molecules*, it is convenient to use the Born-Oppenheimer approximation where the Hamiltonian and the wave function of a molecule may be separated into electronic, vibrational and rotational parts. Since electrons have lighter mass yet experience the same fields as the nuclei, they have higher velocities. Therefore, the electronic structure is calculated assuming the nuclei are fixed.

While a linear molecule is not spherically symmetric, there is cylindrical symmetry along the internuclear axis. The component of electronic orbital angular momentum along the internuclear axis is generally denoted using the quantum number, Λ. Analogous to spectroscopic

atomic notation (which employs Latin letters), the $\Lambda = 0,\pm1,\pm2$ states are denoted by Σ, Π, Δ [162,163]. Additionally, superscripts are used to represent the electronic spin and parity of the state. For example, the ground electronic state of HCO^+ is denoted $^1\Sigma^+$, indicating a closed electronic shell with electronic quantum numbers of $S = 0$, $\Lambda = 0$, and + parity. On the other hand, NH^+ has a ground electronic state of $^2\Pi$.

The nuclear contribution to the Hamiltonian corresponds to vibrational and rotational excitation. For each electronic state, there is a series of vibrational levels designated by the quantum numbers v_1, v_2, v_3, etc. for each mode of vibration. For each of these vibrational levels, there is then a series of rotational levels. The total angular momentum of the molecule, which is the combination of electronic angular momentum and the angular momentum due to the motion of the nuclei is denoted J.

In the cryogenic environment of a Penning Trap, the ion is in its ground electronic and vibrational ($v = 0$) energy states, and only the lowest rotational states are populated. Following the terminology in Reference [135], the "distortion polarizability" (polarizability due to the rearrangement of charge within a molecule) may be neglected at this temperature in favor of the larger "orientation polarizability" (polarizability due to the rotational alignment of the body frame dipole moment of the molecule with the external electric field).

5.3.1 HCO^+ Molecular Structure and Polarizability

For electronic and vibrational quantum numbers equal to zero, the rotational quantum number is equal to the total angular momentum quantum number. The energy for a rotational state with rotational quantum number J can be approximated by the energies of a rigid rotor: $E_J = B_0 J(J+1)$[163], where B_0 is the rotational constant. The energy level diagram for the lowest rotational levels $J = 0,1,2$ of HCO^+ is given in Figure 5.1.

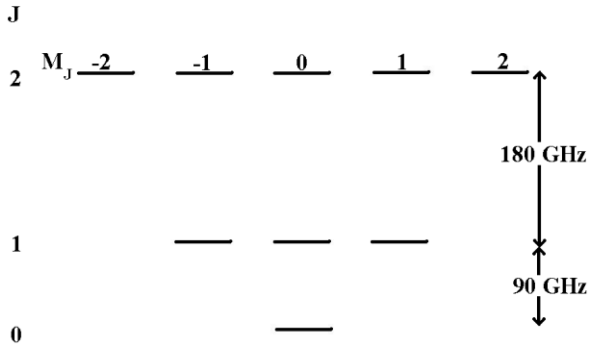

Figure 5.1 Energy level diagram of HCO^+ for rotational levels *J = 0,1,2* in its electronic and vibrational ground state [164].

Using rigid rotor wave functions, Equation 5.3 becomes [162]:

$$\alpha_{XX}(J,M_J)=\begin{cases}\dfrac{\mu^2}{3B_0} & for \quad J=0\\ \left[\dfrac{J(J+1)-3M_J^2}{2J(J+1)(2J-1)(2J+3)}\right]\dfrac{\mu^2}{B_0} & for \quad J\neq 0\end{cases} \qquad [5.4]$$

Clearly, the polarizability of the ion depends on the ion's *(J, M_J)* state. This expression for the polarizability can then be substituted into Equation 5.1 to determine the cyclotron frequency shifts for an ion in state *(J,M_J)*.

Table 5.1 Polarizabilities, α, and resultant cyclotron frequency shifts, $\Delta\omega_c/\omega_c$, for the lowest rotational levels of HCO^+ assuming μ = 3.888(4)D and B_0 = 44594.42873(28) MHz [135,150,164]. An atomic unit of polarizability is equal to $4\pi\varepsilon_0 a_0^3$, where ε_0 is the permittivity of free space, and a_0 is the Bohr radius.

(J, M_J)	α (au)	$\Delta\omega_c/\omega_c$ (ppb)
(0,0)	115078	-2.867
(1,-1)	-17262	0.430
(1,0)	34523	-0.860
(1,1)	-17262	0.430
(2,-2)	-8220	0.205
(2,-1)	4110	-0.102
(2,0)	8220	-0.205
(2,1)	4110	-0.102
(2,2)	-8220	0.205

5.3.2 NH^+ Molecular Structure and Polarizability

Unlike HCO^+, the electronic ground state of NH^+ does not have a closed electron shell. It falls under the category of Hund's Rule (a) in that is has a well-defined component of electronic angular momentum along the internuclear axis, Λ, and component of spin, Σ [163], along the internuclear axis that couple to give a total component of electronic angular momentum designated by Ω.

The electronic ground state of NH^+ has $|\Lambda| = 1$ and $|\Sigma| = ½$, coupling to give $\Omega = \pm ½$. Therefore, the electronic ground state is doubly degenerate, and the sign of Ω dictates whether the electronic angular momentum is directed towards or away from the H atom. This degeneracy is lifted by interactions of the electronic and rotational states, resulting in two close lying states of opposite parity, which are known as lambda doubling components. These two close lying states of opposite parity result in a large polarizability due to the small E_i-E_j denominator of Equation 5.3. The $^2\Pi_{1/2}$, $v=0$, $J=1/2$ and $3/2$ levels of NH^+ are shown as a function of magnetic field in Figure 5.2 [135].

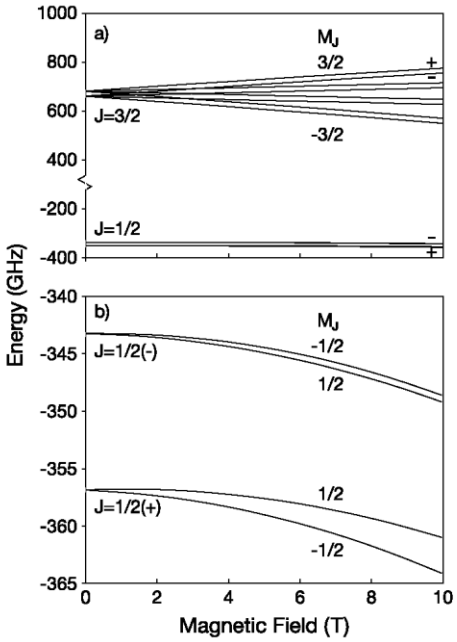

Figure 5.2 Zeeman energies of NH^+, $X^2\Pi_{1/2}$ (v = 0), B = 0-10T. (a) v=0, J= 1/2 , 3/2, (b) expanded view of J=1/2 [135].

The polarizability cannot be given in a simple expression, but has been calculated as a function of magnetic field using energies and matrix elements obtained from an effective Hamiltonian [135].

Table 5.2 Polarizabilities from the theoretical calculations of Reference [135] and resultant cyclotron frequency shifts for NH^+.

J	M_J	α (au)	$\Delta\omega_c/\omega_c$ (ppb)
$\frac{1}{2}^+$	−½	64300	−3.09
$\frac{1}{2}^+$	+½	74205	−3.57
$\frac{1}{2}^-$	−½	−71009	3.42
$\frac{1}{2}^-$	+½	−61105	2.94

5.4 Polarizability "Jumps"

The above sections show how the polarizability, and hence shifts to the cyclotron frequency depend on the state of an ion. When an ion makes a transition between two states, the cyclotron frequency data shows a "jump." This was first discovered at MIT. While carrying out a measurement of a mass ratio involving CO^+, seemingly unexplainable jumps in that ion's cyclotron frequency were observed. These jumps were eventually understood to be caused by jumps in the polarizability of CO^+ and are similar to the jumps in HCO^+ reported here [63].

Remarkably, in addition to spontaneous emission, absorption of black body radiation also induces transitions between energy levels of an ion within the Penning Trap. The transition rate due to absorption of black body photons from state $|j\rangle$ to state $|i\rangle$ is given by ($E_i > E_j$):

$$\Gamma_{abs} = \bar{n} A_{ij} \qquad [5.5]$$

where A_{ij} is the Einstein coefficient for spontaneous emission for the electromagnetic transition from level $|i\rangle$ to $|j\rangle$. $\bar{n}$ is the mean number of photons per mode at frequency $\nu_{ij} = \frac{E_i - E_j}{h}$ and temperature T, and is given by the black body (Planck) distribution:

$$\bar{n} = \frac{1}{e^{h\upsilon_{ij}/k_B T} - 1} \qquad [5.6]$$

where k_B is the Boltzmann constant. Likewise, stimulated emission increases the transition rate $|i\rangle$ to $|j\rangle$ to $\Gamma_{spont}+\Gamma_{stim}=(\bar{n}+1)A_{ij}$. For an electric dipole transition [158, 165],

$$A_{ij}=\frac{16\pi^3\upsilon_{ij}^{\ 3}}{3\varepsilon_0 hc^3}\left|\mu_{ij}\right|^2 \qquad [5.7]$$

Here, ε_0 is the permittivity of free space, c is the speed of light, and μ_{ij} is the dipole matrix element.

5.4.1 HCO^+ Jump Rate

For a linear molecule with no electronic orbital angular momentum, like HCO^+, the electric dipole matrix elements are given by [162]:

$$\left|\mu_{ij}\right|^2=\sum_{m_i}\left|\langle im_i|e\vec{r}|jm_j\rangle\right|^2=\begin{cases}\dfrac{\mu^2(J+1)}{2J+1} & J\rightarrow J+1\\ \dfrac{\mu^2(J+1)}{2J+3} & J+1\rightarrow J\end{cases} \qquad [5.8]$$

For the transition $J=0\rightarrow 1$ (see Figure 5.1), $|\mu_{ij}|^2=\mu^2$, resulting in a calculated lifetime against absorption of approximately 4.0 hours (assuming a black body radiation temperature of 4.2K). See Table 5.3 for the details of the estimation.

Table 5.3 Quantities needed in the calculation of the lifetime against absorption of the ground state of HCO^+, assuming T = 4.2K, μ = 3.888(4)D and B_0 = 44594.42873(28) MHz [150,164] and standard CODATA [91] values for the other constants.

$\|\mu_{01}\|^2$	2.340 $(ea_0)^2$
ν_{01}	89.188 857 46 GHz
A_{01}	1.248 x 10^{-4} s^{-1}
$\bar{n}$	0.56
τ_{01}	4.0 hrs

Data was taken over a two week period, and the observed mean lifetime of the $J=0$ state (the time the HCO^+ was observed in the $J=0$ state divided by the number of observed jumps) was approximately 3.4(1.0) hours.

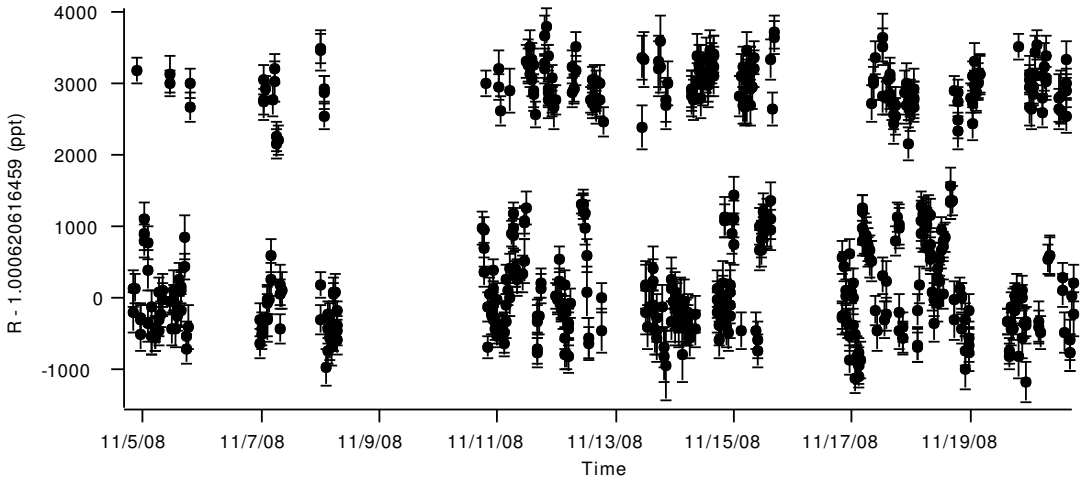

Figure 5.3 All cyclotron data for HCO^+, showing polarizability jumps. The vertical axis is proportional to the polarizability of the HCO^+ ion. $R = f_c[SiH^+]/f_c[HCO^+]$.

5.4.2 NH^+ Jump Rate

Since the *J=3/2* rotational level is approximately 1000 GHz above *J=1/2* (See Figure 5.2), transitions to *J=3/2* can be neglected (assuming black body radiation of 4.2K), so we only consider jumps between the lambda doubling states $J=1/2^+$ and $J=1/2^-$. The lifetime of the upper $J=1/2^-$ state against spontaneous decay and stimulated emission may be estimated using the Einstein coefficient for spontaneous emission, A_{ij}, following the same method as HCO^+. For molecules with electronic orbital angular momentum in Hund's case (a), the *z*-component of the dipole matrix element in the laboratory frame is given by [166]:

$$\left|\left\langle J\Omega M_J\left|\mu_z\right|J'\Omega' M_J'\right\rangle\right|^2 = \mu^2\begin{pmatrix} J & 1 & J' \\ -M_J & 0 & M_J' \end{pmatrix}^2\begin{pmatrix} J & 1 & J' \\ -\Omega & 0 & \Omega' \end{pmatrix}^2 (2J+1)(2J'+1) \qquad [5.9]$$

Here, $J = J' = ½$, $M_J = M_J' = ½$, and $\Omega = \Omega' = ½$, leading to $|\mu_z|^2 = \mu^2/9$. By symmetry, for the *J=1/2* states, $|\mu_{ij}|^2 = 3|\mu_z|^2 = \mu^2/3$. Assuming $\mu = 0.790$ ea_0, the spontaneous emission coefficient is $A_{ij} = 3.9(4)\times10^{-8}$ s^{-1}, and the mean lifetime for the $J = ½^-$ state against spontaneous and stimulated emission at 4.2 K is approximately 42 days. In fact, there was an observation of one polarizability jump from $J = ½^-$ to $J = ½^+$ during only one run, over the course of the approximately 150 hours (6 days) of data.

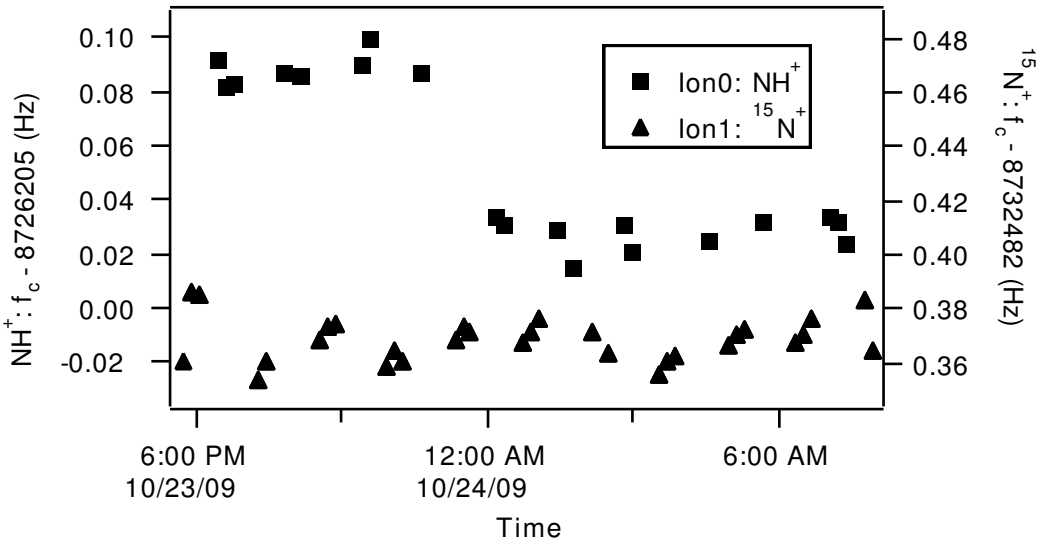

Figure 5.4 The only set of NH^+ vs $^{15}N^+$ data showing a jump in the polarizability of NH^+. This jump corresponds to a jump from *J=1/2*$^-$ to *J=1/2*$^+$.

5.5 HCO^+ Data Collection and Analysis

The HCO^+ data was comprised of 25 runs collected over a two week period. HCO^+ was made by heating polymerized formaldehyde (also known as polyoxymethylene and marketed as Delrin by Dupont [167]) in our vapor loader.

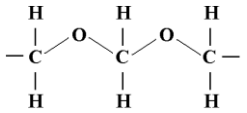

Figure 5.5 Chemical structure of Delrin, or polyxymethylene.

$^{28}SiH^+$ was chosen as the reference ion because it is a mass-doublet with HCO^+ and the masses of ^{28}Si and H are known to 0.02 and 0.1 ppb, respectively [69,90]. It was made by introducing Silane (SiH_4) gas into the Penning Trap. $^{28}SiH^+$ in fact has its own small dipole moment, but the resultant constant polarizability shift of 7 ppt is small, and was accounted for in the analysis. During each run, four HCO^+ PNP cycles were alternated with two $^{28}SiH^+$ PNP cycles (see Figure 5.5).

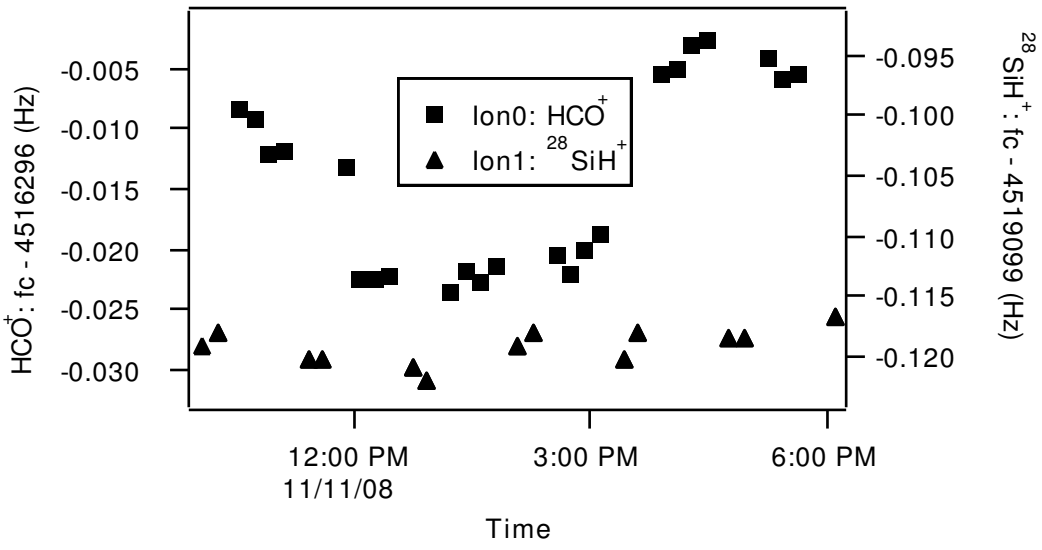

Figure 5.6 Sample HCO+ Run.

Since the HCO^+ and $^{28}SiH^+$ cyclotron frequencies were not obtained at exactly the same time, two interpolation methods were developed for obtaining the ratio for each HCO^+ PNP cycle. Each determines the effective value of the $^{28}SiH^+$ cyclotron frequency at the time of every HCO^+ cyclotron frequency measurement. The first fits the $^{28}SiH^+$ data to a polynomial, and then uses the equation for the polynomial to obtain an interpolated $^{28}SiH^+$ cyclotron frequency corresponding to the time of the measurement of the HCO^+ cyclotron frequency. The second (piece-wise) method simply used the average of the two $^{28}SiH^+$ measurements before and after each HCO^+ measurement. The entire set of data was analyzed using these two procedures.

A histogram was then compiled where the x-axis is the measured ratio for each HCO^+ PNP cycle and the y-axis the number of PNP cycles. The resultant three peaks (see Figures 5.7 and 5.8) coincide with the predicted $(J, M_J) = (0,0), (1,0)$ and $(1,\pm1)$ polarizability shifts (See Section 5.3.1). Data corresponding to $J \geq 2$ would be clustered near the unshifted frequency (0 on the x-axis) and does not produce resolvable peaks.

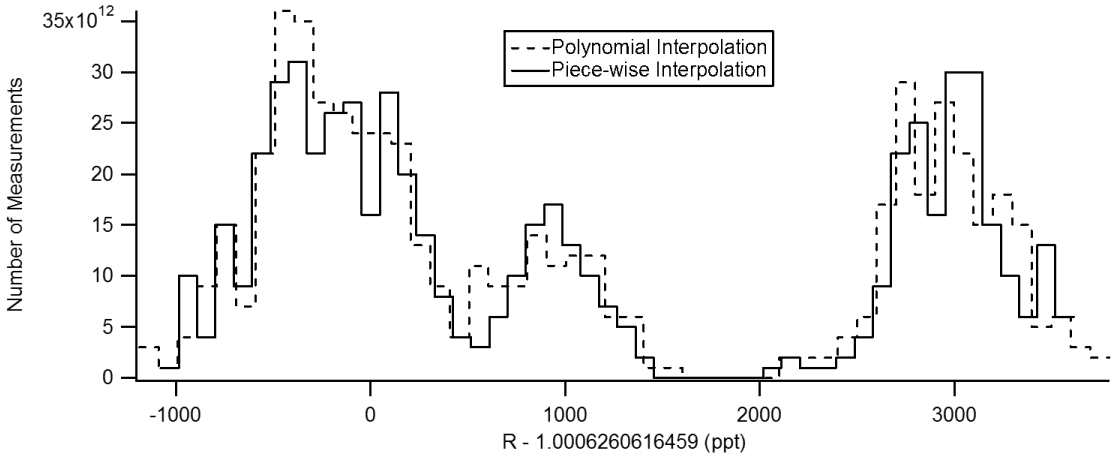

Figure 5.7 Piece-wise versus Polynomial Interpolation.

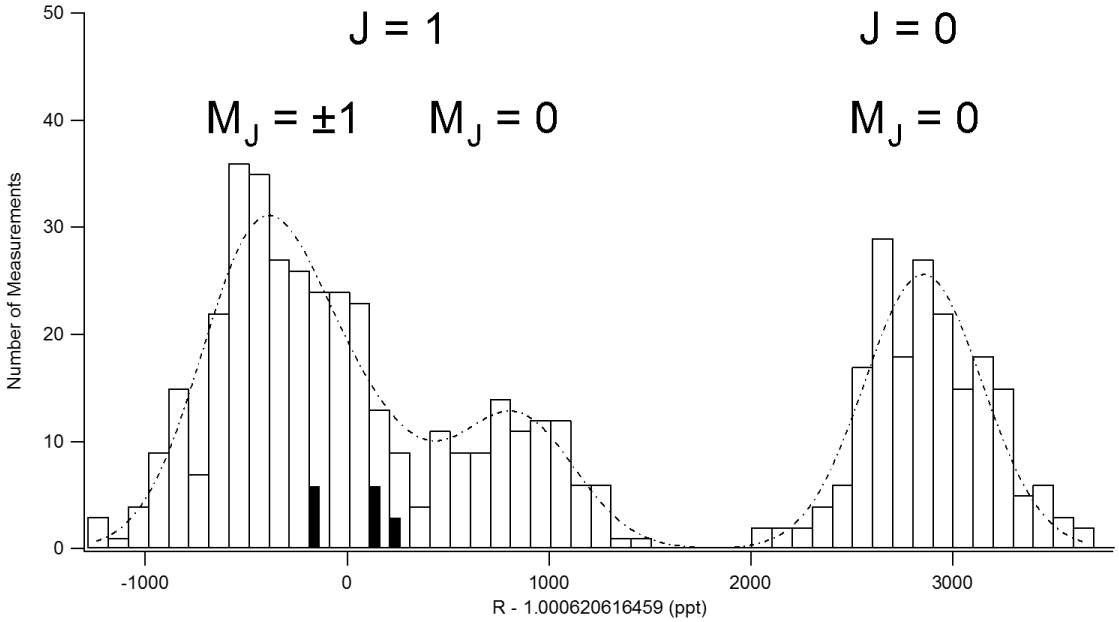

Figure 5.8 All cyclotron frequency measurement shifts, indicating the states of the HCO^+ ion. The dotted line indicates the fit to the histogram (the reduced X^2 for this fit is 1.02). The solid bars indicate the position and amplitude of the *J=2* for the temperature returned from the fit.

Only two HCO^+ ions were needed for the entire two week measurement, indicating good vacuum conditions in the trap. Each run was taken under the same conditions (same ρ_{ci}, ρ_{ck}, etc.). A parking radius of only 1 mm was used to facilitate a quick interchange of ions, consequently the ion-ion interaction (Sec 2.3.5) produced the largest systematic shifts and errors. The expected

cyclotron frequency ratio from the ion masses and after applying the corrections for the systematic shifts was $f_c[^{28}SiH^+]/f_c[HCO^+] = 1.000\ 620\ 616\ 459(156)$.

This expected ratio was subtracted from the observed ratio to produce the x-scale for the histograms in Figures 5.7 and 5.8. To determine the dipole moment, each peak was fitted with a Gaussian lineshape [39]:

$$f(R) = e^{\left(\frac{R - b\Delta R_{JM} - R_0}{\sigma}\right)^2} \qquad [5.10]$$

Each peak is centered around $b\Delta R_{JM}+R_0$, where R_0 is the ratio that would be observed without the polarizability of HCO^+, and ΔR_{JM} is the shift of the peak corresponding to the state $(J, \pm M)$ that is *calculated* from the theoretical values of μ and B_0 (See Table 5.1). For example, combining Equations 5.1 and 5.4, for $(J, M_J) = (0,0)$:

$$\Delta R_{00} = \frac{\Delta\omega_c}{\omega_c} = -\frac{\mu^2 B^2}{3mB_0} \qquad [5.11]$$

The parameter b (which the fit determines) is the ratio of the observed shifts to the predicted shifts, which are proportional to the dipole moment squared. Therefore, it follows that the observed dipole moment is $\mu_{obs} = \sqrt{b}\mu_{pred}$.

The amplitudes of the peaks give information about the relative populations of the levels. Assuming the ion is in thermal equilibrium with the environment at temperature, T, the Boltzmann distribution gives the relative population of state J as:

$$P(J) = g_J e^{-E_J/k_B T} = (2J+1)e^{-B_0 J(J+1)/k_B T} \qquad [5.12]$$

where the degeneracy g_J is the number of M_J states and the energy is given by the rigid rotor expression in Section 5.3.1 for each rotational state J. The ratio of the amplitudes of the peaks can therefore be used to determine a rotational temperature for the ion.

Table 5.4 Expressions for the amplitudes of the peaks in the histogram of the ratio of the cyclotron frequencies of HCO^+ versus $^{28}SiH^+$ assuming a Boltzmann distribution at temperature *T*.

(J, M)	Amplitude		
(0,0)	a_{00}	=	a_{00}
(1,0)	$a_{00}\exp(-2B_0/k_BT)$	=	$a_{00}a_1$
(1,1)	$2a_{00}\exp(-2B_0/k_BT)$	=	$2a_{00}a_1$
(2,0)	$a_{00}\exp(-6B_0/k_BT)$	=	$a_{00}(a_1)^3$
(2,1)	$2a_{00}\exp(-6B_0/k_BT)$	=	$2a_{00}(a_1)^3$
(2,2)	$2a_{00}\exp(-6B_0/k_BT)$	=	$2a_{00}(a_1)^3$

The actual lineshape used to perform the fit was:

$$f(R) = a_{00}e^{-\left(\frac{R-b\Delta R_{00}-R_0}{\sigma}\right)^2} + a_{00}a_1e^{-\left(\frac{R-b\Delta R_{10}-R_0}{\sigma}\right)^2} + 2a_{00}a_1e^{-\left(\frac{R-b\Delta R_{11}-R_0}{\sigma}\right)^2} + a_{00}a_1^3e^{-\left(\frac{R-b\Delta R_{20}-R_0}{\sigma}\right)^2} + 2a_{00}a_1^3e^{-\left(\frac{R-b\Delta R_{21}-R_0}{\sigma}\right)^2} + 2a_{00}a_1^3e^{-\left(\frac{R-b\Delta R_{22}-R_0}{\sigma}\right)^2} \quad [5.13]$$

where *T* is the temperature in K, and σ is the usual Gaussian standard deviation corresponding to the scatter in our measurement of the cyclotron frequency. In the analysis of this data, the ΔR_{JM} have been fixed to the calculated values (See Table 5.1) and all other parameters are allowed to float.

Table 5.5 Results from fitting the histograms of the ratio of the cyclotron frequencies of HCO^+ versus $^{28}SiH^+$.

Analysis	R_0(ppt)	μ(D)	T(K)
Polynomial	71(22)	3.898(22)	5.90(39)
Piece-wise	70(25)	3.917(24)	5.80(44)

The fit was made to the histogram data which had the predicted ratio, including systematic shifts, subtracted. R_0 is therefore the shift between the predicted ratio and the measured ratio. The predicted ratio had an uncertainty of 156 ppt. Hence, the expected value of R_0 is 0(156) ppt, and the observed R_0 in Table 5.5 are in good agreement.

From the amplitudes obtained from fitting the histogram, the temperature in the trap was estimated to be approximately 5.85(42) K, mysteriously higher than the expected 4.2 K temperature of the liquid helium surrounding the vacuum can containing it.

Another way to obtain an effective rotational temperature is to measure the population ratio of state *J=0* to all higher states.

$$Population \quad Ratio = \frac{P(J \geq 1)}{P(J=0)} = \sum_{J=1}^{\infty} (2J+1) e^{\frac{-B_0 J(J+1)}{k_B T}} \qquad [5.14]$$

Table 5.6 Population of all states J ≥ 1 relative to J = 0. The first two entries in the table correspond to Equation 5.14 assuming temperatures 4.2 K and 5.85 K. The third entry is the relative integrated area of all peaks J ≥ 1 relative to J = 0 with one standard deviation error calculated using a binomial distribution.

Method	Population Ratio	Corresponding Temperature (K)
Boltzmann Factor (4.2K)	1.334	4.2
Boltzmann Factor (5.85K)	2.093	5.85
Integrating Histogram	1.94(17)	5.5(1.1)

Averaging the two dipole moments from the piece-wise and polynomial interpolation methods, we extracted a dipole moment of $\mu = 3.907(26)$ D. The error is derived from the histogram fit error (See Table 5.5) combined in quadrature with half the difference in the results of different methods of interpolating the $^{28}SiH^+$ cyclotron frequency measurements.

5.6 NH^+ Data Collection and Analysis

Unlike HCO^+, where the jump rate is fast enough to complete the experiment with a single ion, for NH^+, because of the much slower jump rate, it is necessary to make and remake the ion to sample the different states (See Section 5.4.2). Hence we used 17 NH^+ ions. In fact, the HCO^+ and NH^+ measurements were separated by a year, during which time the vacuum in the trap had degraded (the masses of ^{76,74}Ge/Se, ^{115}Sn/In, ^{23}Na, and ^{6}Li were measured in the mean-time), causing a shorter lifetime for the NH^+ ions, so we never had to actually kill any NH^+ ion.

The measurement of the mass of ^{7}Li had been attempted in the weeks before the measurement of NH^+. According to the chemistry literature [168], Li can react with nitrogen to form Li_3N, which can then react with water molecules to form ammonia. From ammonia, NH^+ could then be made. This was tested by looking for NH^+ after passing current through the Li

element and running the FEP. NH^+ was observed using this method, however it was not observed after several attempts at making it from background gas. Therefore, it is apparent that some mechanism involving heating the Li element was producing NH_3, or possibly NH. $^{15}N^+$ was chosen as the reference ion because it is a mass-doublet with NH^+ and the mass of ^{15}N is known to 0.05 ppb [90].

For each NH^+ ion made, we obtained one run of cyclotron frequency ratio measurements of $NH^+/^{15}N^+$. Since one of these ions showed a jump, we were able to extract 18 separate measurements of the ratio over a two month period. For each run, the statistical and systematic errors were calculated and combined in quadrature to form the final error. Since $NH^+/^{15}N^+$ is a mass doublet, the systematic shifts were small for each measurement, and the statistical uncertainty dominates each measurement's error. Scatter in the cyclotron frequency data similar to the scatter observed in the ^6Li data (taken two months before the NH^+ data, see Section 1.3.3) was responsible for an increased statistical error. Initially, it was suspected that this increase was due to noise in the smaller voltages needed for the lighter ions. However, now it is believed to be due to magnetic field instability. Figure 5.9 is a plot of the average cyclotron frequency ratios for each different NH^+ ion (with two ratios for the NH^+ which was observed to jump).

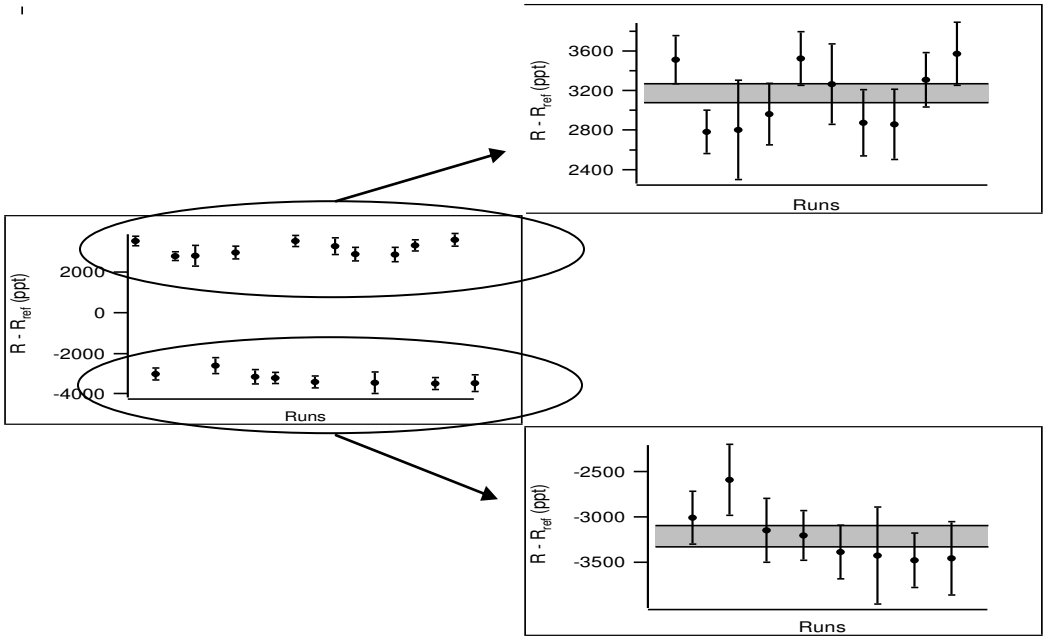

Figure 5.9 All ratio measurements for $NH^+/^{15}N^+$ with an enlargement showing the two opposite parity states. The bands indicate the weighted average and error.

From these plots, the weighted average cyclotron frequency ratio with the ion in the two opposite parity states was obtained. The difference in the averages of the measured ratios in the upper and lower states was found to be $\Delta_{meas} = 6386(151)$ ppt. The calculated difference in polarizability shifts from [135] is $\Delta_{calc} = 6512(227)$ ppt. Here, the uncertainty is due to an inability to resolve the M_J states for each $J=1/2^{\pm}$ state (see Figure 5.2), which have somewhat different polarizabilities. The calculation of this uncertainty is similar to that of [66]. The measured dipole moment may be obtained by scaling the calculated dipole moment, μ_{calc} = 0.790(8) ea_0 [135], by the square root of $\Delta_{meas} / \Delta_{calc}$. The dipole moment that was obtained is hence μ_{meas} = 0.782(18) ea_0.

4.7 Conclusion

While there have been many theoretical calculations of the dipole moments of HCO^+ and NH^+, this section has described the first *experimental* determination of these values (it is difficult to measure the Stark Effect for ions since they are swept away by the electric field). In both cases, the experimental measurements confirm the theoretical calculations. Note that since we measure the polarizability (which is proportional to μ^2), the FSU values in the tables are actually $|\mu|$, that is we are unable to determine the sign.

Table 5.7 The FSU HCO^+ dipole measurement compared to calculated dipole moments.

Determination	Method	HCO^+ μ(D)
Yamaguchi 1994 [150]	Theory	3.888(4)
FSU-PPT 2010 [169]	Experiment	3.907(26)

Table 5.8 The FSU NH^+ dipole measurement compared to calculated dipole moment.

Determination	Method	NH^+ μ(ea_0)
Cheng 2007 [135]	Theory	0.790(8)
FSU-PPT 2010 [169]	Experiment	0.782(18)

HCO^+ and NH^+ join PH^+ [69] and CO^+ [63] as the only precision Penning Trap dipole moment measurements and number among the highest precision experimental dipole moments of molecular ions. Other less accurate experimental determinations of molecular ion dipole moments are obtained through measurements of the isotopic dependence of the rotational Zeeman effect by far-IR laser spectroscopy [170].

Future possible dipole moments measurements may include N_2H^+, which is another molecular ion important to astrophysics (similar applications as HCO^+) [171,172]. Another interesting measurement would be to revisit NH^+ using molecular spectroscopy techniques. Transitions could be induced with a microwave generator, however admitting microwaves into the Penning Trap would be a development project.

6. SUMMARY AND FUTURE WORK

6.1 Summary

This dissertation has described many mass measurements accomplished by the FSU-PPT in the past four years for a variety of applications. Table 6.1 is the summary of these values, along with their purposes.

Table 6.1 Summary of Mass Measurements in this Dissertation.

Atom	Mass (u)	σm/m (ppb)	Reference	Why?
^{17}O	16.999 131 756 6(9)	0.05	[173]	Molecular Spectroscopy
^{18}O	17.999 159 613 0(13)	0.07	[23]	Molecular Spectroscopy
^{19}F	18.998 403 162 9(11)	0.06		Mass Reference
^{130}Xe	129.903 509 351(15)	0.12	[87]	Neutrinoless Double Beta Decay
^{130}Te	129.906 222 744(16)	0.12		
^{6}Li	6.015 122 887 4(31)	0.52	[174]	Photon Recoil, Mass Reference
^{23}Na	22.989 769 282 8(26)	0.11		
^{39}K	38.963 706 485 6(52)	0.13		
^{41}K	40.961 825 257 4(48)	0.12		
^{85}Rb	84.911 789 738(9)	0.11		
^{87}Rb	86.909 180 535(10)	0.12		
^{133}Cs	132.905 451 960(13)	0.10		
^{74}Se	73.922 475 938(15)	0.20	[88]	Neutrinoless Double Electron Capture
^{74}Ge	73.921 177 765(15)	0.20		
^{76}Se	75.919 213 707(19)	0.25		Neutrinoless Double Beta Decay
^{76}Ge	75.921 402 729(19)	0.25		
^{115}Sn	114.903 344 697(17)	0.15	[119]	Lowest Q-Value Beta Decay
^{115}In	114.903 878 774(16)	0.14		

In addition to these masses, two electric dipole moments were also measured:

$$\mu(HCO^+) = 3.907(26)\ D$$

$$\mu(NH^+) = 0.782(18)\ D.$$

Several improvements and advancements to the FSU-PPT have enabled these measurements. A vapor loader now allows vapors to be introduced into the trap, greatly increasing the range of species that can be measured. The two-ion swapping technique, first developed and described in [66], has been further developed to allow the ion in the large cyclotron orbit to be constantly monitored and therefore cooled more efficiently. This technique

has also been extended to include the first two-ion swapping measurements of non-mass doublets in the FSU-PPT, as well as multiply charged ions.

6.2 Future Work with Current Detection Circuit

The following measurements could be done with the current detection circuit, which has a resonant frequency of 213 kHz, and an *m/q*-bandwidth of 12 - 45 u.

6.2.1 ^{174}Yb Mass Measurement for the Fine Structure Constant

Photon recoil measurements, using Yb isotopes (initially ^{174}Yb which is the most abundant) for the determination of the fine structure constant (similar to those for the alkalis) are in progress at the University of Washington using a novel BEC atom interferometer [175,176]. Several Yb isotopes can be cooled to quantum degeneracy. The current precision of the mass of ^{174}Yb is known to 15 ppb. Measurements of the mass of ^{174}Yb with the FSU-PPT have been attempted, but were delayed due to magnetic field instability and short ion lifetime, presumably due to a deterioration of the vacuum. The trap has now been warmed to room temperature to outgas it and the magnet has been re-shimmed. Measurements should resume in the near future.

6.2.2 NH^+ Molecular Spectroscopy

Another interesting measurement would be to revisit NH^+ using molecular spectroscopy techniques. Transitions between the two Λ-doubling states could be induced with a microwave generator. These transitions could then be detected. In fact, since the difference in the cyclotron frequency due to the two polarizabilities of the states is so large (see Chapter 5), the evolution times required to differentiate the states is only about 5 sec (compared to the normal 58 sec cycles). However admitting microwaves into the Penning Trap would be a development project.

6.2.3 Direct Test *of* $E = mc^2$ with ^{35,36}Cl

Einstein's famous equation, $E = mc^2$, is perhaps the best-known equation in all of physics. Thermal neutron capture experiments combined with precision mass measurements provide a direct test of this relation. Tests of this nature have already been performed using ^{33}S and ^{29}Si [177]. An additional test using ^{36}Cl is being considered. The gamma rays emitted after the reaction:

$$n + {}^{35}Cl \rightarrow {}^{36}Cl + \gamma' s$$

have been measured [178], but the atom's masses are not yet precisely known. The mass of ^{35}Cl is known to 1.1 ppb, and the mass of ^{36}Cl is known to 2.1 ppb [90]. To compare with the gamma energy precision, the mass difference must be improved by about two orders of magnitude. The measurement consists of measuring the cyclotron frequency ratio of $H^{35}Cl^+$ and $^{36}Cl^+$ and is complicated by the radioactivity of $^{36}Cl^+$ and polarizability shifts in $H^{35}Cl^+$.

6.2.4 Mass of ^{136}Ba for Neutrinoless Double β-decay

While the mass of ^{136}Xe was measured by the FSU-PPT for the neutrinoless double β-decay [68], the mass of ^{136}Ba was not. If the mass of ^{136}Ba was measured to the same precision as the mass of ^{136}Xe, the uncertainty in the *Q*-value would be reduced by about a factor of 40.

6.3 Future Work with New Higher Frequency Detection Circuit

Measurements with lighter ions require a detection circuit with significantly higher axial frequency, in the region of 600 kHz, in order to produce a sufficiently large axial signal for the PNP method to work. A new superconducting coil has been wound and is ready to be installed.

6.3.1 The Mass of the ^{6,7}Li Monomers

A good test of the Penning trap with the new detector would be to first measure the mass of the ^{6}Li monomer, since the dimer has already been measured by the FSU-PPT (see Section 4.1). Additionally, a measurement of the mass of ^{7}Li would complete the FSU-PPT stable alkali mass measurements (the mass of the dimer was made almost impossible by the presence of ^{14}N in the trap).

6.3.2 ^{3}He/^{3}H Q-value for Neutrino Mass Measurements

This measurement has been described in almost every MIT/FSU Penning trap dissertation on the future "to-do" list, however this mass difference is as important now as it ever was. It has not been attempted yet for three main reasons: it requires that the coil be changed, tritium is radioactive, and ^{3}He and hydrogen isotopes can spoil the cryogenic vacuum.

The tritium β-decay

$$^3H \rightarrow {}^3He^+ + e^- + \overline{\upsilon}_e$$

will be studied by the KATRIN experiment, which should be running within the next decade. This new experiment will improve upon previous Kurie-plot experiments and ultimately provide a limit on the electron neutrino mass at the level of 0.2 eV/c^2 [179]. KATRIN measures the shape of the energy spectrum near the end-point of the β-decay spectrum and also determines the *Q*-value for the decay. The *Q*-value that can be obtained from the ^3He-^3H mass difference will check this value and hence provide an independent check of the systematics for KATRIN.

LIST OF REFERENCES

[1] J. Dalton, Mem. Proc. Machr. Lit. Phil. Soc. **1**, 271 (1805).

[2] N.E. Holden, Chem. Int. **26**, 1 (2004).

[3] B.W. Petley, IEEE Trans. Instr. Meas. **38**, 175 (1989).

[4] T.B. Coplen, H.S. Peiser, *History of the Recommended Atomic Weight Value from 1882 to 1997*, IUPAC Technical Report (1997).

[5] F.W. Clarke, Am. Chem. Soc. **25**, 1 (1903).

[6] D. Mendelejeff, *Zeitschrift für Chemie* **12**, 405-6 (1869).

[7] "Frederick Soddy - Nobel Lecture". Nobelprize.org. 1 Oct 2010 http://nobelprize.org/nobel_prizes/chemistry/laureates/1921/soddy-lecture.html.

[8] J.J. Thomson, *Rays of Positive Electricity and their Application to Chemical Analysis*, (Longmans, 1913).

[9] F.W. Aston, Phil. Mag. XXXXVIII(), 707 (1919); F.W. Aston, Phys. Rev. XI(), 36 (1918).

[10] "Francis W. Aston - Biography". Nobelprize.org. 2 Oct 2010 http://nobelprize.org/nobel_prizes/chemistry/laureates/1922/aston.html.

[11] G. Squires, J. Chem. Soc., Dalton Trans. 3893 (1998).

[12] M.S. Livingston, Phys. Today **12**, 18 (1959).

[13] E.O. Lawrence, M.S. Livingston, Phys. Rev. **40**, 19 (1932).

[14] H. Sommer, H.A. Thomas, J.A. Hipple, Phys. Rev. **82**, 697 (1951).

[15] H.G. Dehmelt, F.L. Walls, Phys. Rev. Lett. **21**, 127 (1968).

[16] D. Wineland, P. Ekstrom, H.G. Dehmelt, Phys. Rev. Lett. **31**, 1279 (1973).

[17] R.S. Van Dyck, D.B. Pinegar, S. Van Liew, S.L. Zafonte, Int. J. Mass. Spec. **251**, 231 (2006).

[18] M.B. Comisarow, A.G. Marshall, J. Mass. Spec. **31**, 581 (1996).

[19] A.G. Marshall, Int. J. Mass. Spec. **200**, 331 (2000).

[20] A.G. Marshall, C.L. Hendrickson, G.S. Jackson, Mass Spec. Rev. **17**, 1 (1998).

[21] T.M. Schaub, C.L Hendrickson, S. Horning, J.P. Quinn, M.W. Senko, A.G. Marshall, Anal. Chem. **80**, 3985 (2008).

[22] W.F. Giague, H.L. Johnson, *Nature*, **123**, 318 (1929); W.F. Giague, H.L. Johnson, *Nature* **123**, 831 (1929).

[23] M. Redshaw, B.J. Mount, E.G. Myers, Phys. Rev. A **79**, 012507 (2009).

[24] G. Gabrielse, Int. J. Mass. Spec., **279**, 107 (2009).

[25] K. Blaum, Y.N. Novikov, G. Werth, Contemp. Phys. **51**, 149 (2010).

[26] K. Blaum, S. Nagy, G. Werth, J. Phys. B **42**, 154015 (2009).

[27] R.S. Van Dyck, P.B. Schwinberg, H.G. Dehmelt., Phys. Rev. Lett. **59**, 26 (1987).

[28] D. Hanneke, S. Fogwell, G. Gabrielse, Phys. Rev. Lett. **100**, 15501 (2008).

[29] G. Gabrielse, A. Khabbaz, D.S. Hall, C. Heimann, H. Kalinowsky, W. Jhe, Phys. Rev. Lett. **82**, 3198 (1999)

[30] J. Verdu, S. Djekic, S. Stahl, T. Valenzuela, M. Vogel, G. Werth, Phys. Rev. Lett. **92**, 093002 (2004).

[31] R.W. Flanagan, "Trapping and Detection of Ions", Ph.D. Thesis, MIT (1987).

[32] R.M. Weisskoff, "Detecting Single, Trapped Ions", Ph.D. Thesis, MIT (1983).

[33] E.A. Cornell, "Mass Spectroscopy Using Single Ion Cyclotron Resonance", Ph.D. Thesis, MIT (1990).

[34] K.R. Boyce, "Improved Single-Ion Cyclotron Resonance Mass Spectroscopy", Ph.D. Thesis, MIT (1992).

[35] V. Natarajan, "Precision Mass Spectroscopy at 0.1 ppb", Ph.D. Thesis, MIT (1993)

[36] F. DiFilippo, "Precise Atomic Masses for Determining Fundamental Constants", Ph.D. Thesis, MIT (1994).

[37] M.P. Bradley, "A Sub-ppb Measurement of the Mass of Cesium for a New Determination of the Fine-Structure Constant", Ph.D. Thesis, MIT (2000)

[38] S. Rainville, "A Two-Ion Balance for High Precision Mass Spectrometry", Ph.D. Thesis, MIT (2003).

[39] J.K. Thompson, "Two-Ion Control and Polarization Forces for Precise Mass Comparisons", Ph.D. Thesis, MIT (2003).

[40] M. Smith, *et al.,* Phys. Rev. Lett. **101**, 202501 (2008).

[41] S. Naimi *et al.,* Phys. Rev. Lett. **105**, 032502 (2010).

[42] M. Breitenfeldt *et al*., Phys. Rev. C **81**, 034313 (2010).

[43] M. Kowalska, Hyperfine Interact. **196**, 199 (2009).

[44] A. Kankainen, *et al.,* Phys. Rev. C **82**, 034311 (2010).

[45] V.S. Kolhinen, *et al.,* Phys. Rev. C **82**, 022501(R) (2010).

[46] V.S. Kolhinen, *et al.,* Phys. Lett. B **684**, 17 (2010).

[47] A.T. Gallant, *et al.,* J. Instr. **5**, C08009 (2010).

[48] S. Ettenauer, *et al.,* Phys. Rev. C **81**, 024314 (2010).

[49] M. Brodeur, *et al.,* Phys. Rev. C **80**, 044318 (2009).

[50] R. Ringle, *et al.,* Phys. Lett. B **675**, 170 (2009).

[51] A. Solders, I. Bergstrom, S. Nagy, M. Suhonen, R. Schuch, Phys. Rev. A **78**, 012514 (2008).

[52] S. Nagy, *et al.,* Phys. Rev. Lett. **96**, 163004 (2006).

[53] S. Nagy, T. Fritioff, M. Bjorkhage, I. Bergstrom, R. Shuch, Europhys. Lett. **74**, 404 (2006).

[54] R. Ringle, *et al.,* Phys. Rev. C **80**, 064321 (2009).

[55] R. Ferrer, *et al.,* Phys. Rev. C **81**, 044318 (2010).

[56] A.A. Kwiatkowski, *et al.,* Phys. Rev. C **81**, 058501 (2010).

[57] N.D. Scielzo, *et al.,* Phys. Rev. C **80**, 025501 (2009).

[58] M. Block, *et al.,* Nature **463**, 785 (2010).

[59] M. Dworschak, *et al.,* Phys. Rev. C **81**, 064312 (2010).

[60] S. Rainville, J.K. Thompson, D.E. Pritchard, Science **303,** 334 (2003).

[61] E.A. Cornell, R.M. Weisskoff, K.R. Boyce, D.E. Pritchard, Phys. Rev. A **41**, 312 (1990)

[62] E.A. Cornell, R.M. Weisskoff, K.R. Boyace, R.W. Flanagan, Jr., G.P. Lafyatis, D.E. Pritchard, Phys. Rev. Lett. **63,** 1674 (1989)

[63] J.K. Thompson, S. Rainville, D.E. Pritchard, Nature **430**, 58 (2004)

[64] F. DiFilippo, v. Nataragan, K.R. Boyce, D.E. Pritchard, Phys. Rev. Lett. **73**, 1481 (1994).

[65] M.P. Bradley, J.V. Porto, S. Rainville, J.K. Thompson, D.E. Pritchard, Phys. Rev. Lett. **83** 4510 (1990)

[66] M. Redshaw, "Precise Measurements of the Atomic Masses of ^{28}Si, ^{31}P, ^{32}S, ^{84,86}Kr, ^{129,132,136}Xe, and the Dipole Moment of PH^+ Using Single-ion and Two-ion Penning Trap Techniques", Ph.D. Thesis, FSU (2007).

[67] W. Shi, M. Redshaw, E.G. Myers, Phys. Rev. A **72**, 022510 (2005)

[68] M. Redshaw, E. Wingfield, J. McDaniel and E.G. Myers, Phys. Lett. **98**, 053003 (2007).

[69] M. Redshaw, J. McDaniel, and E.G. Myers, Phys. Rev. Lett. **100**, 093002 (2008).

[70] M. Redshaw, B.J. Mount, E.G. Myers, Phys. Rev. A **79**, 012506 (2009)

[71] L.S. Brown and G. Gabrielse, Rev. Mod. Phys. **58**, 233 (1986).

[72] L.D. Landau and E.M. Lifshitz, *The Classical Theory of Fields*, (Elsevier Ltd., 1975), 4th Revised English Edition.

[73] http://www.saesgetters.com/default.aspx?idPage=470.

[74] R. Nguyen, Undergraduate Thesis, MIT, 1998.

[75] J.C. Gallop, SQUIDs, the Josephson Effects and Superconducting Electronics (Adam Hilger, Bristol, 1991).

[76] E.A. Cornell, R.M. Weisskoff, K.R. Boyce, D.E. Pritchard, Phys. Rev. A **41**, 312 (1990).

[77] P.R. Bevington and D.K. Robinson, *Data Reduction and Error Analysis for the Physical Sciences* (McGraw-Hill, New York, 2003), 3rd Edition

[78] J.D. Jackson, *Classical Electrodynamics*, (Wiley, 1999), 3rd Edition

[79] M. Redshaw, J. McDaniel, W. Shi, and E.G. Myers, Int. J. Mass Spec. **251**, 125 (2006).

[80] S.R. Elliot, A.A. Hahn, M.K. Moe, Phys. Rev. Lett. **59**, 2020 (1987).

[81] S.R. Elliot and J. Engel, J. Phys. G 30 R183 (2004).

[82] Y. Ashie *et al,* Phys. Rev. Lett. **93,** 10801 (2004).

[83] B. Aharmin *et al*, Phys. Rev. Lett. **101,** 111301 (2008).

[84] P. Vogel, arXive:hep-ph/0611243v1 (2006).

[85] F.T. Avignone III, S.R. Elliot, J. Engel, Rev. Mod. Phys. **80** 481 (2008).

[86] C. Amsler *et al.* (Particle Data Group), PL **B667**, 1 (2008) (URL: http://pdg.lbl.gov).

[87] M. Redshaw, B.J. Mount, E.G. Myers, Phys. Rev. Lett. **102**, 212502 (2009).

[88] B.J. Mount, M. Redshaw, E.G. Myers, Phys. Rev. C **81**, 032501(R) (2010).

[89] S. Rahaman, *et al.*, Phys. Lett. B **662,** 111 (2008).

[90] G. Audi, A.H. Wapstra, C. Thibault, Nucl. Phys. A **729**, 337 (2003).

[91] P.J. Mohr, B.N. Taylor, D.B. Newell, Rev. Mod. Phys. **80**, 633 (2008).

[92] C.E. Alaseth, *et al.,* Phys. Rev. D, **65**, 092007 (2002).

[93] L. Baudis *et al.,* Phys. Rev. Lett. **83**, 41 (1999).

[94] H.V. Klapdor-Kleingrothaus, A. Dietz, I.V. Krivosheina, and O. Chkvorets, Phys.Lett. B **586** 198 (2004); H.V. Klapdor-Kleingrothaus and I.V. Krivosheina, Mod. Phys. Lett. A, **21**, 1547 (2006).

[95] C.E. Aalseth, *et al.*, Mod. Phys. Lett. A **17**, 1475 (2002).

[96] C. Arnaboldi, *et al.*, Phys. Rev. C **78**, 035502 (2008).

[97] F. Avignone, private communication, (2008).

[98] R. Ardito *et al*. (CUORE Collaboration), arXiv:hep-ex/0501010.

[99] R.G. Winter, Phys. Rev. **100**, 142 (1955).

[100] D. Frekers, arXiv:hep-exp/0506002v2.

[101] A.S. Barabash, P. Hubert, A. Nachab, V. Umatov, Nucl. Phys. A **785**, 371 (2007).

[102] J. Bernabeu, A. De Rujula and C. Jarlskog, Nucl. Phys. B **223**, 15 (1983).

[103] Z. Sujkowski and S. Wycech, Phys. Rev. C **70**, 052501(R) (2004).

[104] S. Rahaman, *et al.,* Phys. Rev. Lett. **103**, 042501 (2009).

[105] B. Singh and A.R. Farhan, Nucl. Data Sheets **107**, 1923 (2006).

[106] F.B. Larkins, At. Data and Nucl. Data Tables **20,** 313 (1977).

[107] K.D. Sevier, *Low Energy Electron Spectrometry*, (Wiley-Interscience, New York), 1972

[108] E.B. Saloman, J. Phys. Chem. Ref. Data **36**, 215 (2007).

[109] J. Sugar, A. Musgrove, J. Phys. Chem. Ref. Data **22**, 1213 (1993).

[110] N.D. Scielzo *et al.,* Phys. Rev. C **80**, 025501 (2009).

[111] G. Douysset, T. Fritioff, C. Carlberg, Phys. Rev. Lett. **86**, 4259 (2001).

[112] P.M. McCowan and R.C Barber, Phys. Rev. C, **82**, 024603 (2010)

[113] A. Herlert, *et al.,* Int. J. Mass. Spec. **251**, 131 (2006).

[114] C.M. Cattadori, M. De Deo, M. Laubenstein, L. Pandola, V.I. Tretyak, Nucl. Phys. A **748**, 333 (2005); C.M. Cattadori, M. De Deo, M. Laubenstein, L. Pandola, V.I. Tretyak, Phys. Atom. Nucl. **70,** 127 (2005).

[115] J. Blachot, Nuclear Data Sheets **104**, 967 (2005).

[116] L. Pfeiffer, A.P. Mills, E.A. Chandross, T. Kovacs, Phys. Rev. C **19**, 1035 (1978).

[117] M. Galeazzi, F. Fontanelli, F. Gatti, S. Vitale, Phys. Rev. C **63,** 014302 (2000).

[118] J.S.E Wieslander *et al.,* Phys. Rev. Lett. **103** 122501 (2009).

[119] B.J. Mount, M. Redshaw, E.G. Myers, Phys. Rev. Lett. **103**, 122502 (2009).

[120] M.T. Mustonen, J. Suhonen, J. Phys. G **37**, 064008 (2010).

[121] T. Aoyama, M. Hayakawa, T. Kinoshita, and M. Nio, Phys. Rev. Lett. **99**, 110406 (2007).

[122] A. Czarnecki and B. Krause, Phys. Rev. Lett. **76**, 3267 (1996).

[123] Th. Udem, A. Huber, B. Gross, J. Reichert, M. Prevedelli, M. Weitz, T.W. Haensch, Phys. Rev. Lett. **79**, 2646 (1997); C. Schwob, L. Jozefowski, B. de Beauvoir, L. Hilico, F. Nez, L. Julien, F. Biraben, Phys. Rev. Lett. **82,** 4960 (1999)

[124] G. Werth, J. Alonso, T. Beier, S. Djekic, H. Haffner, N. Hermansphahn, W. Quint, S. Stahl, J. Verdu, T. Valenzuela, M. Volgel, Int.J. Mass Spectrom. **251**, 152 (2006); D.L. Farnham, R.S. Can Dyck, P.B. Schwinbergg, Phys. Rev. Lett. **75**, 3598 (1995).

[125] M. Cadoret, E. de Mirandes, P. Cladè, S. Guellati-Khèlifa, C. Schwob, F. Nez, L. Julien, F. Biraben Phys. Rev. Lett. **101**, 230801 (2008).

[126] V. Gerginov, K. Calkins, C.E. Tanner, Phys. Rev. A **73**, 032504 (2006); A. Wicht, J.M. Hensley, E. Sarajlic, S. Chu, Physica Scripta, **T102**, 82 (2002).

[127] K. Pachucki, V.A. Yerokhin, Phys. Rev. Lett. **104**, 070403 (2010).

[128] H. Müller, S. Chiow, Q. Long, S. Herrmann, S. Chu, Phys. Rev. Lett. **100** 180405 (2008).

[129] CRC, Handbook of Chemistry and Physics, 90th Ed., 2009/10, editor D.R. Lide.

[130] T.P. Heavner, S.R. Jefferts, Phys. Rev. A **64**, 062504 (2001)

[131] Z.-C. Yan, W. Norterhauser, G.W.F. Drake, Phys. Rev. Lett. **100**, 243002 (2008)

[132] P.J.J. Kok, K. Abrahams, H. Postma, W.J. Huiskamp, Nucl. Instrum. Meth. B, **12**, 325 (1985)

[133] Firestone, R.B., Choi, H.D., Lindstrom, R.M., Molnar, G.L., Mughabghab, S.F., Paviotti-Corcuera, R., et al.(2004). Database of prompt gamma rays from slow neutron capture for elemental analysis. Lawrence Berkeley National Laboratory: Lawrence Berkeley National Laboratory. LBNL Paper LBNL-55199. Retrieved from: http://www.escholarship.org/uc/item/1wj43711

[134] http://www.saesgetters.com/.

[135] M. Cheng, J.M. Brown, P. Rosmus, R. Linguerri, N. Komiha, E.G. Myers, Phys. Rev. A **75**, 012502 (2007).

[136] J.E. Sansonetti, W.C. Martin, eds., NIST Hanbook of Basic Atomic Spectroscopic Data, http://physics.nist.gov/PhysRefData/Handbook/index.html.

[137] http://www.astro.lsa.umich.edu/~cowley/ionen.htm.

[138] E.B. Saloman, J. Phys. Chem. Ref. Data, 36, 215 (2007).

[139] E. B. Saloman, J. Phys. Chem. Ref. Data **33**, 765 (2004).

[140] I. Johansson, Ark. Fys. 20, 135 (1961).

[141] P. J. Linstrom and W. G. Mallard, eds., NIST Chemistry WebBook, http://webbook.nist.gov.

[142] J. Reader, J. Opt. Soc. Am. 65, 286 (1975).

[143] M. Mukherjee et al., Eur. Phys. J. A. **35** 31-37 (2008).

[144] H.S.P. Müller, M.C. McCarthy, L. Bizzochi, H. Gupta, S. Esser, H. Lichau, M. Caris, F. Lewen, J. Hahn, C. Degli Esposti, S. Schlemmer, and P. Thaddeus, Phys. Chem. Chem. Phys., **9**, 1579 (2007)

[145] J.L. Dunham, Phys. Rev. **41**, 721 (1932).

[146] J.K.G. Watson, J. Mol. Spectrosc., **45**, 99 (1973).

[147] H.S.P. Müller, private communication

[148] G. Savard *et al*, Phys. Rev. C, **70** 042501(R) (2004).

[150] Y. Yamaguchi, C.A. Richards, Jr., H.F. Shaefer III, J. Chem. Phys. **101**, 8945 (1994).

[151] D. Buhl, L.E. Snyder, Nature, **228**, 267 (1970).

[152] E.A. Bergin, M. Tafalla, Annu. Rev. Astron. Astrophys., **45**, 339 (2007).

[153] L. Zhu, J. Yang, M. Wang, Chinese Astron. Astr. **31**, 387 (2007).

[154] M. Krips et al, Astrophys. J., **677**, 262 (2008).

[155] S. Nikolic, Serb. Astron. J., **175**, 1 (2007).

[156] P.P. Papadopoulos, Astrophys. J., **656**, 792 (2006).

[157] N. Douguet, V. Kokoouline, Phys. Rev. A, **80**, 062712 (2009).

[158] H.W. Hubers, K.M. Evenson, C. Hill, J.M. Brown, J. Chem. Phys. **131**, 034311 (2009).

[159] J. Lecointre, J.J. Jureta, P. Defrance, J. Phys. B **43**, 105202 (2010).

[160] J.M. Amero, G.J. Vazquez, Int. J. Quant. Chem., **101**, 396 (2005).

[161] B.H. Bransden, C.J. Joachain, *Physics of Atoms and Molecules*, Essex: Pearson Education Limited, 2003. Print.

[162] A. L Schawlow, C. H. Townes. *Microwave Spectroscopy*. International series in pure and applied physics. New York: McGraw-Hill, 1955. Print.

[163] G. Herzberg, *Molecular Spectra and Molecular Structure*. New York: Krieger, 1955. Print.

[164] F. Tinti, et al., Astrophys. J. **669**, L113 (2007)

[165] R.W. Field, H. Lefebvre-Brion. *The Spectra and Dynamics of Diatomic Molecules*. Amsterdam: Elsevier Academic Press, 2004. Print

[166] J.M. Brown, A. Carrington. *Rotational Spectroscopy of Diatomic Molecules*. Cambridge molecular science series. Cambridge: Cambridge University Press, 2003. Print.

[167] Dupont Delrin Homepage: http://www2.dupont.com/Plastics/en_US/Products/Delrin/Delrin.html

[168] Greenwood, Norman N., Earnshaw, A., *Chemistry of the Elements* (2nd ed.), Oxford: Butterworth-Heinemann, 1997. Print.

[169] B.J. Mount, M. Redshaw, E.G. Myers, in preparation

[170] K.B. Laughlin et. Al., Phys. Rev. Lett., **58**, 996 (1987)

[171] F. Daniel, J. Cernicharo, M.L. Dubernet, Astrphys. J. **648**, 461 (2006)

[172] M. Havenith, et al., J. Chem. Phys. **93**, 8446 (1990)

[173] B.J. Mount, H.S.P. Mueller, M. Redshaw, E.G. Myers, Phys. Rev. A, **81**, 064501 (2010).

[174] B.J. Mount, M. Redshaw, E.G. Myers, Phys. Rev. A **82**, 042513 (2010).

[175] S. Gupta, private communication

[176] S. Gupta, K. Dieckmann, Z. Hadzibabic, D.E. Pritchard, Phys. Rev. Lett., **89**, 140401 (2002).

[177] S. Rainville *et al.,* Nature, **438**, 1096 (2005).

[178] M. Jentschel et al., AIP Conf. Proc., **769**, 617 (2005).

[179] C. Weinheimer, arXiv:0912.1619v1 [hep-ex] 8 Dec 2009.

BIOGRAPHICAL SKETCH

Brianna J. Mount

Brianna J. Mount (née Tweedy) was born in Lewiston, Idaho on March 12, 1984. She graduated from Lewiston High School in 2002, and from the University of Idaho in 2006 with a Bachelors of Science Degree in Physics and Mathematics. During the summer of her sophomore and junior years at the University of Idaho, Brianna participated in the Pacific Northwest National Laboratory (PNNL) National Security Internship Program working with a Cavity Ring-down Spectroscopy detection system.

Brianna began her graduate studies under the direction of Edmund Myers at Florida State University in 2006. Her work focused on high precision mass measurements using a Penning trap mass spectrometer. Papers co-authored during this time period include:

Atomic masses of ^{6}Li, ^{23}Na, $^{39,41}K$, $^{85,87}Rb$ and ^{133}Cs: B.J. Mount, M. Redshaw, E.G. Myers, Phys. Rev. A **82**, 042513(2010)

Mass of ^{17}O from Penning-trap mass spectrometry and molecular spectroscopy: A precision test of the Dunham-Watson model in carbon monoxide: B.J. Mount, H.S.P. Mueller, M. Redshaw, E.G. Myers, Phys. Rev. A, **81**, 064501 (2010).

Double-β-decay Q values of ^{74}Se and ^{76}Ge: B.J. Mount, M. Redshaw, E.G. Myers, Phys. Rev. C **81**, 032501(R) (2010).

Q Value of $^{115}In \rightarrow ^{115}Sn(3/2^{+})$: The Lowest Known Energy β Decay: B.J. Mount, M. Redshaw, E.G. Myers, Phys. Rev. Lett. **103**, 122502 (2009).

Masses of ^{130}Te and ^{130}Xe and Double-β-Decay Q Value of ^{130}Te: M. Redshaw, B.J. Mount, E.G. Myers, Phys. Rev. Lett. **102**, 212502 (2009).

Improved atomic masses of $^{84,86}Kr$ and $^{129,132}Xe$: M. Redshaw, B.J. Mount, E.G. Myers, Phys. Rev. A **79**, 012506 (2009)

Penning-trap measurement of the atomic masses of ^{18}O and ^{19}F with uncertainties <0.1 parts per 10^{9}: M. Redshaw, B.J. Mount, E.G. Myers, Phys. Rev. A **79**, 012507 (2009).

Brianna obtained her Ph.D. in Physics from Florida State University in 2010.